A STUDY OF THE STAEBLER-WRONSKI EFFECT AND AMORPHOUS SILICON SOLAR CELLS

By

Kim SOLESVIK OPPEDAL
MSc Candidate
June 2013

Examination Committee:
Prof. dr. M. Zeman
Dr. ir. J.F. Creemer
Dr. R.A.C.M.M. van Swaaij
ir. J. Melskens

Technische Universiteit Delft
Photovoltaic Materials and Devices

Preface

The thesis project presented in this report represents the finalization of my Master of Science degree; undertaken at the Delft University of Technology as a part of the Sustainable Energy Technology program. Moreover, this report also represents an academic year marked by new experiences, and a steep learning curve. Throughout the 9-month duration of this thesis I have had the opportunity to fully immerge myself in scientific research within photovoltaics. I have thoroughly enjoyed the direct application of scientific method and reasoning to a project which I could consider my own. Additionally, I have obtained an insight and feel for the research-end of a field which I find fascinating from a technological point of view, and which I believe holds great potential for future power generation – namely photovoltaics and solar power. The move towards renewable energy production is, in my point of view, symbolic of a society which is gaining awareness of- and interest in- the value of sustainable practice. I feel compelled to advocate the need for sustainability in a world which, to a large extent, is characterized by insufficient aid, care, and resources for its population. Therefore, regardless of the focus of my professional career, I will do my utmost to contribute to increased sustainability and efficiency in today's society. The past year has been a motivating and challenging start on this path.

There are several people that deserve acknowledgement for making this year and this master thesis project an invaluable part of my education. First of all, I would like to thank the entire PVMD-group of the TU Delft for the academic community and enjoyable work environment which you provide. A special thanks is due to the chairman of the research group, Prof. Dr. Miro Zeman, for running this entity of the TU Delft with a consistent focus on professionalism and academic competence.

I would like to thank Martijn Tijssen for providing me with all the samples I needed, and for answering all my questions regarding deposition details and the machinery of the PVMD facilities. Furthermore, I would like to thank Jan Chris Staalenburg for all the help regarding the experimental setups which I have used throughout the thesis project.

I wish to accredit the supervisor of this project, Dr. René van Swaaij. Thank you for all our helpful discussions, and the guidance you have given me. Your meticulous and scientific approach to just about any subject has been both educational and inspiring. Finally, a warm thank you is due to my daily supervisor, Jimmy Melskens, for continuously providing necessary support and feedback in the course of the project. Thanks to your supervision and assistance, I have a new understanding of how to apply scientific method and interpretation.

Abstract

The aim of this master thesis project is to compose a comprehensive analysis of hydrogenated amorphous silicon (a-Si:H) solar cells. A large part of this effort is dedicated to investigating the effect of light soaking on the a-Si:H devices, i.e. the Staebler-Wronski Effect (SWE), because of the decisive influence of the latter on solar cell performance. Despite the fact that the SWE was discovered almost 40 years ago, a comprehensive and complete explanation of the phenomenon still eludes the scientific community. As such, the analysis carried out in this project is a contribution to understanding how the SWE impacts today's solar cell devices. The project entails well-controlled characterization of the initial state, the degraded state, and the annealed state of the a-Si:H solar cells. Moreover, the degradation process itself was monitored. In order to unveil the dependencies of the SWE in solar cell devices, several different degradation conditions are explored. Consequently, this study contains analyses of the effect of intrinsic layer material, intrinsic layer thickness, and degradation temperature, on the kinetics of the SWE in a-Si:H solar cells. Characterization under different conditions is vital to understanding the facets of a physical phenomenon, and, more importantly, how to adapt to it. Understanding how to minimize the SWE through variation of internal and external conditions not only yields valuable information about the effect itself, it proves valuable to the industrial application of the a-Si:H devices.

In this context, five different solar cell series are tested. Three series of R_{20}-type solar cells are tested, and two series of R_0-type solar cells are tested. Each series consists of three different samples of different intrinsic layer thickness – 300 nm, 600 nm, and 900 nm. An analysis of thickness and material dependence is carried out in initial, degraded, and annealed state by use of dark IV measurements, EQE measurements, and illuminated IV measurements. The degradation of the samples are carried out using a custom degradation setup of the PVMD group's laboratory facilities. The degradation setup allows for in-situ measurements of illuminated current-voltage measurements during degradation. The degradation environment is well-defined and well-controlled using continuous feed-back computer control of vital parameters such as temperature and light intensity. While the light intensity and wavelength used during degradation are kept constant at $I = 350\ \mathrm{W/m^2}$ and $\lambda = 630\ \mathrm{nm}$, respectively, for all series, the degradation temperature is altered. Thereby, the interplay between solar cell degradation and thermal annealing is explored. The advantage of the in-situ measurement setup provided by the PVMD group is the inherent control over measurement conditions which it offers. An accurate understanding of SWE kinetics relies on minute changes in nanostructure which are untraceable, i.e. impossible to distinguish from measurement contamination, unless they are measured in-situ. The results show the precision with which degradation kinetics of a-Si:H can be traced, permitting a sound framework for further analysis of SWE.

The study reveals distinct differences in a-Si:H device characteristics in the initial, degraded, and annealed state, due to changes in intrinsic layer thickness and material type. This is analyzed in terms of nanostructure within the R_0-type material and R_{20}-type material, as well as the spatial defect distribution of the a-Si:H solar cells. We show evidence supporting the numerical modeling of a-Si:H mobility bandgap determination, which suggests higher values for amorphous silicon deposited using elevated hydrogen-to-silane feed-in gas ratios. Moreover, the degradation and annealing kinetics of a-Si:H solar cells are shown to vary according to the deposition conditions of the samples and the degradation temperature. The in-situ measurement system provides evidence to the clear differences in external parameter evolution between R_0-type and R_{20}-type solar cells during light soaking. The degradation and annealing evolution is interpreted in terms of where in the device it is probable that defects are created. The notion of soft and hard defects is demonstrated, investigated, and interpreted in light of annealing kinetics of the different samples. We show supporting evidence that defect creation occurs throughout the intrinsic layer of the solar cell during light soaking. Moreover, the numerous EQE measurements of the devices imply that the charge collection in a-Si:H device may be limited by electron – and not hole – propagation in the device. This seems to hold true before and after light-induced degradation of the solar cells. Finally, the kinetics of the solar cells are presented as two distinct regimes – fast degradation and slow degradation. The results presented herein suggest that these regimes are not well described by the current numerical models of a-Si:H degradation.

Table of Contents

Chapter 1: Introduction

1.1 Leap to Renewable Energies

1.1.1 Background

While talk of climate change and the environmental footprint of the human race may seem to be a 21st century phenomena, awareness of human impact on earth's ecosystems are far from recent. Theophrastus, student of Aristotle and ancient Greek philosopher, noted alterations in nearby localities, which he perceived as a direct result of human intervention in the area [1]. Similar suspicions of human impact on the environment, and even the local climate, prevailed and re-appeared, most notably during the Renaissance period. Meanwhile, it was not until the 19th Century that the greenhouse effect, a process by which thermal radiation from a planetary surface is absorbed by atmospheric gases (so-called greenhouse gases, or GHG) and re-radiated in all directions, was defined by scientists [2]. In modern times, and most notably throughout the past 50 years, a long list of international conferences and committees have attempted to mitigate man-made changes in climate and emission of greenhouse gases, the most infamous of which being carbon dioxide.

International awareness has progressed immensely since the first World Climate Conference took place in 1979. The world has seen the creation of the Intergovernmental Panel on Climate Change (IPCC), the Brundtland Report, and the Kyoto Protocol. As of 2012, all major nations, both developed and developing, have agreed to a roadmap to reduce GHG-emissions [3]. Nonetheless, the measures undertaken so far seem feeble when faced against the immense, ongoing process of global warming. Carbon trading and other clean development mechanisms (CDIs) fostered by environmentalists have failed to yield the desired results, as industrial actors consistently find loop-holes in these systems, which are inherently flawed due to lack of global consensus [4]. Meanwhile, the countries of the world struggle to strike equilibrium between national interests and the common good. This is manifested through strong resistance to impose economic incentives to reduce emissions, such as carbon taxes. Indeed, the question of "who takes the bill?" splits the international community. While developing nations do not wish to bear the punishment for a global trend initialized by the now industrialized countries, the developed countries are equally unwilling, and perhaps unable, to offer free ride to other countries. The result of these diplomatic disputes is that the world's largest emitters (U.S.A., Russia and Canada) never ratified, have discontinued, or have renounced the Kyoto Protocol [5]. On the other hand, *the* world's largest GHG-emitter, China, vigorously clung to its status as 'developing nation' during the most recent U.N. climate negotiation's meeting, thus avoiding any binding emission targets. Furthermore, the economic downturn and consequent financial crisis which have marked the western world since 2008 are far from urging nations to be more generous.

1.1.2 Imminent Dangers

The need for action and investment, however, is urgent if long-term, irreversible climate change is to be avoided. As the world passed the seven billion population count, the world energy consumption also reached new heights. To underline the world's entrenchment within fossil-fuel expenditure – only 4.9 percent of the total energy consumption was fuelled by carbon-neutral renewable energy sources. All the while, the IEA reports that an average temperature increase may reach 6 degrees Celsius before the end of the 21st century [6]. Risk analysts and humanitarians paint a dreary picture of a future where coastal cities, and thereby some of the largest economic hubs in the world, as well as populations living in other climate sensitive regions, are likely to be highly inflicted by a rising sea-level. The IEA and the IPCC also estimate that fossil fuels are likely to be depleted within the coming 100 to 200 years, given today's energy consumption trends, extraction methods, and knowledge of fossil fuel reserves [7].

1.1.3 Global Transition to Counteract Climate Change

The transition to renewable energy is considered necessary in order to alleviate the human footprint on climate and environment. In the IPCC Study, "Special Report on Renewable Energy Sources and Climate Change Mitigation", the panel investigates 164 different scenarios of climate evolution towards the year 2050. Although not all of these scenarios predicted significant GHG-emission reductions, those that did showed a massive expansion of renewable energy technology. Additionally, the total energetic potential of renewable energy resources is manifold that of the total energy needs. It is estimated that the technical potential of renewable energy technologies far outweighs the global energy demand for electricity with today's technologies. The IPCC considers that the current technologies and renewable resources would be sufficient to meet the world's energy needs. Nonetheless, the possible outcome reported by the IPCC, concludes that 80 percent of the global energy consumption *could* be covered by renewable energy sources, given that each country commits properly to this effect [8]. Such a commitment would most likely entail economic incentives to favor renewable energies as opposed to fossil fuels. For example, the subsidies to fossil fuel production and consumption, a world-wide total of $600 billion in 2010, must be phased out, while phasing in more subsidies for renewables, which only grossed $60 billion in 2010 [6]. In a market-based energy economy, such statistics need to be reversed in order to obtain the desired evolution. A firm line of policy and a veritable socio-technical paradigm-shift are required to push local and global communities in the right direction – essentially everyone will play a role in the ongoing transition. Theophrastus' suspicions of human impact on the world have long ago been ascertained and proven. Now it is time to use this fact to the advantage of the human population and the environment- it is time for a true leap to renewable energies.

1.2 Solar Energy and Photovoltaic Solar Cells

1.2.1 Solar Radiation and Energy

Electromagnetic (EM) waves are considered a form of energy which is emitted and absorbed by charged particles as they travel through space and time. Therefore, any electromagnetic wave carries with it a certain quantity of radiant energy. Similar to other wave-phenomena in physics, an important property of EM-waves is its frequency,f, which is related to the wave velocity, v, by the relation given in Eq. 1-1.

$$v = f\lambda \qquad \text{Eq. 1-1}$$

Where λ is the wavelength of the EM wave. Radiant energy can be invisible or visible to the human eye, depending on the value of the wavelength. Additionally, the wavelength indicates the energy of an EM-wave. Quantum physics postulates that EM-waves are emitted as discrete bundles of energy, or *quanta*, or more commonly, photons. The energy, E, contained by a photon is defined below, in Eq. 1-2.

$$E = hf = \frac{hv}{\lambda} \qquad \text{Eq. 1-2}$$

where h is Planck's constant. This is what is known as irradiative energy.

EM-waves are emitted by so-called thermal radiators. The idealized thermal radiator is known as a black body, which absorbs all incoming irradiation, and, in thermal equilibrium, re-emits it all isotropically. The thermal radiator, and therefore the black body, is characterized by an emission spectrum according to its temperature. Essentially, any physical body is a thermal radiator, but the most important one in our solar system, and the one which most closely assimilates the behavior of a black body, is the sun. With a surface temperature close to 6000 K, the sun's radiation emission spectrum is described by two quantities, the spectral power density, $P(\lambda)$, and the photon flux density, $\phi(\lambda)$. As the emission and absorption of EM-waves occur in quanta or photons, the quantities describing an emission spectrum must link the emitting body to a certain photon distribution. Therefore, the photon flux describes the number of photons per unit time, unit area, and unit wavelength which are being emitted. Meanwhile, the spectral power density is a measure of incoming power per unit wavelength per unit area. Thereby, the two quantities are linked through the photon energy defined in Eq. 1-2. The relation between spectral power density and photon flux is given in Eq. 1-3 below.

$$P(\lambda) = \phi(\lambda) * E = \phi(\lambda) * \frac{hv}{\lambda} \qquad \text{Eq. 1-3}$$

Integration of the spectral power density of the sun over its entire emissive spectral range yields the power density, i.e. energy per unit area, of the sun.

Losses of irradiative energy, or more precisely, the spectral power density, will occur when the EM-waves of the sun are passing through the earth's atmosphere. The total energetic loss to the atmosphere will therefore depend on the path length within the boundaries of the atmosphere, and thus the geographical position where the measurement is taking place. In order to quantify this measure, the *optical air mass* is defined as the ratio of the distance travelled to the shortest path length of the EM-waves. The optical air mass, or AM value, is defined according to the zenith angle of a geographical location,θ, as given in Eq. 1-4.

$$air\ mass = AM = \frac{1}{\cos(\theta)} \qquad \text{Eq. 1-4}$$

The air mass is an important value because it gives not only a measure of energy lost to the atmosphere, but it permits for a standardization of test conditions. In order to set an industry standard, the spectral response corresponding to the emissive spectrum at AM1.5, i.e. a zenith angle of 48.2 degrees, is always reported when referring to solar cells. An illustrative schematic of optical air mass considerations is shown in FIGURE 1-1 seen below.

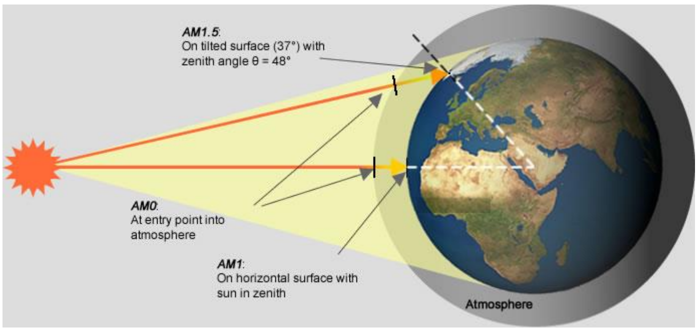

FIGURE 1-1: Path lengths of solar radiation through the earth's atmosphere. The figure is adapted from [9]

When speaking of solar energy, it is therefore important to be aware of one's geographical location. The AM-value will decidedly scale the spectral power density distribution. For reference, the spectral power density distribution is usually given for AM0, which is defined as the position outside the earth's atmosphere. A figure of the spectral power distribution is provided in FIGURE 1-2.

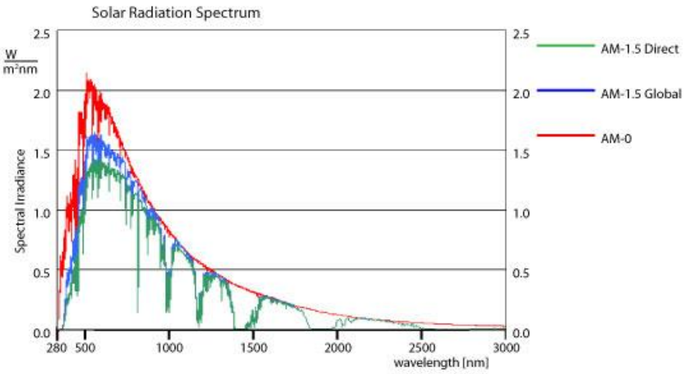

FIGURE 1-2: Spectral power density distribution of the sun for different AM-values. The figure is adapted from [9].

The power density impinging on earth's surface denotes the amount of irradiative energy which is readily available due to the sun. It is common practice to distinguish between *direct sunlight* (reaches the earth’s surface without interference from atmospheric particles), the *diffuse sunlight* (scattered by the atmospheric particles), and the *albedo* (reflected from the earth’s surface). The global power density measured is the combination of these three. As such, the value of the integrated AM1.5 spectrum is defined as $1000\ \mathrm{W/m^2}$. When referring to solar energy, it is indeed the spectrally integrated power density at a given AM-value that is being evoked.

The global solar resource is enormous, and the earth receives a tremendous amount of it. It is estimated that in one hour of noontime summer sun, the United States mainland receives enough solar energy to meet its annual electricity demand. Moreover, the amount of solar radiation striking the earth in one day is enough energy to satisfy our population for 27 years [10].

1.2.2 Harvesting Solar Energy

There are many potential ways to harvest the energy coming from the sun to the earth’s surface, and to a certain extent, boils down to a matter of definition. Wind energy is a result of temperature- and pressure gradients across the globe, ultimately caused by the incoming solar radiation. Likewise, any kind of biomass is a down-the-line product of the solar energy which allows for plant growth on earth. In such cases one refers to *indirect* solar energy.

The solar energy which is converted directly from sunlight into electricity, and not through intermediary media, is aptly named *direct* solar energy. Today’s solar energy applications are essentially concentrating solar power (CSP) and photovoltaic (PV) solar cells. CSP systems are based on the concentration of sunlight using mirrors and lenses. The dominant CSP systems are: the parabolic trough, the concentrating linear Fresnel reflector, the Stirling dish, and the solar power tower. All four systems are constructed so that the concentrated beam of sunlight heats a working fluid- in many cases water. The heated working fluid may be used directly in electricity production, or stored to preserve the thermal energy for later use.

PV solar cells are based on the *photovoltaic effect*, a process by which a voltage difference is generated in a material upon the absorption of photons. The material in question is a semi-conductor, due to its well suited opto-electrical qualities. Semiconductor materials are materials that act as insulators at low temperatures and conductors at higher temperatures. Due to the distribution of energy states in this type of material, one can define certain bands of states, namely the *valence band*, the forbidden band (usually referred to as the *band gap),* and the *conduction band*, in order of increasing energy. The valence band pertains to states where occupying charge carriers have little freedom for movement. The conduction band, on the other hand, pertains to states where charge carriers have freedom to move, i.e. conduction may occur. Finally, the band-gap consists of states which are not energetically feasible for the charge carriers in the semi-conductor, due to the inherent structure of the material.

A voltage difference is established in the material as a result of charge carrier generation, separation, and collection. When a photon is absorbed in a solar cell, an electron (negatively charged carrier)-hole (positively charged carrier) pair is generated in the valence band as a result of the energy transmitted in the process. If the photon energy is sufficiently large, i.e. superior to the energetic difference between the ‘lowest’ conduction band state and the ‘highest’ valence band state, the electron may occupy a state in the conduction band, and thus separate from its positive counter-charge; the hole.

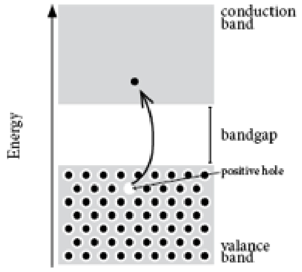

FIGURE 1-3: Band diagram of intrinsic crystalline silicon during charge carrier generation. Figure is adapted from [11]

This process is depicted in FIGURE 1-3, which shows a typical band diagram of intrinsic crystalline silicon (c-Si) at thermal equilibrium. Thereby, the charge carriers, now separated from each other by an energetic gap, must somehow be forced to conduct in order to create a current or build a voltage in the material. To this effect, an electric field, or electrical potential gradient must be present in the material. This is where two other characteristic properties of semiconducting materials play a vital role – the possibility to *dope* the material with positive or negative charge carriers, and the formation of energetic *junctions* when two oppositely doped semiconductors are associated. The creation of such a junction occurs due to diffusion of charge carriers from one material into the others. Because the electric charge of the diffusing free carriers is opposite to that of the free carriers in the material being diffused, the carriers will neutralize, thus leaving behind a host material with a net charge inequality. Meanwhile, the same process is occurring in the second semiconductor material, resulting in a junction, also known as the *depletion region*, between two oppositely charged semiconductor materials. Consequently, an electric field and a voltage potential have been set up, which act as a vector for conducting free charge carriers in the semiconductor. Thereby, the collection of charges at opposite ends of the semiconductor, and thus the electric field, may be realized. At this point, a current or voltage is readily available to an end user, and only the electrical wiring is necessary to harvest the solar energy.

1.2.3 Solar Cell Generations

Current PV solar cell technologies may be grouped into three categories. Although the solar cell industry is still relatively young, the pace of innovation, research, and development has resulted in three *generations* of solar cells per today. The *first generation* consists of crystalline silicon (c-Si) solar cells; the first solar cells to be commercially exploited and produced on a large scale. First generation solar cells are high-cost and high-efficiency components, obtaining efficiencies between 20 and 25 percent. Such solar cells largely employ a structure of one junction between n-doped c-Si and p-doped c-Si. The reason for the elevated prices of first generation solar cells is the level of purity which is required for the crystalline material, and consequently, high production costs. Furthermore, these types of solar cells are subject to the *Shockley-Queisser* limit, a balance limit which refers to the maximum theoretical efficiency of a p-n junction solar cell [12]. This limit, which is based on a balance of losses inherent to the solar cell material and the junction, is considered to be 33.7% for first generation solar cells.

Second generation solar cells are low-cost yet lower efficiency devices, reaching conversion efficiencies between 10 and 15 percent. Such solar cells are thin-film devices, and, as the name implies, can be deposited as single, thin layers. This is because thin-film technology employs a different type of material, most commonly hydrogenated amorphous silicon (a-Si:H), copper indium gallium selenide (CIGS), and cadmium telluride (CdTe), which exhibit entirely different absorption levels than the c-Si material. The benefit of this type of solar cells is therefore the reduced production costs and increased production rate. Thin-film producers enjoy a 20 percent reduction in production cost compared to that of crystalline solar cells [13]. It is expected that the gap in production costs between first and second generation solar cells will continue to grow, as large industrial powerhouses are heavily investing in thin-film technology research and development [10].

The optimal solar cell technology, which can obtain high efficiencies at low cost, is commonly denoted as *third generation* technology. There exists no such device as of today and third generation solar cells are limited to laboratory research. Several research groups and industrial partners have theories for how to surpass the Shockley-Queisser limit [12]. These theories are, for example, based on manipulations of incoming light or the absorbing material, such that electrical and optical losses in the device will reach a bare minimum. For the time being, however, this is a research-based field without commercial application.

The solar cell market is, as previously noted, dominated by first generation solar cells. However, the global PV market has accelerated over the past decade, demonstrating a 53% compound annual growth in PV shipments [10]. While the United States were the major market share holder at the entry of 2000, they were surpassed, first by the Japanese, then by the Germans, and finally ceded their place in the market to China and Taiwan. The Japanese market surge originates from a subsidy program started in the mid-1990s, while the European market growth stems from German feed-in tariff solutions implemented in 2000, in order to boost renewable energy production of electricity. This project was streamlined in the following years, and adopted by many other European nations in the last half the decade. China and Taiwan demonstrated their ability to invest and scale up production quickly, while substantially reducing manufacturing costs.

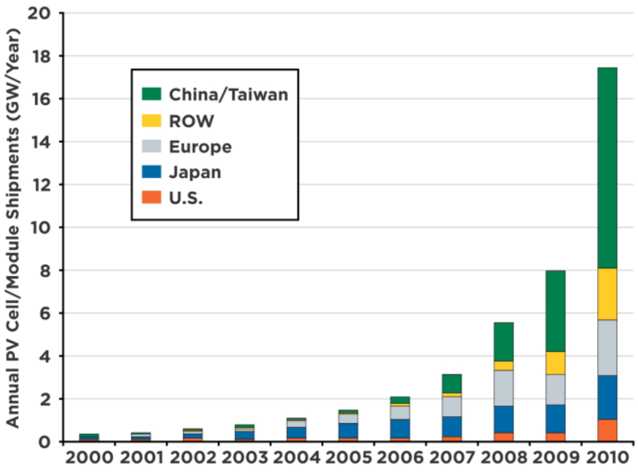

FIGURE 1-4: Global market developments in PV shipments. The figue is adapted from [10].

While the PV shipments have historically been dominated by c-Si solar cells, the thin-film industry has grown at a rapid pace during the past decade. In 2003, the market share for thin-film PV technology was 5%, the remaining 95% pertaining to c-Si. As shipments of CdTe and a-Si have rapidly expanded, so has the thin-film market share. By the end of 2010, the thin-film technology market share was

13% of global PV-shipments [10]. The evolution of the PV shipment market is shown in FIGURE 1-4 above.

1.3 Hydrogenated Amorphous Silicon Solar Cells

1.3.1 Choice of a-Si:H for PV Technologies

Although a-Si was the first material to be applied in thin film technology, it has failed to take the position as market leader in this field, yielding its place to both CdTe and Copper Indium Gallium Selenide (CIGS) [13]. The two latter material types have the advantage of yielding higher efficiencies, and having band-gaps and material properties which are well suited for thin-film solar cell applications. Meanwhile, a-Si:H continues to be a strong and suitable option for thin film PV. One reason for this is that industry, and the scientific community, are well acquainted with the amorphous silicon material – it is one of the most studied photovoltaic materials. Simple and low-cost deposition methods have been developed accordingly. Moreover, silicon is one of the most abundant materials on earth. This poses a major advantage to CdTe solar cells, as tellurium (Te) is a rare earth element (present at 1-5 parts per billion in the Earth's crust). Furthermore, silicon is a non-toxic material, which is of utmost importance for sustainable, large scale applications [14].

1.3.2 Material Structure of a-Si:H

The difference in material structure between amorphous and crystalline silicon is revealed by the name of each substance. While c-Si offers a crystalline structure, with constant bond lengths and angles throughout the entire material, a-Si:H does not provide such long-range order. Therefore, the a-Si:H material structure is complex and unpredictable. A coherent and complete understanding of the microstructure of a-Si:H is still lacking. The common and traditional interpretation of the a-Si:H material is that it forms a *continuous random network* (CRN). The random variations in bond lengths and angles in a-Si:H lead to certain combinations of these which are energetically unfavorable. Consequently, the potential interatomic bond in question will not form, thus leaving behind unpaired connections in the amorphous network, known as *dangling bonds* (DBs). Dangling bonds are denoted as *coordination defects,* which entails a mismatch between the coordination numbers of adjoining atoms in a material, i.e. number of atoms which an atom is energetically disposed to bond with. *Such* coordination defects impede the movement of free charge carriers within the material structure, i.e. the material conductivity. Initially, the large defect density in a-Si material, reaching levels of 10^{21} cm^{-3}, was though to render the material unsuitable for PV applications [15].

More recent studies of the amorphous material structure yield results which indicate the presence of other types of defects than solely DBs [16]. The presence of so-called nanovoids and vacancies within the amorphous network implies a configuration which is not wholly randomized, as the CRN-model proposes. Moreover, these defect zones in the material have been shown to be characterized by clusters of hydrogen, some of which are thought to adopt bonding configurations that yield DBs [17] [16]. As such, today's research implies that a-Si:H is better described as a disordered network which is modulated by the existence of hydrogenated voids and vacancies. The aptly named Disordered Network with Hydrogenated Vacancies (DNHV) model implies that DBs caused by strained Si-Si bonds or broken Si-H bonds are not the only source of defects within a-Si:H [18].

1.3.3 Doping a-Si

As explained earlier, the photovoltaic effect requires doped material in order to collect charges. The purpose of doping a material is to force a doping agent to adopt the coordination number of the host material. By doping the host material with atoms with a different coordination number, a charge deficit (i.e. a free electron) or a charge surplus (i.e. a free hole) is inferred. This physical phenomenon is figuratively depicted in FIGURE 1-5. The free charge carriers introduced will render the material more conductive, and the material is therefore said to be doped. During initial characterization studies, failure to dope the amorphous material was considered a normal consequence to the amorphous structure and its large density of coordination defects – as dopants would assume their natural coordination number and simply form bonds with DBs [15].

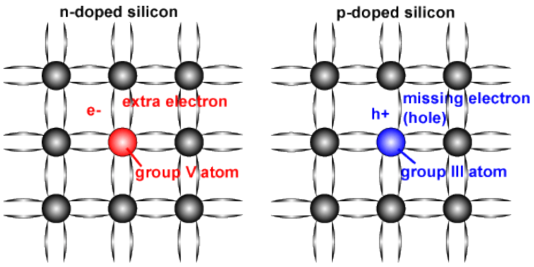

FIGURE 1-5: Schema of the principle of doping. The figure is adapted from [19].

This effect is, however, deterred by the presence of hydrogen (H) in the a-Si:H, as the H-atoms passivate (i.e. bond with) DBs in the a-Si:H, thereby reducing the defect density to $10^{15} – 10^{16}$ cm^{-3} [20]. Therefore an alloy between a-Si and hydrogen, or *hydrogenated amorphous silicon* (a-Si:H) is favorable for solar cell applications, and is the current standard in device grade applications. Therefore, when speaking of amorphous silicon solar cells, it is indeed a-Si:H that is referred to.

1.3.4 Optical Properties of a-Si:H

One of the most interesting aspects of amorphous silicon, which also clearly distinguishes it from its crystalline counterpart, pertains to the optical properties of the material. The optical properties of a-Si:H are characterized by its absorption coefficient and its optical band gap. Due to the disorder of a-Si:H, the material acts as a direct bandgap semiconductor. This means that the momentum of the electrons and holes is considered equal in the conduction band and the valence band. Crystalline silicon is an indirect bandgap semiconductor. In practice, this means that the momentum of induced charge carriers must be altered before they can occupy higher energy states – a process which requires parts of the absorbed energy. However, in amorphous silicon, the energy states are ‘relaxed’ to a point where they impose direct band-gap behaviour. The result of a direct band-gap is that the absorption coefficient of the material is much higher. As the charge carrier momentum mismatch is not an issue, more of the incident irradiation may actively participate in charge carrier transition across the band gap. In the visible part of the solar spectrum, a-Si:H absorbs up to two orders of magnitude more than c-Si. Therefore, a 1-μm layer of a-Si:H is sufficient to absorb 90% of the incoming visible light [15].

1.3.5 Band Diagram of a-Si:H

As opposed to the well-defined energy bands and ranges of crystalline silicon material, the energy bands of hydrogenated amorphous silicon form a continuous distribution with no abrupt cessation of states [15]. Due to the long-range disorder in the a-Si:H network, certain energetic states of the valence and conduction bands are located within the traditional band gap (i.e. forbidden energetic range of the crystalline network). These are named conduction and valence band *tail states*, as they are formed at the edges of the conduction and valence bands. According to the CRN-model discussed earlier, these states are considered as extensions of their respective bands, and as such are interpreted as strained inter-atomic bonds within the a-Si:H amorphous network structure [15].

Meanwhile, in correlation with the DNHV-model, it has been proposed that energetic states within the sub-bandgap region have their own unique bandgap. In this regard, the tail states are considered as the superposition of different bandgap energies stemming from defects in the a-Si:H [21]. The DBs are represented energetically in the band diagram of a-Si:H as *defect states*, located between the tail states. DBs form *amphoteric states*, meaning that they have three possible charge states: positive, neutral or negative. This results in defects which are capable of acting as electron donors and electron acceptors, thereby becoming centres of *recombination* of charge carriers. According to the DNHV-model, there exists additional charged defect types in the amorphous material which allow for different energy transitions than between a positive, a neutral, and a negative state [17]. Effectively, the defects form allowed energy states deep within the band gap of the material. The defect states and the tail states are denoted *localized* states due to the fact that there is almost no energetic overlap therein, thus providing traps to charge carriers in their proximity. The conduction and valence band states are called *extended states*, as these contain states that overlap energetically, and so allow for free charge carrier movement. Because of this altered band structure, the *mobility band gap* is defined as the energetic distance between the extended states. This is useful when characterizing a-Si:H, as the traditional band-gap definition is only a measure of the energetic distance between the valence and conduction bands. However, because the tail states also provide localized traps for free charge carriers, these are omitted from the permitted energy states for free charge carriers by introducing the mobility band gap, E_{mob}. A schematic of a-Si:H band structure is seen below, in FIGURE 1-6.

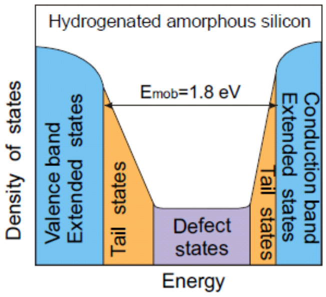

FIGURE 1-6: Band diagram of a-Si:H. The figure is adapted from [22].

The distribution of defect states in the amorphous material is thought to play an important role in the behaviour of the solar cell. It has been shown that optical and electrical properties of the amorphous material are highly dependent on defect density and defect density distribution, and these are therefore considered to be vital characteristics of the amorphous material [15]. This will be discussed further in Chapter 2 of this report.

1.3.6 The PIN Structure of a-Si:H Solar Cells

As opposed to c-Si solar cells, a-Si:H solar cells are not based on a single p-n junction. This is due to the fact that energetic conditions yield a situation where the dopants will assume configurations in the amorphous network which yield higher defect concentrations. Consequently, defect-compensated donors and acceptors in the doped layers cause increased recombination rates, thus lowering charge carrier *mobility* and *lifetime* in the material [15]. For this reason, a relatively thick intrinsic a-Si:H layer is sandwiched between thin n-doped and p-doped a-Si:H layers. The doped layers ensure that an electric field is generated across the solar cell, while the intrinsic layer acts as the absorber layer of the solar cell device. Therefore, contrary to the p-n junction, whose operation is dominated by diffusion of minority carriers, the dominant mode of charge carrier transport in a-Si:H solar cells is electrical drift of majority carriers. The electrons are collected in the n-doped layer, whereas the holes are collected in the p-doped layer. The most common a-Si:H solar cell structure is the superstrate configuration: p-doped layer, intrinsic layer, n-doped layer, also known as *pin-device*. This device structure is beneficial for overall charge transport due to a combination of two a-Si:H material properties. Firstly, holes have a mobility-lifetime product in intrinsic a-Si:H material which is considered to be lower than that of electrons, meaning that they will recombine sooner as they propagate through the intrinsic layer. Secondly, the absorption spectrum of a-Si is such that light is not absorbed homogeneously throughout the intrinsic layer, where a higher proportion of incoming sunlight is absorbed in the first couple of nanometres (nm) of the material [15]. Thereby, employing the device structure as seen in FIGURE 1-7 below will infer the least possible amount of losses during charge carrier transport through the device. Meanwhile, it should also be noted that the nip-configuration is successfully employed in solar cell fabrication.

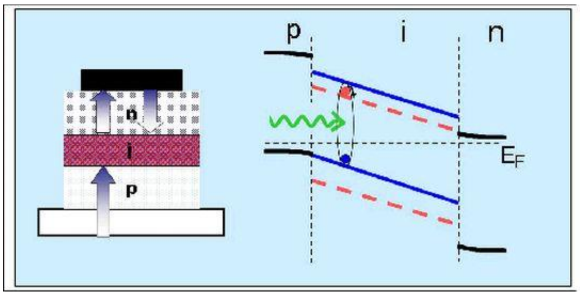

FIGURE 1-7: pin-device and its corresponding band diagram. The figure is adapted from [23].

1.3.7 The Staebler-Wronski Effect

Optical Efficiency Losses in Solar Cells

Efficiency losses *within* the solar cells (i.e. neglecting the effect of contact and wiring ohmic losses) have several different sources. Globally, the loss mechanisms can be grouped into two categories: optical- and collection-related mechanisms. The optical loss mechanisms occur due to spectral mismatch, reflection at the solar cell interface, shading, or insufficient transmission. Shading losses are inevitable when metal contacts and wirings are placed on top of a solar cell. Thereby, a fraction of the incoming sunlight will be unavailable for absorption. Reflection is caused by the difference in refractive indices in air and the medium of the first solar cell layer. Currently, anti-reflective layers are inserted in the top part of solar cells in order to reduce this effect. Transmission loss means that the sunlight which physically enters the solar cell is not absorbed. Such losses occur because the solar cell's absorber layer has a finite thickness and because the absorption coefficient of the material is imperfect (only the ideal black body absorbs all incoming radiation). Transmission losses can be reduced by increasing the optical path length of the sunlight in the material, which can be obtained by increasing internal reflection and optimizing scattering at interfaces within the solar cell. The largest source of losses, whether optical- or collection-related, is the spectral mismatch in a solar cell. Spectral mismatch denotes a difference in incoming photon energy and band gap energy, assuming that the photon is absorbed by the solar cell material. If the incoming photon energy is larger than the band gap energy, then the difference will be lost as heat to the absorbing material through a process known as *thermalization*. Meanwhile, if the energy of the incoming photon is inferior to that of the band gap, then the photon energy is too small to be absorbed by the material and, as such, is unavailable to power conversion in solar cells. It is estimated that around 55% of all sunlight is not usable by PV solar cells due to spectral mismatch [24].

Collection Losses and Recombination

As opposed to the optical losses, the charge carrier collection-related loss mechanisms are due to the electronic properties of the solar cell material. Charge carrier collection is impeded at two major instances in the solar cell – in the *bulk* material, i.e. where the carriers are generated and separated, or at the contact interfaces, i.e. where the carriers are physically collected. In both cases, the losses are due to the process of *recombination*. Recombination is a process by which two charge carriers of opposite polarity annihilate each other. The process is the complimentary action to the generation of charge carriers by photons. At the surface and metal contact interface, recombination is defect-mediated, as structural imperfections at these sites will function as charge traps and thereby spur recombination. In the bulk of the solar cell, which is the intrinsic layer in the case of the pin a-Si:H solar cell, different mechanisms of recombination exist for a-Si:H. The mechanisms are termed *band-to-band* recombination, *Auger* recombination, and *Shockley-Read-Hall* (SRH) recombination. In band-to-band recombination, an electron from the conduction band recombines with a hole from the valence band, emitting a photon in the process. The wavelength of the emitted photon corresponds to the energetic difference between the hole and electron in question. In Auger recombination, an electron gives off its excess energy upon recombination to another electron in the conduction band. The recipient electron experiences an increased kinetic energy, and most likely thermalizes shortly after. SRH recombination is a defect mediated mechanism, where a hole and an electron recombine through means of a defect site in the band gap. The energetic requirement for this transition is less than in the two other cases, and is therefore more likely to occur in a defect-rich material. In a-Si:H, both Auger and band-to-band recombination are negligible compared to SRH recombination [15].

The Staebler-Wronski Effect (SWE)

Discovered in 1977 by David L. Staebler and Christopher R. Wronski, the Staebler-Wronski effect was described as a significant decrease in dark conductivity and photoconductivity as a result of prolonged light soaking (LS) of a-Si:H material. The schematic figure of this experimental result is reproduced in FIGURE 1-8 below.

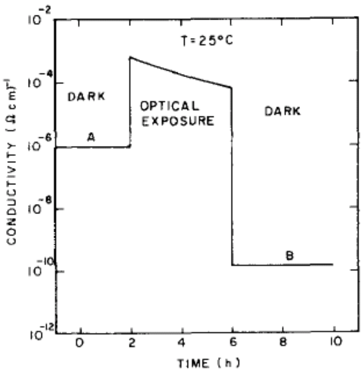

FIGURE 1-8: Observed change in dark and illuminated conductivity as a result of light soaking. The figure is adapted from [25].

Moreover, it was observed that these effects were *metastable*, i.e. reversible, as the process of *thermal annealing* caused recovery of conductivity in the amorphous material [25]. Thermal annealing (TA) is a process where a material is heated at a given temperature for a given amount of time. There exists a thermal threshold above which the thermal annealing is effective in a-Si:H, and temperatures above 100 degrees Celsius are standard practice [26]. At standard test conditions (STC), the degradation process stabilizes after about 1000 hours of light soaking, after which the performance level of the solar cell stabilizes [27]. In a-Si:H solar cells, the Staebler-Wronski effect causes reductions in efficiency of 10%-30%. As such, the SWE is one of the major obstacles of using a-Si:H in production of high efficiency photovoltaic devices.

While the true cause of the effect continues to elude the scientific community, it has been shown that the concentration of defects in the amorphous material increases by up to two orders of magnitude before stabilization, reaching levels of 10^{17} cm^{-3}, as depicted in FIGURE 1-9 [28]. Furthermore, crystalline silicon is not prone to the SWE, and even microcrystalline material is almost completely resistant to the effect. As the outcome of SWE is a higher defect density, much attention is given to uncovering the nature of the defects within the amorphous material. Nearly 40 years' worth of research exists on the characterization of defect creation dynamics and defect characteristics within a-Si:H. Although a complete and coherent model for the degradation process is lacking, it is common consensus that the presence of hydrogen within the a-Si:H structure plays a large role in the creation mechanisms of metastable defects. It has been shown that hydrogen bonding configurations change as a result of LS [29]. Because hydrogen atoms within the amorphous silicon material pacify DBs in the structural framework, it is believed that such changes in bonding configurations lead to alterations in defect density and defect density distribution.

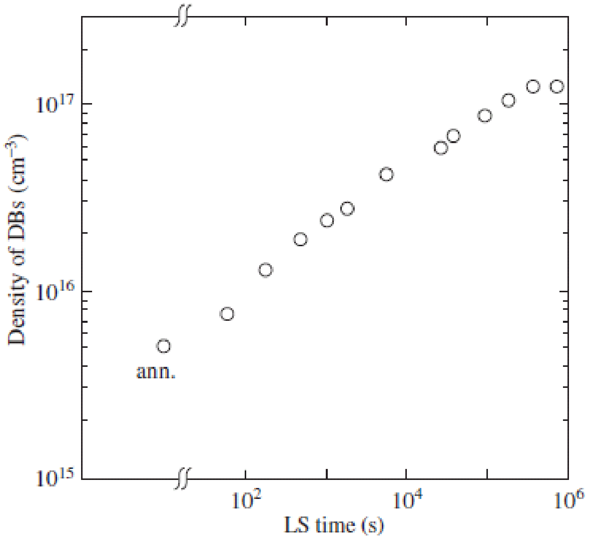

FIGURE 1-9: Defect density evolution with light soaking time from electron spin resonance measurements. The figure is adapted from [28].

1.4 Project Purpose and Report Outline

1.4.1 Project Purpose

The purpose of this master thesis project is to actively contribute to the development and advance of renewable energy sources. More specifically, the thesis is dedicated to the progress of a-Si:H solar cells in the PV market, as the material holds great potential in a day and age when thin-film solar cells are gaining more and more interest. Contributing to a complete and coherent study of a-Si:H solar cell characteristics is therefore the superior aim of the project. A study of the Staebler-Wronski Effect through *light induced degradation* (LID) of a-Si:H solar cells is effectuated in order to shed new light on degradation characteristics and mechanisms of the amorphous silicon material. Controlled degradation experiments, using in-situ measurement setups for continuous records of solar cell characteristics, are carried out. Thereby, the investigation aims to map the degradation characteristics of intrinsic a-Si:H under particularly well-controlled experimental conditions. The aim of this master thesis is to carry out an in-situ survey of the effect of temperature, intrinsic layer thickness, and *hydrogen-to-silane gas flow rate ratio* (R) on the degradation of hydrogenated amorphous silicon solar cells.

1.4.2 Outline of Report

This project report consists of seven chapters. Chapter 1 and Chapter 2 are devoted to the introductory information and theoretical considerations which form the foundation of this master thesis. Chapter 3 offers a detailed description of the methods and experimental procedures which were employed throughout the project. Herein, the details of the equipment and material depositions are thoroughly described. Chapters 4 to 6 are outlined as a combination of result presentation and discussion. Due to the large amount of experimental data compiled throughout this project, it is necessary for the sake of clarity and order to divide the results into several chapters. Moreover, this structure lends itself logically to the nature of the experimental results which pertain to three different states of the solar cells – as deposited (Chapter 4), degraded (Chapter 5), and annealed (Chapter 6). The discussion and analysis of the results for each of these stages is consequently located within the corresponding chapter. The final chapter of the report, Chapter 7, summarizes the key finding of this project and contains recommendations for future work based on this master thesis.

Chapter 2: Theoretical Background

2.1 Defect Density Distribution

The electronic properties of hydrogenated amorphous silicon are distinctly marked by its continuous distribution of states (DOS). As mentioned in the previous chapter, the energy states in the amorphous material are categorized as three separate types of states – extended states, tail states, and localized states. These three types of states constitute their own bands, as seen in the schematic in FIGURE 1-6, and are each subject to different DOS. The extended states, which correspond to the states in the valence and conduction band, are energetically overlapping. This makes it possible for free charge carriers to move in the material, i.e. the charge carriers have a certain concentration *and* non-zero mobility. Therefore, the extended states are traditionally considered to represent unstrained Si-Si bonds and Si-H bonds in the amorphous network [15]. The extended states band is delimited by the characteristic energy for which the appearance of tail states occurs, E^{tail}. Within the extended states band, the DOS is generally assumed to be distributed according to a parabolic function, which is modulated by the given energy level, as well as the aforementioned E^{tail}. The density of states in the extended states is therefore given by relations in Eq. 2-1and Eq. 2-2 found below.

$$N_{CB} = N_C^0 (E - E_C)^{0.5} \tag*{Eq. 2-1}$$

$$N_{VB} = N_V^0 (E_V - E)^{0.5} \tag*{Eq. 2-2}$$

N_{CB} and N_{VB} represent the DOS in the conduction band and the valence band, respectively. N_C^0 and N_V^0 describe the parabolic distribution of states in the conduction and valence band, respectively. E_C and E_V represent the conduction band edge and the valence band edge, respectively. In semiconductor physics, the difference between these two characteristic energies defines the bandgap, E_{gap}, of the material, as seen in Eq. 2-3 below.

$$E_{gap} = E_C - E_V \tag*{Eq. 2-3}$$

The tail states and the defect states constitute the localized states of the amorphous semiconductor material, i.e. where charge carriers have strongly reduced mobility and are consequently said to be trapped herin. Therefore, the energetic band which encompasses the localized states is an important parameter in a-Si:H, and replaces the conventional definition of the bandgap as defined in Eq. 2-3. The *mobility bandgap* is therefore defined as the difference between the characteristic energy of the tail states in the conduction band and the valence band, as defined earlier in this section. The mobility gap, E_{mob}, is defined in Eq. 2-4.

$$E_{mob} = E_C^{Tail} - E_V^{Tail} \tag*{Eq. 2-4}$$

E_C^{Tail} and E_V^{Tail} are the characteristics energy levels of the conduction and valence band tails, respectively. Traditionally, the DOS within the tail states is considered to be exponentially related to the difference between a given energy level and E_C^{Tail} or E_V^{Tail}, depending on which band is considered. Moreover, the tail states are often considered to represent the strained bonds between silicon atoms and hydrogen atoms in the amorphous structure [15] [26]. Tail states, as extensions of either the valence or conduction extended state bands, act as either electron acceptors or donors, respectively. Thus, the tail states represent one single energy transition for a charge carrier. Meanwhile, analysis of the a-Si:H may suggest that the tail states are caused by a disordered and anisotropic distribution of bond lengths, as a result of vacancies and voids within the material structure [21].

In contrast to the general consensus regarding extended states of a-Si:H, defining the tail states and the defect states has proven an elusive task to the scientific community. The defect states in a-Si:H give it some of its unique characteristics, and play a large role in the electronic performance of the material. It is naturally accepted that the types of defects, as well as the energetic and spatial distribution of the defects, impact the material, and ultimately, solar cell performance. Moreover, the proposed mechanisms of SWE rely on a sound definition of these parameters. The most widely accepted theory is that the defect states are synonymous with dangling bonds in the amorphous network, which ultimately act as trap states and recombination centers [26]. As noted in Chapter 1, the DBs are considered amphoteric in nature, and present two possible energy transitions for a charge carrier: from neutral state to negative state, and from positive state to a neutral state. Each of these energy transitions involves the capture of an electron. There exist several models of SWE, most of which are based on the role of hydrogen and DBs in defect creation and propagation [28] [30]. Alternative models involving a combination of vacancies, voids, and DBs within a-Si:H are suggested and documented [17].

Therefore, the DOS within the defect band of the amorphous material is of noteworthy importance to understanding the kinetics of charge carriers within a-Si:H, and, ultimately, the SWE. The standard model of DOS distribution in a-Si:H predicts that the defect states are distributed according to two Gaussians, each one centered at a characteristic energy which represents the average energy of transition for an electron to occupy the state. The two are related by the correlation energy, U, which represents the energy needed to add a second electron to a singly occupied (neutral) DB. The standard model considers this distribution to be valid for all positions within the material, and thus a uniform spatial distribution within the material. Meanwhile, this model fails to provide an explanation as to the origin of the DBs in the material [15].

Modeling studies suggest that another model of DOS distribution in the defect band may be more fitting to the characteristics of a-Si:H, namely the Defect Pool Model (DPM) [31]. The Defect Pool Model is based on the weak-bond – dangling-bond conversion model. Through an equilibration process governed by a minimization in Gibbs free energy, the lattice and DB density become fixed. The equilibrium DB density is calculated by minimizing the entropy of the system that is formed by silicon weak bonds, dangling bonds, and the silicon-hydrogen bonds. The DPM relies on a diffusing agent through the material, and proposes that the equilibration process by which the DB density and material structure are defined, is hydrogen mediated. Furthermore, DPM defines the mean energy of the electrons in the DB states as dependent on the charge state of the DB. Because the charged state is inevitably dependent on the Fermi level, the Fermi level influences the DB distribution. This also yields a heterogeneous spatial distribution of defects within a solar cell device. The DPM model attributes the tail states distribution to the weak Si-Si bonds in the material. Moreover, the distribution of the available defect sites, P(E), is called the *defect pool*. The defect pool is described by a Gaussian distribution, and is ultimately dependent on the Fermi level at the given position in the device. The DPM has proved capable of modeling doped and undoped material, making it a powerful tool in semiconductor analysis [14] [15] [31].

Meanwhile, it is necessary to underline once again that current research efforts reveal the possibility of other types of defects than mere DBs, as presented in the DNHV model [17] [32]. Several transitional energies have been identified within the material, suggesting the existence of other charged states than those incorporated by the amphoteric nature of the DBs [20]. Furthermore, the kinetics of the creation of metastable defects in the amorphous material still escapes a complete and coherent description which is consistent with all experimental findings. The CRN model and its associated interpretation of defects and the amorphous structure therefore lack a clear definition [26]. For example, experimental evidence suggests the existence of nanovoids and vacancies in a-Si:H [16] [18]. Thereby, the DNHV model, which elaborates the role of these in the creation of DBs and other trap states, is invoked. As such, the modeling work on DOS and defect density distribution within the a-Si:H material is not yet terminated.

2.2 Thermal Annealing

The metastable defects induced in the amorphous material by light soaking are, as the name implies, possible to remove. As any thermodynamic process is defined by an activation energy, it is natural that a certain amount of energy is required in order to create defects, and a certain amount of energy is required to remove them. A light soak can furnish the right amount of energy to create a defect, while a provision of a thermal load, i.e. thermal annealing, can overcome the energy barrier to reverse the process. This process is depicted FIGURE 2-1, seen below.

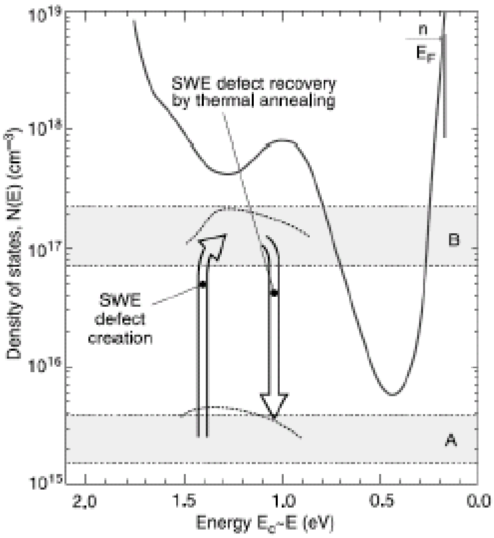

FIGURE 2-1: Energy barriers to defect creation and thermal annealing. Figure is adapted from [29].

Studies of annealing kinetics in a-Si:H have shown that this activation energy may vary according to the deposition conditions of the material, and thus, its quality [33]. Investigations on the effects of plasma frequency and deposition rate during deposition, which is explained in detail in the next chapter, show a range of possible activation energies of thermal annealing. Moreover, as the quality of the device degrades this activation energy of thermal annealing increases.

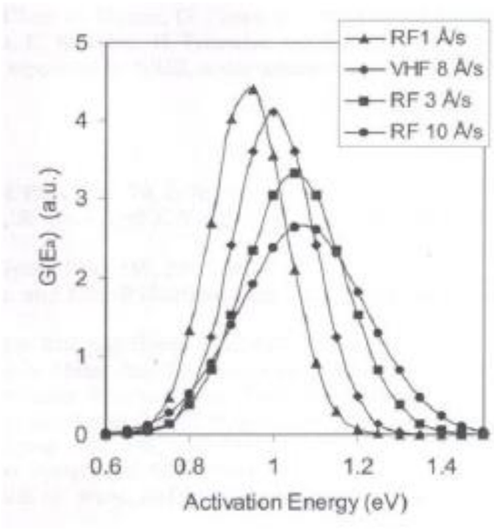

FIGURE 2-2: Activation energy distributions of thermal annealing of defects as a function of plasma frequency and deposition rate. The figure is adapted from [33].

This is illustrated in FIGURE 2-2, as seen above by the different distributions of annealing energies as a function of plasma frequency and deposition rate. It is clear that the distributions are centered about a lower activation energy as the deposition rate decreases, and the plasma frequency decreases. Typically, the defects which require lesser energy to anneal out of a material are denoted *soft,* whereas the defects which require more energy to anneal out of the material are denoted *hard.* Annealing studies indicate that the native defects within a material are typically hard [26].

Essentially, it is useful to think of the light induced degradation and thermal annealing as two continuously ongoing processes, resulting in an equilibrium of creation and annihilation of defects. Thus, increasing the activation energy of annealing equates a shift in this equilibrium towards defect creation. Meanwhile, providing more thermal energy to the system marks a shift in the equilibrium towards defect annealing.

2.3 Hydrogen Dilution

Among the existing techniques to reduce the Staebler-Wronski Effect is the possibility to dilute the silane ($\mathrm{SiH_4}$) gas with hydrogen (H) during deposition of the amorphous material [34]. Several reports show that solar cells with a-Si:H absorbers which are prepared under these conditions have a better performance after exposure to light than their undiluted counterparts. The deposition of solar cell material is described in Chapter 3 of this report, and the reader is referred here for a detailed discussion on this matter. Essentially, hydrogen is implemented as an additional feed-in gas to the deposition chamber, which consequently reduces the relative amount of pure silane gas. Thus, it is possible to define the hydrogen-to-silane gas flow rate ratio, or simply, H-dilution ratio, *R*, of the deposition gas, defined in Eq. 2-5, as the ratio of the gas flow rate of hydrogen gas to silane gas that enter the deposition chamber.

$$R = \frac{[\mathrm{H_2}]}{[\mathrm{SiH_4}]} \qquad \text{Eq. 2-5}$$

The increased hydrogen coverage of the growing surface due to higher values of *R* allows for precursors of silicon to diffuse for a longer time before settling in the amorphous structure. Therefore, the likelihood of forming energetically favorable bonds increases, which inevitably leads to an interatomic network which is less prone to defect and defect creation. The increased hydrogen coverage throughout the thin film deposition process also allows for enhanced defect passivation – most notably in the case of DBs in the layer being grown [35].

Moreover, imposing a certain hydrogen dilution is believed to increase the structural order of the amorphous material by removing the weakest silicon-silicon bonds in the network, and permitting growth radicals to reach energetic positions which are more favorable [35]. To understand this, it is useful to consider film growth as an equilibrium between etching and deposition. The etching process consists of hydrogen atoms impinging on the growth substrate and reacting with the film material, i.e. Si precursors, to re-form volatile substances, thus removing the Si. Because hydrogen preferentially reacts with weakly bonded silicon, it is believed that the weak silicon-silicon bonds are more efficiently removed from the growing film. Thus, the bonds which are often associated with formation of tail states and defect states in the amorphous material are, to a certain extent, removed during the deposition process due to increased hydrogen dilution ratios [35].

Thus, it is believed that hydrogen dilution increases the structural order of the amorphous material. This interpretation is consistent with the observation observations of higher material stress within films of increased hydrogen dilution ratios [35] [36]. Moreover, it has been shown that dilution of the Silane gas during deposition promotes the evolution of microcrystalline silicon (μc-Si:H). FIGURE 2-3 shows how the microcrystalline growth evolves with film thickness, t, and hydrogen dilution ratio, *R*. The figure is a rudimentary phase diagram, and indicates for which dilution ratios and thicknesses one can expect the different phases of a-Si:H.

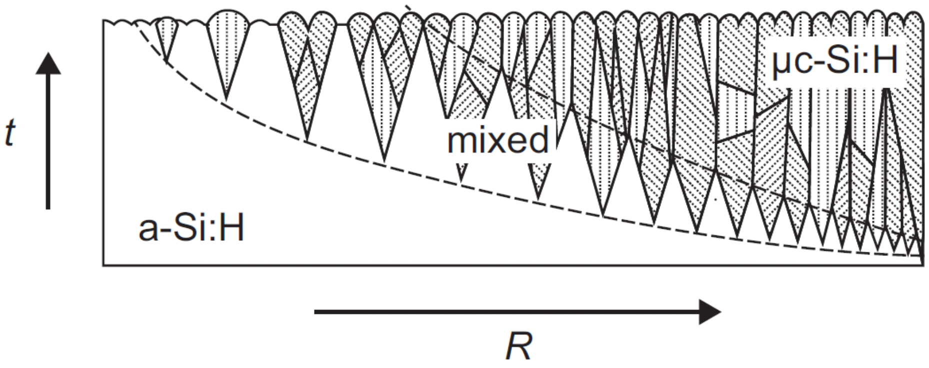

FIGURE 2-3: Schematic representation of the phase transition in amorphous silicon with increasing thickness and hydrogen dilution ratio values. The figure is adapted from [35].

Although this project does not treat microcrystalline phase of silicon, it is worth noting that this phases do not suffer from the SWE. Meanwhile, the mixed phase still contains sufficiently a-Si:H to degrade under light soaking, but due to a high initial density of defects due to non-passivated phase boundaries, the relative degradation is small [37]. Furthermore, the evolution towards a microcrystalline phase may be interpreted as an increase in structural order in the material, even when it is still in its amorphous phase.

Because the microstructure of the amorphous network is altered through hydrogen dilution, it is natural to expect the same to be true for other properties relevant to solar cell application. This is effectively ascertained in FIGURE 2-4, where the evolution of the absorption coefficient of a-Si:H is plotted with respect to the value of *R*. It is important to note that for values of *R* which exceed 30, the material is no longer amorphous and has crossed the phase boundaries exhibited in FIGURE 2-3.

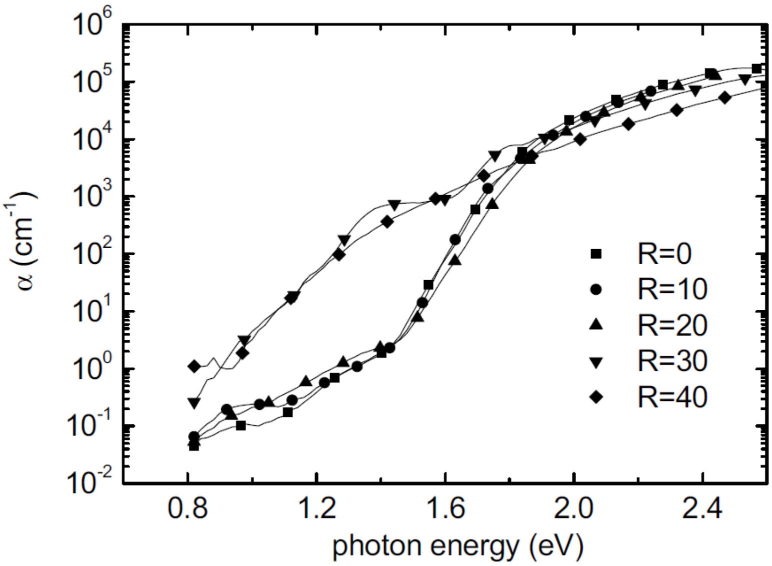

FIGURE 2-4: Absorption coefficient of a-Si:H for different values of hydrogen dilution ratio during intrinsic layer deposition. The figure is adapted from [35].

As FIGURE 2-4 demonstrates, the evolution towards microcrystalline material is accompanied by a clear decrease in absorptivity for longer wavelengths of light. When used in a solar cell, this effect will ultimately be reproduced in the performance of the device, and most certainly in the spectral response. The fundamentals of solar cell performance are explained in the next section of this chapter.

2.4 Solar Cell Performance

Solar cells are complex devices of which the functioning depends on a myriad of material parameters and opto-electronic properties. As is the case for most technical devices, a few representative parameters are consequently used as a standard for comparison. These parameters offer a quick, practical, and simple way of exchanging information about the solar cells because they give a well-balanced impression of their overall rating. Consequently, certain key measurements which effectively delineate the performance of a solar cell are outlined in this section.

2.4.1 Dark IV

The measurement of the dark voltage-current characteristic of a solar cell is ultimately a survey of its electronic properties. By imposing a bias voltage across the device via an external circuit, charge carriers are driven into the solar cell. Herein, the charge carriers will recombine due to the defects in the amorphous material. Therefore, the charge injection into the device, which essentially is the measured current during a dark IV experiment, is a quantitative measure of recombination in the device. Hence, the dark current is often referred to as the *recombination current* when referring to the a-Si:H. In a a-Si:H p-i-n device, the dark current is dominated by the rate of SRH recombination in the absorber layer. The recombination rate in the doped layer is usually neglected due to a low density of minority carriers as well as very the small layer thickness herein. Thus, the dark current can be approximated by Eq. 2-6, seen below [38].

$$J_D(V,T) = q\int_0^W R(x,V,T)dx \qquad \text{Eq. 2-6}$$

Where V is the bias voltage, T is the temperature, J_D is the dark current density, q is the elementary charge of an electron, W is the thickness of the intrinsic layer, and $R(x,V,T)$ is the depth, voltage, and temperature dependent recombination rate of the a-Si:H material. Swaaij *et al.* show that the recombination rate for a given position in the device is related to the recombination efficacy and the defect density, integrated over the quasi-Fermi levels of trapped charge as indicated by Eq. 2-7 below [39].

$$R(x,V,T) = \int_{E_{F_{p,t}}}^{E_{F_{n,t}}} \eta_R(x,E_t,V,T) * N_t(E_t,x)dE_t \qquad \text{Eq. 2-7}$$

Where η_R is the recombination efficacy, E_t is the energy level of the trap state, N_t is the density of trap states, $E_{F_{n,t}}$is the quasi Fermi level of negatively trapped charge, and $E_{F_{p,t}}$ is the quasi-Fermi level of positively trapped charge. It is important to underline that the density of traps, or defects, is not dependent on bias voltage or temperature. Rather, it is the recombination efficacy which is altered when such conditions vary. The recombination efficacy is derived from the Shockley-Read-Hall recombination statistics and, consequently, is a qualitative measure of the capacity of a trap or defect to serve as a recombination center [14].

Thereby, the dark current measurement of a p-i-n solar cell is an indirect measurement of the defect density within the absorber layer of the device. In the following two sections, the activation energy of the dark current and the voltage-dependent ideality factor, both of which are derived from the dark current-voltage characteristics, will be explained.

Ideality Factor

The dark JV curve exhibits an exponential profile at low forward bias voltages. Traditionally, the dark current density, J_D, in this bias voltage region is described via the well-established diode equation as seen below in Eq. 2-8.

$$J_D = J_0 \exp(\frac{qV}{nkT}) \qquad \text{Eq. 2-8}$$

Where $J_0$is the saturation current density, T is the temperature, k is the Boltzmann constant, q is the elementary charge, and n is the ideality factor. Hence, the ideality factor is often interpreted as a measure of how well a device approaches the ideal diode behavior, for which $n = 1$. For a-Si:H p-i-n solar cells, the ideality factor typically has a non-integer value between 1 and 2, which is accordingly associated with SRH recombination [14]. The voltage dependent ideality factor can be obtained through the method proposed by Deng and Wronski, as given by Eq. 2-9 below [40].

$$n(V) = \left[\frac{kT}{q}\frac{\mathrm{d}}{\mathrm{d}V}\left(\ln\left(\frac{J_D}{J_0}\right)\right)\right]^{-1} \qquad \text{Eq. 2-9}$$

Thereby, according to the interpretation of dark current described earlier in this section, the ideality factor is indirectly related to the change in density of traps which participate in recombination as the bias voltage increases or decreases. This interpretation is based on the fact that an increase in bias voltage causes splitting of the quasi-Fermi levels of trapped charge within the bandgap of a material [41]. As noted previously in this section, only the traps which are energetically distributed between these quasi-Fermi levels participate in recombination, and thus contribute to the dark current. Thereby, the ideality factor becomes a measure of the energetic distribution of defects in the solar cell device.

Thermal Activation Energy of Recombination

The activation energy of the dark current, and thus recombination, is calculated by Pieters *et al.* via a generic relation for any thermodynamic process, $X((kT)^{-1})$, where X is the given temperature dependent process. In the case of a-Si:H recombination, X represents the dark current, J_D, and the generic relation cited by Pieters *et al.* is accordingly adapted to yield the thermal activation energy of recombination, E_a^R, given in Eq. 2-10 [38].

$$E_a^R \triangleq -\frac{\mathrm{d}(\ln[J_D((kT)^{-1})])}{\mathrm{d}((kT)^{-1})} \qquad \text{Eq. 2-10}$$

Thus, the temperature dependence of the dark current can be determined through the calculation of the activation energy of the recombination of a p-i-n device. Pieters *et al.* also show that the activation energy is related to the mobility band gap of the intrinsic layer, E_{mob}, by Eq. 2-11, for the bias voltage range between 0.2 V and 0.7 V, where SRH recombination is dominant.

$$E_a^R = \frac{E_{mob} - V}{m_{th}} + 3kT \qquad \text{Eq. 2-11}$$

Where m_{th} is the thermal ideality factor. Pieters *et al.* showed through experiments and numerical modeling that m_{th} is equal to 2 and independent of voltage for intrinsic a-Si:H [38]. Kind *et al.* investigated the thermal ideality factor, as well as Pieters' approach to the calculation of the mobility band gap, and obtained results which are consistent with the theoretical models and predictions [42].

2.4.2 Illuminated IV

The illuminated current-voltage characteristic yields the solar cell performance under illumination and is the most common measurement to determine the quality of the device. Therefore, the IV-curve of a solar cell under illumination of the AM1.5 spectrum has become the industry standard for exchanging information about the characteristics of the device. In solar cell research, it is common to work with current density, *J*, instead of total current, and a typical illuminated JV-curve is shown below, in FIGURE 2-5.

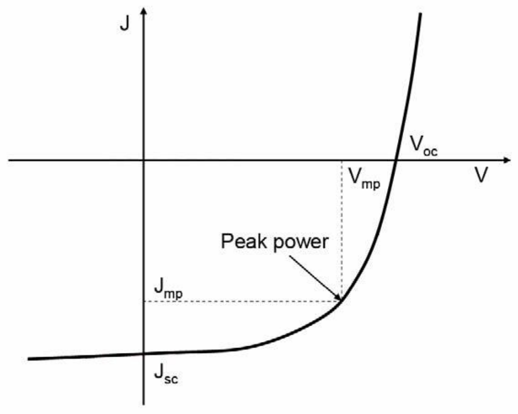

FIGURE 2-5: Typical current-voltage characteristic curve of a solar cell. The figure is adapted from [22].

The current-voltage characteristic is used to retrieve the so-called external parameters of the solar cells, namely the short-circuit current density, J_{SC}, the open-circuit voltage, V_{OC}, the fill factor, and the efficiency. As is shown on the curve, the J_{SC} is simply the current at zero voltage across the solar cell. Thus, the J_{SC} represents the maximum generation possible generation of charge carriers under the AM1.5 spectrum. The V_{OC} is found at the intercept of the JV-curve and the voltage axis, and represents the voltage for which no current flows in the device. This provides information about the strength of the internal electric field in the device, and thereby, the built-in voltage potential of the solar cell.

The maximum power point of a solar cell is defined as the point on the curve for which the product of current and voltage is maximized, as seen in Eq. 2-12.

$$\mathrm{P}_{MPP} = \max_{I,V}\{P\} = \max_{I,V}\{IV\} = I_{MPP}V_{MPP} \qquad \text{Eq. 2-12}$$

where I and V are the current and voltage, respectively. I_{MPP} and V_{MPP} are the values for current and voltage, respectively, for which the maximum power output, P_{MPP} is obtained. These points are also marked on the IV-curve shown in Figure 2.5 above. The efficiency of the solar cell, $\eta_{solar\ cell}$, is calculated in terms of this maximum possible power, and is defined in Eq. 2-13, seen below.

$$\eta_{solar\ cell} = \frac{P_{MPP}}{P_{IN}} \qquad \text{Eq. 2-13}$$

where P_{IN} is the incident power on the solar cell. As noted in Section 1.2.1 of Chapter 1, solar cell efficiency is usually considered in terms of the AM1.5 spectrum at an incoming intensity of $1000\frac{W}{m^2}$.

Finally, the fill factor of the solar cell is defined as the ratio of the maximum power point and the product of V_{OC} and I_{SC}. The fill factor, FF, reveals the characteristic shape of the IV-curve, and is defined in Eq. 2-14.

$$FF = \frac{I_{MPP}V_{MPP}}{I_{SC}V_{OC}} \qquad \text{Eq. 2-14}$$

The fill factor may be indirectly interpreted in terms of how large the shunt and series resistance losses of the solar cell are, relatively speaking. This implies that cells with a high fill factor have less dissipative losses of the generated photocurrent.

2.4.3 EQE

The *external quantum efficiency*, or EQE, of a solar cell is a compound entity which delineates the spectral absorption *and* charge carrier collection capacity in a solar cell. EQE may be defined as the ratio of number of charge carriers collected to the number of photons impinging on the device. As will be described in the following chapter, an EQE measurement is carried out by illumination of monochromatic light on a sample, followed by the subsequent current measurement. Thus, Eq. 2-15 is used to obtain the EQE.

$$EQE = \frac{electrons/_{sec}}{photons/_{sec}} = \frac{current/_{elementary\ charge,\, q}}{total\ photon\ power/_{energy\ of\ a\ single\ photon}} \qquad \text{Eq. 2-15}$$

The use of monochromatic light renders the EQE a measurement of the spectral sensitivity of the solar cell. Moreover, by measuring the EQE at short circuit condition, the relation between EQE and the short circuit current given by Eq. 2-16 is obtained.

$$J_{SC} = q\int_0^\infty \Phi(\lambda) * EQE(\lambda)d\lambda = q\int_0^\infty P(\lambda) * \frac{\lambda}{hc} * EQE(\lambda)d\lambda \qquad \text{Eq. 2-16}$$

where $\Phi(\lambda)$ is the photon flux density, $P(\lambda)$ is the spectral power density, λ is the light wavelength, c is the speed of light, and$h$ is Planck's constant. Ideally, the EQE of a solar cell has a rectangular shape; in this case it would be equal to 1 for wavelengths lower than λ_{gap}, i.e. the wavelength corresponding to the energetic bandgap of the solar cell, and equal 0 otherwise. Meanwhile, due to recombination losses, charge trapping, and reflection, the EQE across the entire spectral region is reduced. The response in the lower wavelength region is significantly reduced by absorption in non-active layers, i.e. the TCO and the doped p-layer in the case of the p-i-n structure. As depicted earlier in FIGURE 2-4, a-Si:H has an elevated absorption coefficient in the lower region of the light spectrum, which explains why the photons of corresponding wavelength are quickly absorbed in the first layers of the solar cell. As such, the EQE is a complex of several different physical processes in the solar cell device. Thus, it is not possible to extract the contribution of each individual process from the EQE measurement [43].

2.5 Efficiency Fitting

There exist a multitude of empirical relations which describe the light induced degradation of solar cells. In the analysis of time-dependent data presented in this project, the efficiency of the devices will be considered in terms of its relation to defect densities as proposed by Chen and Yang [44]. This relation is given by Eq. 2-17 below.

$$\eta \propto 1 - A * \log(N) \qquad \text{Eq. 2-17}$$

Where η is the solar cell efficiency, N is the defect density, and A is a device-related constant. Generally, defect creation in the solar cell is considered the as the sum of contributions from four different processes in the device: light induced creation of defects, light-induced annealing, thermally induced creation of defects, and thermally induced annealing. Redfield *et al.* proposed the reaction rate equation given in Eq. 2-18 to incorporate these four contributions [45].

$$\frac{\mathrm{d}N}{\mathrm{d}t} = C_1(N_s - N)R - C_2NR + v_1(N_s - N) - \ v_2N \qquad \text{Eq. 2-18}$$

Where N_s and R are the total density of potential defect sites and the recombination of light-generated carriers, respectively. C_1, C_2, v_1, and v_2 are constants corresponding to light induced creation of defects, light induced annealing of defects, thermally induced creation of defects, and thermally induced annealing, respectively. The solution of Eq. 2-18 is a stretched exponential function. Terakawa *et al.* combine this solution with Chen and Yang's relation given in Eq. 2-17. Furthermore, Terakawa *et al.* normalize their final equation to the initial and saturated values of solar cell efficiency, as given by Eq. 2-19 [46].

$$\frac{\eta(t) - \eta_{sat}}{\eta_{init} - \eta_{sat}} = -\left(\frac{1}{n}\right)\log\left[1 - \left(1 - \left(\frac{1}{10^n}\right)\right) * \exp\left(-\left(\frac{t}{\tau}\right)^{\beta}\right)\right] \qquad \text{Eq. 2-19}$$

Where η_{init} and η_{sat} are the initial and stabilized solar cell efficiencies, respectively. β is a dispersion factor that modulates the stretch of the exponential function, and τ is a time constant which indicates the total degradation time before efficiency stabilization. Meanwhile, n is a variable which is linked to the defect density characteristics of the material. Terakawa *et al.* provide the following definition of n, as seen in Eq. 2-19.

$$n = \log\left(\frac{N_s}{N_0}\right) \qquad \text{Eq. 2-20}$$

Where N_s and N_0 are the total density of potential defects in the device and the initial defect density, respectively.

In this project, the model proposed by Terakawa *et al.* will be fitted to the experimental efficiency data obtained. The results of these fittings will be analyzed according to the definition of the model parameters of n, τ, β, η_{init}, and η_{sat} as provided in this section. This exercise is carried out with precaution; the interpretations of the fitting parameters are made in light of their capability to approximate and approach empirical data. Meanwhile, it is important to stress that the fitting exercise must not be considered as a conclusive proof of the validity of n as a measure of defect density within the a-Si:H of the device.

Chapter 3: Experimental Setups and Conditions

In this chapter, the experimental methods employed throughout the thesis project will be explained in detail. The aim of this chapter is to emphasize how the experimental conditions have been controlled, and to what extent. Firstly, the operating principles of the machines used in the experiments will be described in detail. Secondly, the conditions under which these machines were operated are presented, as well as the experimental procedure followed in this project.

3.1 Experimental Setups

3.1.1 Deposition and Fabrication

Deposition of Thin Film Layers

In order to deposit the thin film semiconductor layers of the a-Si:H solar cell, radio frequency (rf) plasma enhanced chemical vapor deposition (PECVD) has become a research and industry standard, and has been utilized in this project. This deposition technique forms the desired layers by decomposition of a gas, the *precursor*, containing silicon and hydrogen, as well as prospective doping agents, in the desired proportions. A schematic figure of the rf-PECVD setup is shown in FIGURE 3-1 below. The deposition temperatures at which device grade a-Si:H is made is between 175 °C and 250 °C, allowing for low cost substrates such as glass or plastic [15]. The process scales easily for low-cost industrial application, and allows for tuning of material properties such as film stress and refractive index through choice of gas feed composition, temperature, pressure, and plasma power. The main drawback of the deposition technique is the relatively slow deposition rate, typically somewhere between $0.1\frac{\mathrm{nm}}{\mathrm{s}}$ and $0.5\frac{\mathrm{nm}}{\mathrm{s}}$ [22].

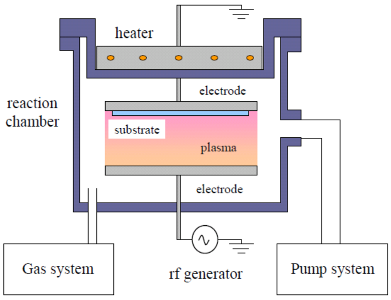

FIGURE 3-1: Schematic figure of the rf-PECVD setup. The figure is adapted from [22].

The *plasma,* a gas of ionized atoms, is used to provide the energy for the dissociation of the precursor gas, in this case SiH_4 with or without prospective dopants or extra hydrogen flow. The deposition itself takes place inside the chamber, where various pump systems assure vacuum pressure of a few mTorr in order to eradicate contaminant bodies. The precursor gases pass through the gas system into the reaction chamber. Therein, the plasma is ignited by an oscillating electric field through a radio frequency signal to the electrode plates. This frequency is the aforementioned radio frequency (rf) and the industry standard is 13.56 MHz. Frequencies at such elevated levels ensure capacitive discharges in the plasma which are reasonably time-independent. The presence of the oscillating electric field between the two electrode plates, one of which is connected to the rf source while the other remains grounded, causes the free electrons of the ignited plasma to oscillate. These electrons participate in inelastic collisions with neutral gases, causing further ionization and, thereby, more electrons. This sustains the plasma in the reaction chamber, and ensures decomposition of the neutral precursor gas molecules which continuously enter the chamber.

As a result of the ionization and decomposition of the precursor gas as described above, the plasma in the reaction chamber consists of neutral radicals and molecules, negative and positive ions, as well as electrons. The precursor gases therefore move towards the grounded electrode plate where the substrate is located by the process of diffusion. When depositing a-Si:H using silane gas, common radicals in the plasma are SiH_3, SiH_2, SiH, Si, and H, the most common of which is SiH_3. These gases will diffuse to the grounded electrode and bond weakly to the substrate surface. Once bound to the surface, radicals may combine with other loosely bound precursor radicals and escape the substrate. In this case, growth naturally does not occur. If a radical bonds with a DB in the substrate material, however, strong Si-Si bonds may form and the radical sticks, thereby contributing to the growth of the film. The probability that the radical will stick to the substrate is dictated according to the *sticking probability*, and is linked to the diffusion capability of the radical across the substrate surface. In the case of the radicals produced through the decomposition of silane, SiH_3 is the most favorable in this regard, and thereby is a more effective radical for annihilation of DBs in the substrate material than SiH_2, SiH, and Si [14]. Upon finalization of the deposition process, the subsurface reactions, such as hydrogen release from the material matrix, take place.

Deposition of Metal Contacts

Metal contacts are deposited through Beam Physical Vapor Deposition (PVD). PVD is a vacuum deposition process by which a solid source is evaporated, with subsequent transfer towards, and condensation on, the deposition substrate. There exist several variants of the PVD process, the main differences being how the source is evaporated. In this project Electron Beam PVD is employed. During Electron Beam PVD, a target anode is bombarded with an electron beam given off by a charged tungsten filament under high vacuum. The source or evaporation material can be in the form of an ingot or rod.

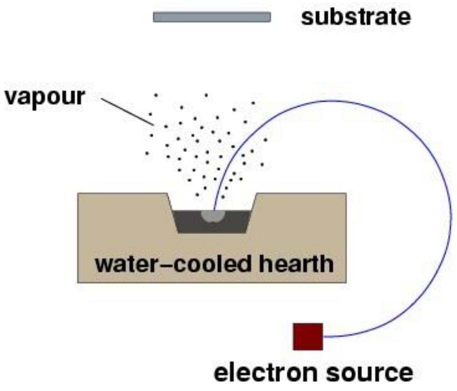

FIGURE 3-2: Schematic figure of the electron beam PVD functioning. The figure is adapted from [47].

The generated electron beam is accelerated to high kinetic energy through an electric potential difference, and directed towards the evaporation material by a magnetic field within the deposition chamber as seen in FIGURE 3-2 above. Upon striking the evaporation material, the kinetic energy of the accelerated electrons is transferred to the source, resulting in melting or sublimation. When sufficient energy is transferred to the source, evaporation will occur, and the source vapor will diffuse to deposit on the chamber walls, and the substrate.

Reactive Ion Etching

The etching of the solar cells, and the final process in the sample manufacturing process, is carried out via Reactive Ion Etching (RIE). RIE is also a plasma-based process. However, as opposed to rf-PECVD, the role of the plasma in RIE is to remove deposited layers. The chamber, pumped to vacuum, is filled with etching gases according to the type of material to be etched and the desired etching rates. The sample is placed on a substrate, which also functions as one of the two electrodes used to generate the necessary electric field to create the plasma. As is the case in PECVD, a radio frequency is applied to the electrodes, thereby imposing oscillations in the electric field, which in turn generates the plasma. Electrons and plasma ions are accelerated towards and away from the sample through the cycles of the electric field, as demonstrated in FIGURE 3-3 below. Some of the sample material may be etched away by sputtering due to transfer of kinetic energy, but the main etching process consists of ions reacting with the sample material, thus etching it away. The top electrode is electrically grounded and works as an electron sink.

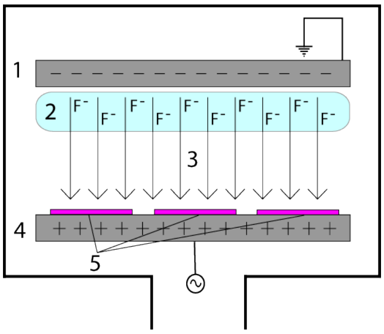

FIGURE 3-3: Schematic figure of the functioning of a reactive ion etching system. The figure is adapted from. [48]

3.1.2 Characterization Measurements

External Quantum Efficiency

The general purpose of the External Quantum Efficiency (EQE) setup is to focus light on a solar cell, and then calculate the fraction of this incoming light which is converted into electricity. To this end, a light source is needed, and a current measurement setup of a solar cell. The light source in use is a Xenon arc lamp and is connected to the main grid. For the sake of fully depicting the spectral response of the solar cell, the light source is fitted with a *monochromator*, which will produce the desired wavelengths throughout the measurement. The monochromator also holds filters to filter out the higher orders of diffraction from the gratings.

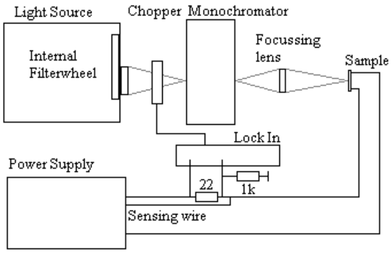

FIGURE 3-4: Schematic figure of the external quantum efficiency setup of the PVMD group at TU Delft [49].

The potential over the solar cell is controlled by a floating power supply, as to compensate for fluctuations. There are sources of current offsets, and therefore the offset current needs to be measured. The light source is therefore chopped, thereby making it possible to distinguish between offset and actual solar cell current generation. The current is measured through a voltage measurement over a resistor. FIGURE 3-4 shows a schematic demonstration of the EQE setup.

Illuminated IV-Characteristics

The performance of the solar cell under illumination is, as discussed in previous chapters, revealed by the relationship between generated voltage and current. The principle of this measurement is simple – vary the voltage applied across a solar cell and measure the outgoing current via the proper circuit connections. However, the difficulty in accurately characterizing the solar cell performance lies in the number of external parameters which must be well defined and controlled. Practical concerns relevant to the IV-measurement under illumination are the stability of generated illumination, the uniformity of the light on the test plane, the spectral distribution of the irradiance generated, the temperature of the measured sample, and the contacting between the measured sample and measurement circuit.

The PASAN Slab measurement setup is an automated test bench where such measurement effects are taken into account. The xenon single flash tube yields a quick flash of light which has a spectral distribution very similar to that of AM0. Heating effects are consequently negligible and therefore no filtering is needed in the infrared part of the spectrum. Simple filtering is all that is needed to obtain AM1.5 or other AM-variants of the spectrum. A fully uniform light emission area is used to obtain light uniformity, and active control of the irradiance corrects each measured point immediately to the correct level. At the will of the user, the software of the machinery will begin automatic acquisition for 100 measurement points. A voltage is set, and measurements of instantaneous voltage, current, and irradiance are made. A four point contact probe is in place in order to correct for losses in voltage due to contact resistance. The software subsequently reads the measurement files and searches for the short circuit current and open circuit voltage points. The solar cell characteristics which are stored are corrected to Standard Test Conditions.

Dark IV-Characteristics

Voltage-current measurements in the dark are, as is the case for when measuring under illumination, sensitive to external parameters. While the measurement principle itself remains simple, controlling these external parameters is more complex. The most pertinent external parameters are light contamination and electrical losses due to contact resistance. The Keithley multimeter connected to the measurement circuit is sensible to currents in the range of 10^{-12} A, meaning that slight deviations can have large effects. In order to reduce the effects of light contamination, an impermeable seal covers the measurement bench throughout the acquisition. The lights in the measurement room are turned off, and there are no windows so as to ensure that no light enters. The contact surface area is reduced to a minimum by employing needle probes which function as electrodes and circuit connections to the solar cell. Temperature is also an important external parameter to control throughout this measurement. This is done by coupling the substrate holder to a thermogenerator, which allows for programmable temperature settings and stabilization times between changes in temperature.

3.1.3 Degradation

In order to degrade the a-Si:H solar cells, a computer controlled degradation-setup of customary hardware configuration design of the TU Delft is used. The degradation setup consists of a solar cell platform where the samples to be degraded are placed. This platform is attached to a cooling system comprised of three Peltier-elements, which offer thermoelectric control of the platform, as well as a fan. On top of the platform, four conjoined perpendicular mirrors form the walls of the enclosure where the samples will be placed. An aluminum block holding a panel of LEDs, a fan, and a heat sink is placed at the very top, and seals of the enclosure. A picture of the setup is shown below, in FIGURE 3-5.

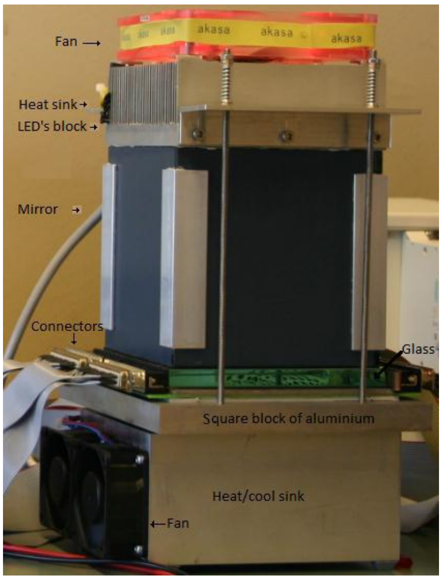

FIGURE 3-5: The solar cell degrader of the PVMD group at TU Delft. The figure is adapted from [50].

The platform is also fitted with a photodiode, which is capable of continuously monitoring the irradiation levels within the enclosure. Three solar cell strips holding 30 solar cells each may be degraded and measured simultaneously. Three connector cables feed the signals of each of these sample strips to the computer, which offers full control of the degradation setup. Via a National Instruments switch, and a Keithley voltage source, it is possible to measure the performance of any single cell of any desired solar cell strip at any given time. The degradation software is fed with a schedule for when to perform current-voltage characteristic measurements throughout the degradation process.

The degradation software also controls the temperature within the enclosure and the irradiance levels, which are both continuously monitored and adjusted via feedback-loops consisting of Watlow computer elements. A 2 cm thick glass sheet is placed on top of the samples so as to obtain a stable and homogeneous temperature distribution in the solar cells. The mirrored walls are also in place for the sake of illumination homogeneity – thereby ensuring a stable and constant light intensity distribution within the enclosure. Moreover, the glass slab exerts a force on the samples which ensures better electrical contact with the external circuit.

The great advantage of the degradation setup is the fact that in-situ measurements of solar cell current-voltage characteristics may be carried out throughout degradation. Thereby, the degradation setup offers a measurement environment where only real effects of light induced degradation are registered. The constant feedback-based control of irradiation levels and temperature also ensures a degradation environment which is well defined, and reliable. The LED lights offer a steady and durable generation of light, with a lifetime of tens or hundreds of thousands of hours. Data collection is handled by the custom LabView program, tailored to the level of control which is desired for this measuring process. All solar cell external parameters are written to file on the server of the university, ensuring a minimum data loss in case of local power shortages or other unforeseen disturbances. The procedure for launching the degradation of solar cells may be summarized as follows:

1. Mount the samples on the platform and place glass, mirrored walls, and LED-panel on top. Fix with screws.
2. Turn on power sources for heat, irradiance, and voltage source.
3. After launching the degradation measurement software
    a. Indicate the names of the samples
    b. Indicate which cells are to be measured
    c. Indicate the desired temperature during degradation
    d. Indicate the desired irradiance level during degradation
    e. Indicate the time steps for measurements during degradation, as well as resolution of the IV-characteristic curve.
    f. Begin measurement

A figure of the complete degradation setup is shown below, in FIGURE 3-6.

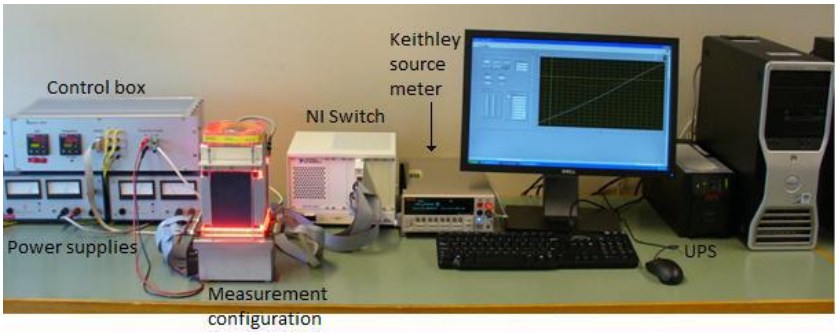

FIGURE 3-6: The complete in-situ solar cell degradation and measurement setup of the PVMD group of the TU Delft. The figure is adapted from [50].

3.1.4 Annealing

Thermal annealing of the solar cells is carried out in a thermal oven with mechanical convection for standard laboratory applications. The general protocol fan convection method offers a high-precision work space temperature control, adjustable in steps of one degree up to 250°C. A fixed-speed fan ensures temperature uniformity within the oven. The oven is fitted with a countdown timer for timed process control.

3.2 Experimental Details and Conditions

3.2.1 Deposition Details and Conditions

The solar cell samples are deposited in the AMOR multi-chamber rf PECVD system constructed by Elettrovara (Torino, Italy). This cluster tool permits the deposition of intrinsic, p-doped, and n-doped thin film amorphous and microcrystalline silicon, as well as silicon alloys like silicon germanium. The system comprises four chambers, and a load lock, all connected to a common transport chamber. The recipes and deposition controls are all through a PC interface. As two different hydrogen dilution ratios were used for i-layer deposition, the details of each respective deposition are given below. For a study of the thickness effects of the intrinsic layer (i-layer) on performance and degradation characteristics, three samples of varying i-layer thickness were produced for each sample set. The structures of the solar cells are described below.

R_0-Material

In total, six sample strips, two of each desired intrinsic layer thickness, were deposited. The solar cell deposition structure is as follows:

1. p-a-SiC:H – 10 nm layer thickness
2. a-SiC:H – 5 nm layer thickness
3. i-a-Si:H – variable layer thickness: 300 nm, 600 nm, and 900 nm
4. n-a-Si:H – 20 nm layer thickness

R_{20}-Material

In total, nine sample strips, three of each desired intrinsic layer thickness, were deposited. The solar cell deposition structure is as follows:

1. p-a-SiC:H – 10 nm layer thickness
2. i-a-Si:H – variable layer thickness: 300 nm, 600 nm, and 900 nm
3. n-a-Si:H – 20 nm layer thickness

In both cases, the solar cell structure is deposited on a glass superstrate coated with an ASAHI-VU transparent conductive oxide layer. The substrate temperature at the time of deposition was 180 degrees Celsius. TABLE 3-1 and TABLE 3-2, as seen below, contain the flow-rates of feed gases, as well as plasma power for R_0-type solar cells and R_{20}-type solar cells, respectively.

	p-a-SiC:H	a-SiC:H	i-a-Si:H	n-a-Si:H
SiH_4 [sccm]	20	1.6	40	40
CH_4 [sccm]	45	3,7	0	0
B_2H_6 [sccm]	2	0	0	0
PH_3 [sccm]	0	0	0	11
H_2 [sccm]	0	200	0	0
$P_{RF\text{-}PLASMA}$ [W]	2.5	4.8	1.9	1.9
$P_{DEPOSITION}$[mbar]	0.7	2.6	0.7	0.6

TABLE 3-1: Deposition Details of R_0-type material

	p-a-SiC:H	i-a-Si:H	n-a-Si:H
SiH_4 [sccm]	20	5	40
CH_4 [sccm]	45	0	0
B_2H_6 [sccm]	2	0	0
PH_3 [sccm]	0	0	11
H_2 [sccm]	0	100	0
$P_{RF\text{-}PLASMA}$ [W]	2.5	2.5	1.9
$P_{DEPOSITION}$[mbar]	0.7	2.0	0.6

TABLE 3-2: Deposition Details of R_{20}-type material

After deposition of the semiconductor layers, metal contacts are deposited on the samples – alloys of aluminum, chromium and silver. Each sample strip holds 30 solar cells, each of which is coated with a metal contact with a surface area of 0.16 cm^2. The metal contacts are deposited by physical vapor deposition in the PROVAC machine, a single-chamber system with a 4 pocket electron gun for physical evaporation of aluminum and chromium. Silver is thermally evaporated. The metal contact depositions are made at room temperature under vacuum.

Lateral currents in the upper active layers (i.e. closest to the metal back contact) of the solar cells have been shown to cause a larger effective solar cell area than intended. This effect is inhibited by etching away the parts of the active layer surrounding the metal contact [43]. Upon completed deposition, the samples are, for this reason, placed in the RIE Machine of the PVMD group's facilities – namely the ALCATEL. The etching is set to remove ca. 40 nm (i.e. two times the thickness of the n-layer) from the active layers of the solar cells, beginning the process in the n-layer. The plasma environment during the etching is well-defined and controlled. The ALCATEL is set to etch at a temperature of 50°C, a pressure of 0.05 mbar, an rf-power density of 0.5 W/m^2, and using CF_4, SF_6, and O_2 as process gases.

3.2.2 Characterization Details and Conditions

The characterization measurements, i.e. EQE, illuminated IV, and dark IV measurements, are made continuously throughout the course of the project in order to monitor the effects of light soaking. However, because dark IV measurements are temperature dependent experiments, these are limited to a minimum: one measurement of each sample *as-deposited* (AD), and one measurement after degradation and annealing. As applying a thermal load to a solar cell will anneal the device and its defects, it is desirable only to perform such experiments at stages where the device is as insensitive as possible to elevated temperature exposure. It is assumed that a solar cell is at this stage in its AD state, and after an appropriate number of post-degradation annealing hours. Therefore, the dark IV of the R_0 devices was measured after 10 and 20 hours of annealing, whereas the dark IV of the R_{20} devices was measured after 1 hour of thermal annealing. The dark current of the device is measured for bias voltages ranging between 1 and -2 Volts, in increments of 0.05 Volt. The voltage sweep goes from a positive to a negative bias. The temperature range over which each voltage sweep was made is from 100°C to 30°C, in steps of 10 degrees. Temperature stabilization after each temperature change is ensured via computer control.

EQE and illuminated IV experiments do not impose any additional thermal load to the device, and are therefore carried out more regularly. EQE and illuminated IV records are kept for each sample for its

AD state, its *degraded* state, as well as after each anneal. The EQE is measured for wavelengths between 280 and 850 nanometers, in increments of 10 nanometers. In the illuminated IV measurements, a voltage sweep between 1 Volt and -0.1 Volt is made, where 100 different points along the sweep are recorded.

3.2.3 Degradation Details and Conditions

One round of degradation was carried out for each *thickness series*, comprising three samples of equal R-type material and varying i-layer thickness (i.e. 300 nm, 600 nm, and 900 nm). The degradation *and* the in-situ IV-measurement were performed under red light provided by LEDs bulbs, of which the light spectrum is found below in FIGURE 3-7. As the reader will note, the spectrum of the LEDs is tightly distributed around a wavelength of 630 nm. Because this investigation entails a study of the temperature dependency of light induced degradation, the degradation process was carried out at 25°C and 45°C for both R-type materials. One distinct thickness series was degraded at each temperature. In the case of R_{20}-type material, an additional degradation was carried out at a temperature of 60°C for the third distinct thickness series.

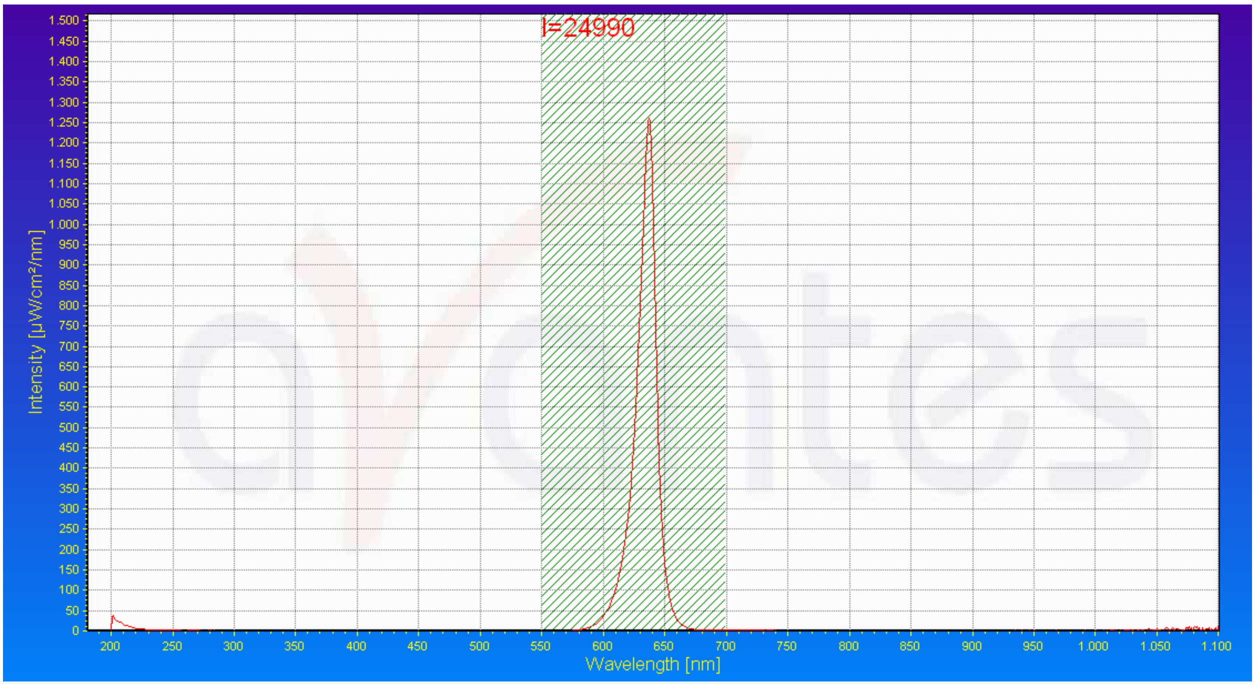

FIGURE 3-7: The spectrum of LEDs employed in the in-situ solar cell degradation setup of the PVMD group of TU Delft. The figure is adapted from.

The light intensity of the LEDs was set to 350 W/m^2, and is kept constant throughout all degradation processes. This is an arbitrary intensity setting, and is based on the performance of the 600 nm intrinsic layer sample of the first R_0-type thickness series to be degraded. The choice of intensity was such that the short-circuit current of this particular sample at 25 degrees Celsius is the same as under STC under irradiation of AM1.5 spectrum. Each thickness series is degraded until visible signs of stabilization in the external parameters of the degraded samples. The cells were degraded under open circuit conditions.

3.2.4 Annealing Details and Conditions

The thermal annealing of the samples is performed for each thickness series at several points along the experimental process. Firstly, the AD samples are annealed for 30 minutes, as this has shown to yield a higher and more stable initial solar cell performance. After degradation, the samples are thermally annealed in steps of increasing periods of time, in order to monitor their progress. Therefore, thermal annealing after degradation is set to the following time schedule: 1 hour/1.5 hours/2.5 hours/5 hours/10 hours. Only the R_0 samples are annealed for the final 10 hours. The temperature throughout the thermal anneal is set to 130℃.

3.2.5 Experimental Proceedings

In this section, the aim is to structure the steps of the experimental procedure which were listed previously in this chapter. After deposition, the thickness series is thermally annealed at 130℃ for 30 minutes. Thereafter, the samples are characterized through EQE measurements, as well as dark and illuminated IV measurements. At this point, degradation is commenced at a given temperature. Voltage-current measurements under the 630 nm-light of the LEDs are made throughout the degradation, until it is finally stopped upon the stabilization of external parameters. Subsequently, the samples are characterized through EQE measurements and illuminated IV measurements only. Afterward, the samples are again thermally annealed at 130℃ in steps of varying time, as noted in the previous sub-section. EQE and illuminated IV measurements are carried out after each anneal. One dark IV measurement is carried out when the samples are considered to be sufficiently insensitive to thermal loads – after 10 hours of annealing in the case of R_0 cells, and after 1 hour in the case of R_{20} cells. The annealing steps are continued after the dark IV measurements are completed.

Chapter 4: As-Deposited Characteristics of a-Si:H Solar Cells

This chapter is devoted to illustrating the initial conditions of the solar cells, and how these vary according to the test conditions of the project. The initial state of the solar cells is an important benchmark for device performance analysis, as it sets the framework for comparison. Moreover, the initial characteristics of the solar cells under consideration can indicate the state of the material of which they consist. As a study of the SWE is inevitably dependent on material characteristics, it is important to record such baseline values. Controlled variations in the initial conditions of the devices considered may also yield valuable information on the properties of a-Si:H, as well as a-Si:H solar cells. Therefore, the effect of absorber layer thickness on the initial conditions is discussed in this chapter. Furthermore, the effect of hydrogen dilution in the absorber layer on the initial performance of the solar cells is presented here. We note for the sake of clarity that the R_0-type material measured under STC is henceforth consistently presented as the point of reference to which all variations, either in material configuration or in measurement conditions, will be compared.

4.1 Effect of Thickness on Initial Performance

The amorphous material is, in its initial as well as its degraded state, a material with a relatively high defect density . As noted in earlier chapters, the presence of such defects in the material ultimately degrades its electronic properties because they act as traps and recombination centers for charge carriers. Inevitably, the amount of defects in the device scales with the amount of the defect-containing substance needed to construct it. Therefore, the thickness of the a-Si:H material will affect the solar cell performance. The thickness dependency of a-Si:H solar cell performance is therefore delineated in this sub-chapter.

4.1.1 External Parameters

As explained in Chapter 2 of this report, the external parameters of the solar cell device are derived from its characteristic current voltage relationship. In Figure 4.1 below, the initial external parameters of an R_0-type thickness series are plotted as a function of thickness.

The plots shown in FIGURE 4-1 are based on averages of a representative amount of solar cells for each absorber layer thickness. A 10-cell average is shown for samples with 300 nm and 600 nm absorber layer thickness, while a 7-layer average is plotted in the case of the thickest sample. The error bars in the plots correspond to three standard deviations within the group of cells for which the averages are considered.

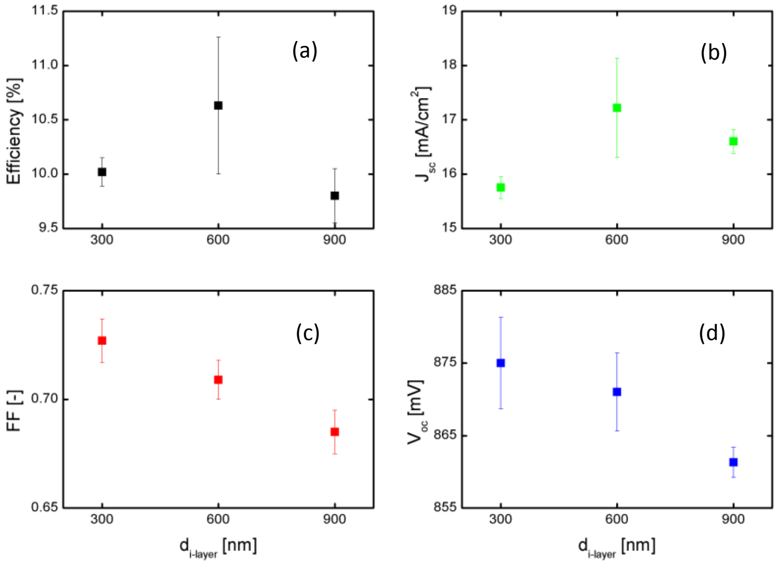

FIGURE 4-1: Thickness dependency of (a) efficiency, (b) short circuit current density, (c) fill factor, and (d) open circuit voltage for as-deposited R_0-type material.

It is immediately possible to note the elevated efficiencies in all cells at this initial stage of the investigation. It is important to underline that the cells deposited and studied are state of the art, and are therefore well disposed to comparison with devices used in industry and other research institutes. The open circuit voltage and the fill factor show a clear decrease with increasing absorber layer thickness. The open circuit voltage is directly proportional to the electric field within the device. As the distance between the doped layers increase, this electric field will gradually diminish, which explains the V_{oc} drop as seen in the figure above. As the thickness of the solar cell increases, so does the electric impedance imposed on charge carriers moving inside it. Naturally, providing more of the material will increase the equivalent series resistance it poses to the charge carriers. Moreover, being an intrinsically defective material, a decrease in equivalent shunt resistance with increasing absorber layer thickness in the device will occur. These two trends are manifested in the fill factor results seen above.

Meanwhile, the J_{SC} results show a trend which indicates an equilibration between two opposing processes. As the absorber layer thickness increases, more sunlight is naturally absorbed, thus producing more current. However, the defects within this very same layer may act as recombination centers, which will tend to diminish the current as the intrinsic layer thickness increases. As FIGURE 4-1 indicates, the most favorable equilibrium between these two processes occurs when the intrinsic layer thickness is 600 nm. Interestingly, this is also the case for the solar cell efficiency. A similar depth dependency for initial V_{OC} and fill factor is observed. Moreover, a similar depth dependency is also seen for initial J_{SC} and conversion efficiency.

4.1.2 EQE

The EQE of the solar cell, as noted earlier, gives a combined picture of the device's optical response and electric losses. As such, the external quantum efficiency analysis portrays both how light is absorbed in a material, and how the charge carriers behave and move within the device once they are generated. By changing the thickness of the device, it is possible to probe these two phenomena separately to a limited extent. In FIGURE 4-2, seen below, the initial EQE under short circuit conditions with a 0 V bias voltage of a thickness series of R_0-type solar cells are plotted as a function of wavelength. Clear trends in the data indicate an increase in EQE for longer light wavelengths ($\lambda > 550nm$), and a drop in EQE for the shorter wavelength ($\lambda < 550nm$). These trends have been previously documented in various publications [14] [51] [52].

As the short circuit current is the spectrally integrated product of quantum efficiency and incoming photon flux, the J_{SC} and EQE are, by definition, inextricably linked. We note that the similar trends in thickness dependence of these two physical quantities. Meanwhile, as the absorption efficiency of sunlight in the amorphous material is wavelength dependent, light is not absorbed homogeneously in the solar cell device. Thereby, charge carrier generation will also vary in a device according to depth. Due to a higher absorption rate of light with decreasing wavelength, the UV region of the solar spectrum is quickly absorbed in the solar cell. Meanwhile, the longer wavelength regions in the IR part of the spectrum are less efficiently absorbed by the amorphous material and may therefore penetrate deeper into the solar cell before complete extinction. This leads to a more homogenous distribution of IR light absorption in the amorphous material, and in the solar cell. This fact also explains why EQE in the long wavelength regions increases with increasing absorber layer thickness, as more absorber material increases the optical path length of the light in this spectral region.

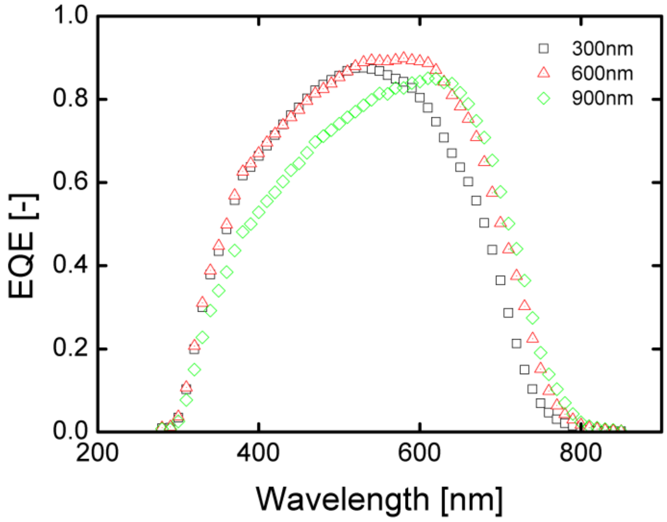

FIGURE 4-2: Thickness dependency of EQE for as-deposited R_0-type material.

Upon charge carrier generation, the photovoltaic effect in a material consists of separating and collecting the charge carriers of opposite polarity. Because of the inhomogeneous absorption of sunlight in the material, the EQE yields information regarding how effectively charge carriers within the device are collected. In p-i-n structured solar cells, such as the ones studied here, the light in the UV range is considered to be absorbed in the proximity of the interface between the p-doped layer and the intrinsic layer, denoted the *p-i interface* [52]. This implies that the drop in EQE in the spectral range of 250 nm to 500 nm, as intrinsic layer thickness increases from 600 nm to 900 nm, is most likely due to collection losses of charge carriers generated near the p-i interface. As the distance to traverse before collection from this point is far greater for the electrons than for the holes, the figure above may indicate that for thicker devices, EQE is limited by electron collection losses. This indication is reinforced by the observation that EQE in the long wavelength regions increases as the generation of carriers deeper in the i-layer, i.e. closer to the i-n interface, is fairly independent of intrinsic layer thickness for red illumination. However, for longer wavelengths, more carriers are generated deeper in the intrinsic layer, relatively speaking, when illuminating with red light as opposed to blue light. Therefore, there is a relatively larger amount of holes generated at depths where they must traverse a significant part of the intrinsic layer before being collected. The increasing EQE for these wavelengths may therefore imply that hole-propagation is not the limiting factor in the charge carrier collection, even within thicker devices.

4.1.3 Dark IV

As the dark current voltage characteristics are merely a measure of recombination in the a-Si:H solar cells, it is a useful means of characterizing the devices when investigating the SWE. As recombination in the a-Si:H device is linked to the defect density, dark IV measurements are used as a tool to qualitatively investigate material defects. As discussed in Chapter 2, the dark current of a device is temperature dependent. Providing thermal energy to the material yields a higher density of excited electrons which are prone to recombine through defects, and thus generate a recombination current. FIGURE 4-3 below depicts a dark IV measurement for two different temperatures. A visible increase in dark current, or recombination current, by several orders of magnitude is observed for a temperature difference of 50°C. Meanwhile, the thickness dependence of the dark current characteristic curve, or the lack thereof, is significant. As noted in previous studies, recombination in the dark seems to be rather independent of the thickness of the material under consideration [41] [42].

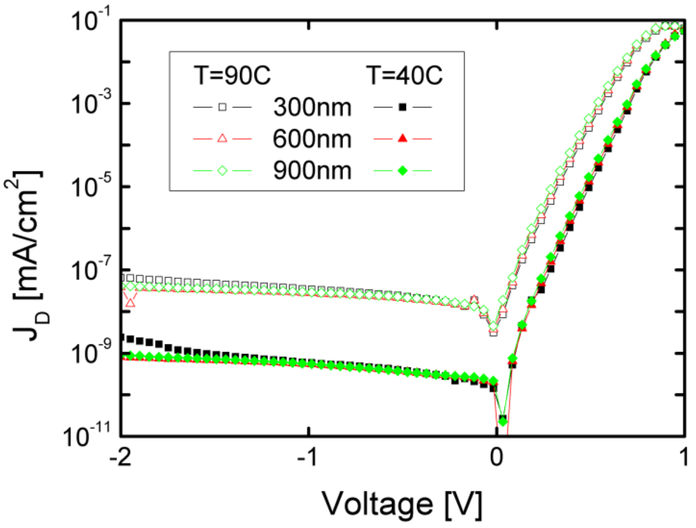

FIGURE 4-3: Thickness dependence of dark IV characteristics for as-deposited R_0-type material.

Previous studies have come to the conclusion that the thickness independence of recombination implies a non-uniform distribution of defects within the amorphous material [41]. This is most notably the case within the bias voltage range which is characteristic for SRH recombination, namely 0.2 V to 0.7 V. It is consequently argued that the recombination must be focused in one spatial region of the intrinsic layer, which is distinct from the bulk environment of the solar cell. This region is considered to be the p-i interface [41]. This interpretation implies that a relatively small zone near the interface between the p-doped material and the intrinsic material constitutes a sufficiently large proportion of the recombination in the device, that it masks the remaining recombination effects in the bulk. Therefore, the dark IV measurement is seen by many researchers as a probe of the p-i interface of the a-Si:H solar cell.

Ideality Factor

The ideality factor, as defined in Eq. 2-9, offers a closer look at the voltage dependency of the recombination current. Physically, the ideality factor represents the change in number of traps in the material which contribute to the recombination current due to a change in bias voltage, i.e. distance between quasi-Fermi levels [39]. Previous studies have found the ideality factor to be independent of thickness for the voltage range where SRH recombination is dominant, which reflects the results of the observed dark IV measurements.

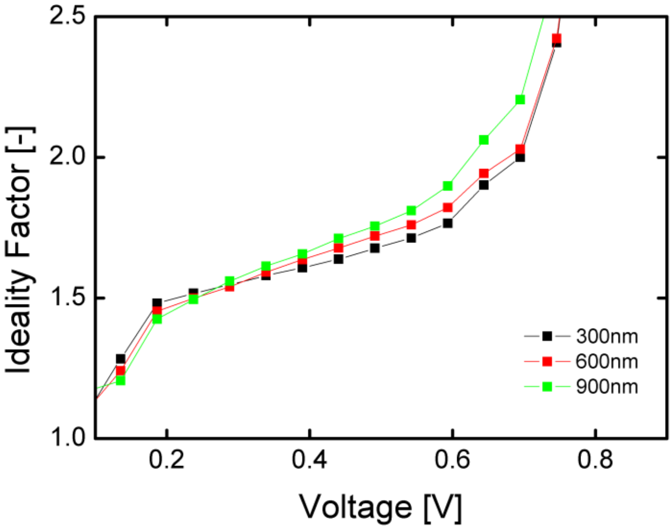

FIGURE 4-4: Thickness dependencies of ideality factor of R_0-type material.

Thus, FIGURE 4-4 above is in line with previous reports of a fairly thickness independent ideality factor. This can be interpreted in terms of space charge regions within the device, which are found at the layer boundaries. The space charge regions cause band bending in the interface region, which, in the case of the p-i interface enhances the electric field effects in its direct vicinity. Thereby, a larger defect density and electric field in the p-i interface implies that the recombination current is dominated by recombination in this region. The energy distribution of states in the mobility gap at the p-i interface is also distinct from elsewhere in the device. Thereby, it is believed that the thickness independence of the ideality factor as seen in FIGURE 4-4 above illustrates the dominance of recombination in near the p-i interface, as opposed to deep within the bulk of the absorber layer [14] [41].

Thermal Activation Energy of Recombination

The thermal activation energy of recombination, or dark current, within the device is consequently calculated according to Eq. 2-10 from dark current measurements. Plotted in FIGURE 4-5 below, the voltage dependent activation energy shows thickness independence for the given voltage range.

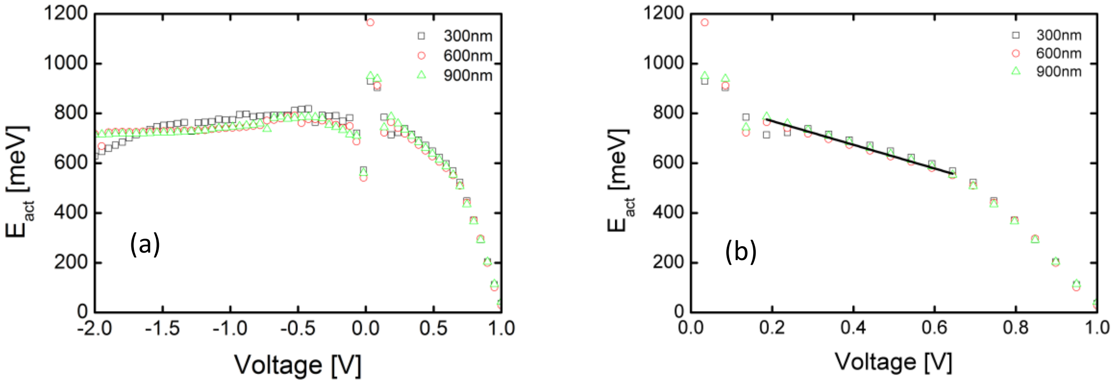

FIGURE 4-5: Activation energy plots for an as-deposited R_0-type material thickness series for (a) reverse and forward bias voltage and (b) forward bias voltage with linear fit of data points.

The activation energy as seen in the figure above is plotted for the full voltage range, i.e. forward *and* reverse voltage bias, and solely for forward bias voltages. For the reverse bias voltages, the activation energy is more or less constant and equal to about half the band gap of the absorber layer. This is consistent with theory, as the increased electric field effects imposed by a reverse bias reduces active recombination centers, and therefore restores the thermal activation energy to the energetic distance between the Fermi level and the conduction band level [22].

In forward bias, the linear region of the thermal activation energy decrease with respect to applied voltage is indicated by the solid black line. This is also a linear fit of the data points in this region from all three thicknesses, and yields a mobility band gap of $\mathrm{E_{mob}} = 1.63\ \mathrm{eV}$ and a thermal ideality factor of $\mathrm{m_{th}} = 2.1$, based on the relation seen in Eq. 2-11. Furthermore, the thermal ideality factor is in line with the theoretical value of 2 [42]. Similar values for the R_0-type solar cell mobility gap have previously been presented by Kind *et al*. [14].

4.2 Effect of Hydrogen Dilution on Initial Performance

Amorphous material deposited with H-dilution ratio, also known as protocrystalline silicon, has been shown to resist LID to a larger extent than undiluted a-Si:H [34]. Essentially, use of hydrogen dilution during deposition yields a new type of material structure. As noted in Chapter 2 of this report, the protocrystalline material structure is considered amorphous with reduced defect density. In this project, a hydrogen dilution of R=20 was used during deposition of thickness series to which the R_0 material could be compared. By choosing R=20, it was ensured that crystalline growth would not occur, even for elevated thicknesses [35]. As a result, the R_{20} material is still completely amorphous, although its structural properties are sufficiently different from R_0 a-Si:H. This is reflected in the solar cell performance, which we will compare in this section. It has been shown that the initial performance of R_0-type and R_{20}-type a-Si:H consistently differ [35]. In the following sections, the initial differences between one R_0 thickness series and one R_{20} thickness series are presented and discussed.

4.2.1 External Parameters

The external parameters of R_0 and R_{20} material are shown in FIGURE 4-6 as a function of absorber layer thickness. As the plots aptly illustrate, the initial performance of the R_{20} devices are consistently lower than that of the R_0 device. Moreover, these differences are significant – efficiencies of R_{20} showing a 40%-50% reduction with respect to the R_0 samples. This decrease in initial performance is consistent with previous findings [35]. The decrease in fill factor in the R_{20} samples are attributed to a partial deterioration of the p-i interface, due to the high incoming flux of hydrogen atoms upon the p-layer during absorber layer deposition. The same reasoning is used to explain the drop in V_{OC} when the R-value is increased. The decrease in V_{OC} occurs despite the fact that the bandgap of the R_{20} material is higher than that of R_0 material. Meanwhile, the increased bandgap is manifested in the J_{SC} decrease which is observed for higher R-values. It is important to underline, however, that the cell structure of the R_{20} samples does not comprise a buffer layer between the p-layer and the absorber layer. Therefore, a part of the V_{OC} and efficiency difference between the two material types may be attributed to this circumstance [14]. However, it is henceforth assumed that this difference is negligible with respect to the effect of increased hydrogen dilution in the absorber layer.

Apart from the efficiency, the initial performance of the two material types shows the thickness dependencies which are visibly different. Whereas the V_{OC} of the R_0 samples diminish with increasing absorber layer thickness, the V_{OC} of R_{20} cells remains more or less constant. This is a peculiar trait, as the electric field generated across the device should diminish as the device thickness increases. On the other hand, the J_{SC} of the R_{20} material shows a steady increase with absorber layer thickness. The drop in J_{SC} between 600 nm absorber layer thickness and 900 nm absorber layer thickness for the R_0 material was attributed to a high density of defects.

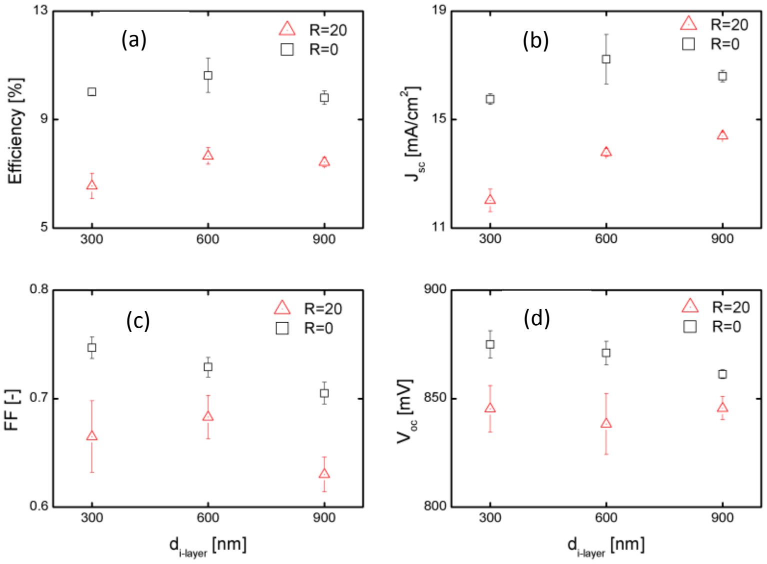

FIGURE 4-6: Initial (a) efficiency, (b) short circuit current, (c) fill factor, and (d) open circuit voltage compared for two different hydrogen dilution ratios.

The R_{20} material has a lower native defect density than the R_0 material, which would result in less recombination in the material. Therefore, a possible explanation for the observed J_{SC} trend is that the equilibrium between increase in absorbed sunlight (i.e. generated charge carriers) and recombination is shifted. Consequently, the thicker devices can still be favorable with respect to J_{SC}. Meanwhile, another reason for this pattern may also be the increased bandgap in the R_{20} material, which results in a clear reduction in absorption, and therefore generation of charge carriers, within the material. As the density of charge carriers and recombination are inevitably linked, it is difficult to say with certainty whether lower generation permits for continued increase in J_{SC} in very thick devices. The R_{20} fill factor dependence on intrinsic layer thickness, on the other hand, could suggest that this is not the case. The initial increase in fill factor when passing from 300 nm to 600 nm intrinsic layer thickness implies that the losses due to series and shunt resistance in the R_{20} material are less significant than they are in R_0 material. The subsequent decrease in J_{SC} for a 900 nm sample indicates that the dominant resistance loss is due to series resistance. Assuming a generally better, i.e. higher, shunt resistance in the R_{20} than in the R_0 solar cells is consistent with a lower defect density in the hydrogen diluted material.

4.2.2 EQE

The spectral response of the R_{20} solar cells is characterized by its elevated energetic bandgap. As the J_{SC} results imply, a lower EQE is to be expected for the hydrogen diluted samples vis-à-vis the undiluted samples. FIGURE 4-7 presents the external quantum efficiency of R_{20} and R_0 samples for the thinnest and the thickest cells, i.e. 300 nm intrinsic layer and 900 nm intrinsic layer.

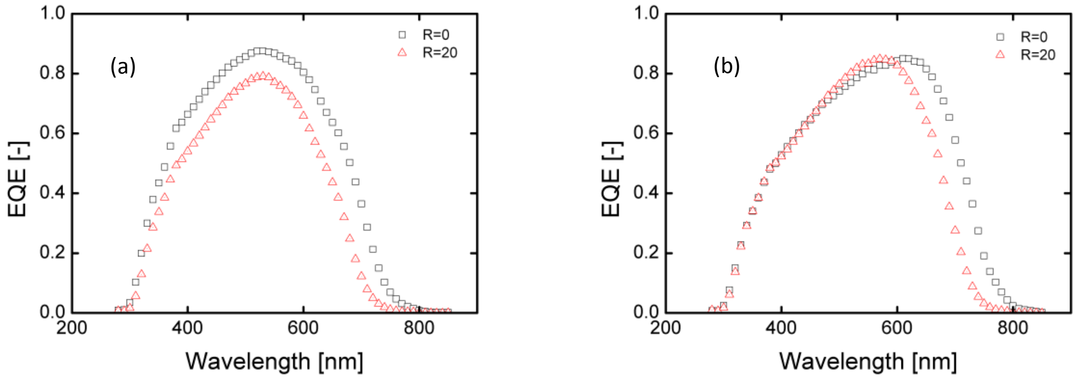

FIGURE 4-7: EQE for two different hydrogen dilution ratios of (a) 300 nm i-layer sample and (b) 900 nm i-layer sample

FIGURE 4-7 indicates a significant decrease in EQE for both thickness samples. Meanwhile, it is not expected that the 300 nm R_{20} sample's response in the blue part of the spectrum differ so greatly from that of the R_0 sample. The absorption spectrum of the diluted and undiluted samples has been shown to be more or less equal in this spectral range. As seen in FIGURE 2-4, only for wavelengths larger than 600 nm to 650 nm does the absorption coefficient of the R_{20} a-Si:H decrease notably compared to the R_0 a-Si:H material. This is well depicted in the case of the samples with intrinsic layer of 900 nm, where the EQE is almost identical up to a wavelength of 600 nm.

The most probable explanation for the poor EQE in the blue region for is related to the deposition process of the R_{20} solar cells. Prior to the deposition of the R_{20} samples, a maintenance period was in session for the AMOR PECVD machine. Consequent depositions showed similar trends in spectral response in the shorter wavelength range, and it is therefore likely that the chambers of the deposition system had not been conditioned sufficiently after the maintenance works. The problem was solved when depositing the p-layer of a p-i-n structure using higher rf-power. Consequently, it is believed that the rf-power which was set during deposition of the R_{20} samples used this project was too low. In practice, this will lead to less methane molecules being dissociated during deposition of p-SiC:H. Essentially, the carbon content in the p-Si:H assures a higher order in the material, and, consequently, a larger bandgap. If the dissociation of methane is less than intended, the p-layer will end up with a lower bandgap, and absorption in the p-layer is expected. This would result in the type of EQE differences that is have obtained here, particularly because the blue light is quickly absorbed in the device, and the p-layer is one of the first layers the light passes through in the solar cell upon illumination. The results of this project for the R_{20} samples must therefore be considered in light of the possibility that the bandgap of the p-layer is smaller than intended for a standard p-i-n structure.

4.2.3 Dark IV

As the material structure of the R_{20} material exhibits fewer defects, it is expected that the level of recombination within the device to be inferior to that of an R_0 solar cell. In FIGURE 4-8, the recombination current for the R_0 and R_{20} solar cells are compared for two different temperatures and two different intrinsic layer thicknesses. The results clearly demonstrate that the recombination current in the R_{20} is generally smaller than that of the R_0 samples by one to two orders of magnitude.

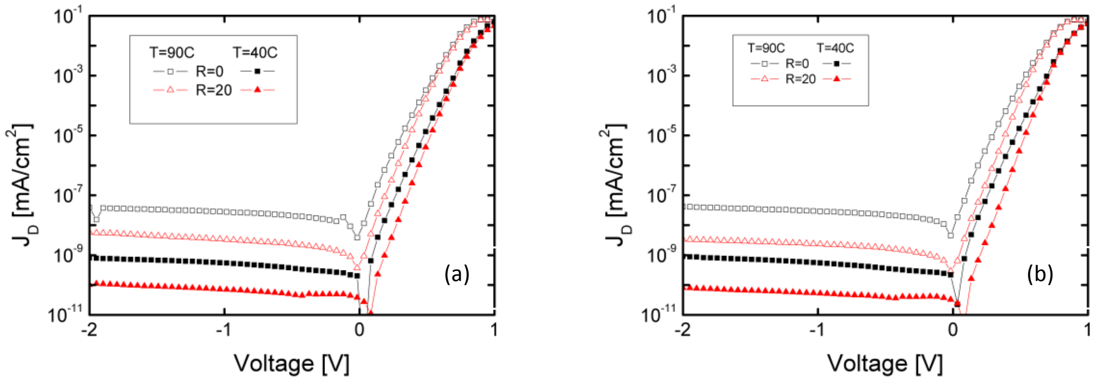

FIGURE 4-8: Dark IV curves for different hydrogen dilution ratios for (a) 600 nm i-layer sample and (b) 900 nm i-layer sample

We note that the dark current is the same for R_0 and R_{20}, in case of both intrinsic layer thicknesses shown here, for forward bias voltages above 0.8 V approximately. Furthermore, both material types show the same bending off of the dark current in this bias voltage region. Due to high levels of charge injection for these bias voltages, this is where the effect of series resistance in the material manifests itself in the dark current measurements. The bending off which is observed from 0.8 V and onwards is therefore characteristic of dominant series resistance in the device. Traditionally, the shunt resistance of a device/material is interpreted based on the dark current in the bias voltage region between 0 V and 0.7 V [43]. By the shape of the R_{20} dark current, it seems that the degree of shunt in these cells is far smaller than in the R_0 samples. This is in line with the interpretation of the external parameter results presented earlier, and it seems that both material types are equally prone to series resistance losses, whereas the R_{20} sample is less prone to shunt resistance losses. Furthermore, the dark current in the bias voltage range where SRH is dominant points to a smaller amount of contributing defects in the R_{20} material compared to the R_0. This, combined with the increased shunt losses, clearly corroborate the lower defect density in the R_{20} with respect to its undiluted counterpart.

Ideality Factor

The dark current of the R_{20} solar cells is visibly distinct from that of the R_0 solar cells. As discussed, it is likely that this reflects the lower defect density in the hydrogen diluted amorphous material.

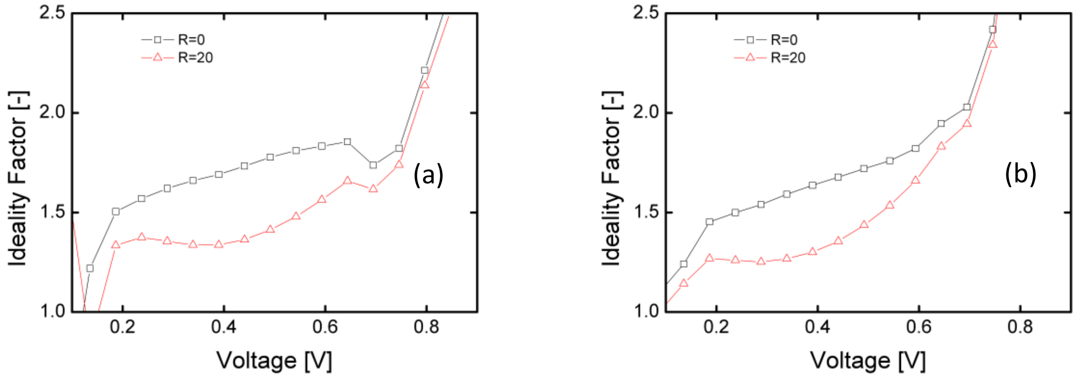

FIGURE 4-9: Ideality factors for different hydrogen dilution ratios of a 600 nm intrinsic layer sample for temperatures of (a)$T = 40$°C and (b)$T = 90$°C.

As illustrated in FIGURE 4-9 above, the change in material also affects the ideality factor of the dark current characteristics. Although not explicitly shown here, it is important to underline that the ideality factor is largely thickness independent in the case of the R_{20} devices. Therefore, the general material dependence is shown for only one thickness in FIGURE 4-9 – namely intrinsic layer of 600 nm. We note the strong overall reduction in the ideality factor in the voltage range where SRH recombination is dominant, i.e. 0.2 V to 0.7 V. According to the interpretation adopted previous discussions of this report, this implies a lower added density of defects which participate in the recombination current due to increased voltage. Therefore, a smaller level of spread in the energetic distribution of defects is expected in the R_{20} material compared to the R_0 material. Additionally, the shape of the R_{20} ideality factor differs significantly from that of the R_0 ideality factor. It is possible to distinguish the gentler slope of the curve between 0.2 V and 0.4 V, while a steeper slope characterizes the bias voltage range between 0.4 V and 0.7 V. Because the ideality factor represents the change in traps which participate as recombination centers due to a change in voltage, the slope of the ideality factor represents the increase/decrease in this change with respect to bias voltage. A steep slope therefore implies a rapid growth in increase of active trap states as a result of voltage change, while a less steep slope implies the opposite. As such, the slope of the ideality factor may also be interpreted as an indication of the energetic distribution of defects in the material. We note that the slope of the R_0 ideality factor is seemingly linear in the voltage range of interest, while the slope of the R_{20} ideality factor has an exponential profile.

Thermal Activation Energy of Recombination

The thermal activation energy is once again considered for the R_{20} samples. FIGURE 4-10 below depicts the activation energy of one R_{20} thickness series in the forward bias voltage range. Through linear fitting of the activation energy data, represented by the black line in the figure, we observe the same slope in this bias voltage region, but a different y-intercept, as compared to the R_0 activation energies.

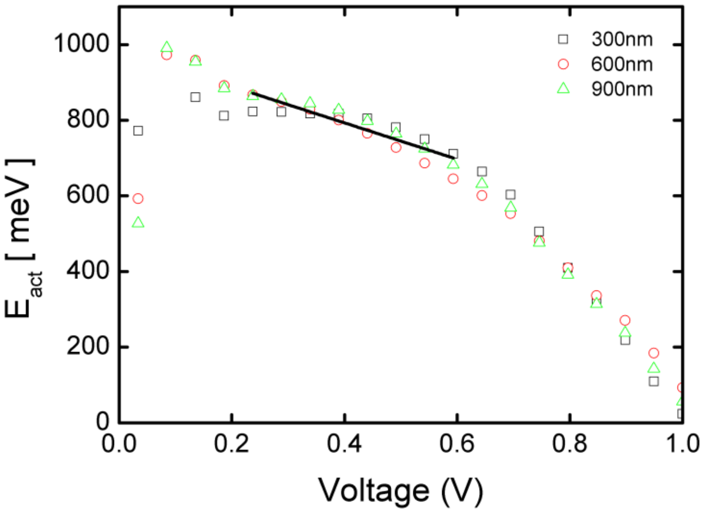

FIGURE 4-10: Thermal activation energy plot in forward for an R_{20} thickness series. Linear fit in voltage range which yields mobility gap is shown.

Consequently, the thermal ideality factor and the mobility bandgap of the R_{20} solar cells are calculated based on the linear fitting procedure, and Eq. 2-10. It is found that the thermal ideality factor is equal to $\mathrm{m_{th}} = 2.08$, which is consistent with theory, and, additionally, equal to the results obtained for the R_0 samples. Subsequently, the mobility gap is calculated, and found to be equal to $\mathrm{E_{mob}} = 1.85\ \mathrm{eV}$ for the R_{20} material. Thus, the results indicate a 0.2 eV increase in the mobility gap compared to the value of the R_0 material, which is significant. However, this is in line with the knowledge that increased hydrogen diluted causes an increase in the optical band gap of the amorphous material [35]. Hence, the mobility bandgap results presented here are consistent with existing knowledge, and evidence presented in this section, that the R_{20} material is of higher structural order and presumably less native defects, than its undiluted counterpart.

Chapter 5: Degradation Characteristics of a-Si:H Solar Cells

In this chapter, the experimental results pertaining to the degradation of the solar cells are presented, analyzed, and discussed. As previously indicated, one of the major motivations behind this project was to monitor the degradation of amorphous silicon solar cells under highly well-controlled conditions. We stress once again the benefit of carrying out in-situ measurements of solar cell performance throughout the degradation process. Through constant feedback based computer control, the environment provided within the solar cell degrader is subject to a minimum amount of fluctuations. Moreover, as the solar cells are never actually removed from the degradation setup for the sake of measurements, we may assume that the degradation parameters are safely fixed at the intended values. The intensity and wavelength of the light protruding from LEDs during degradation were kept constant for all degradation runs. The light intensity was set to $I = 350\ \mathrm{W/m^2}$ at a wavelength of $\lambda = 630\ \mathrm{nm}$. The choice of intensity was, as pointed out in Chapter 3, arbitrarily set to the intensity for which AM1.5 J_{SC} was obtained for the 600 nm intrinsic layer sample of the first R_0 thickness series. The choice of wavelength, on the other hand, was consciously chosen to be within the spectral region where a-Si:H is fairly transparent. As the SWE is most pronounced in the absorber layer, it is desirable to study the effect under illumination of light which is absorbed uniformly and deep within the device. Meanwhile, certain conditions were altered for the sake of this study, namely the sample thickness, degradation temperature, and hydrogen dilution of the absorber layer. The relevant results and comparisons are compiled in this chapter.

It is important to note that the results and comparisons shown in this section are averages based on the best performing cells after degradation. The monitored cells are the 10 most proficient ones, whose fill factors were within the 95% yield of the best performing cell in their as-degraded state. Thereby, the data processing ensures a representative average of measurements whose quality is already assured by their in-situ nature. The Matlab code used during data processing is found in Appendix C of this report. For the sake of clarity, we note here that the values of efficiency and J_{SC} which are measured by the in-situ degradation setup will differ from those under the AM1.5 spectrum. As can be seen from the EQE plots provided in the previous chapter, the quantum efficiency of the solar cells at the degradation light wavelength, $\lambda = 630\ \mathrm{nm}$, is relatively large compared to other parts of the spectrum. Therefore, elevated values of efficiency and J_{SC} are inevitably obtained, as will become evident in the coming sections.

5.1 Effect of Thickness on Degradation Characteristics

Previous studies have shown that an increased absorber layer thickness leads to higher level of light induced degradation in a device [26] [28]. Therefore, this sub-chapter offers an in-depth analysis of the evolution of the degradation characteristics of solar cells of different thicknesses. Simulation work performed within the PVMD group at TU Delft has shown that the light induced degradation of the solar cells can be modeled by assuming an increase in defect density throughout the intrinsic layer [31]. Thus, an experimental analysis based on differentiation of absorber layer thickness may shed valuable light on SWE kinetics within an a-Si:H solar cell.

5.1.1 External Parameters

As shown in the previous chapter, the initial values of the solar cell performance parameters show a large degree of variation with the intrinsic layer thickness. We attribute these differences to the characteristics of a-Si:H, and especially with respect to the defects within the solar cell material. The goal of this section will be to outline the evolution of degradation of the external parameters. Moreover, we will discuss how this varies with absorber layer thickness, and the impact this has on the final state of the device after degradation.

In FIGURE 5-1, seen below, the evolution of the external parameters of an R_0 thickness series degraded at a temperature $\mathrm{T} = 25°\mathrm{C}$ is illustrated. The solar cells were degraded for approximately 720 hours, until signs of leveling off were observed in the external parameters. The external parameter degradation evolution is shown both in terms of relative and absolute values. As the plots illustrate, the final state of the solar cell consistently worsens as the intrinsic layer thickness grows, independent of the initial value of given external parameter. This is in line with previous findings, which show an improved resistance to light induced degradation for thinner devices [52]. We note that the thinnest device degrades to about 70% of its initial efficiency in the experimental time interval, whereas the thicker cells degrade to about 50%-45% of their initial conversion efficiencies.

The fill factor and the V_{OC} degradation curves of the different R_0 devices show trends which seem to be less influenced by the thickness of the device. This is particularly visible in the relative plots of the external parameters, where V_{OC} in particular degrades very similarly for the three thicknesses. In terms of electric field effects in the device, this trend means that the light induced defects which are generated in the device are perturbed by the electric field to the same extent regardless of the electric field strength. Because of band bending near the interfaces of the p-i-n structure, the electric field is the strongest around these regions. This feature grows stronger for thinner cells, as the band bending is more abrupt. Meanwhile, the middle part of the cell sees an electric field which is relatively weak and constant compared to the interface regions. The V_{OC} results may imply that defects are generated in this region of the device, where the electric field profile is weak, and similar for all intrinsic layer thicknesses. This is in line with other theories that defect generation occurs deep within the device, as discussed earlier [53] [54].

The degradation curves of solar cell efficiency and short circuit current point to the fact that there are two dissimilar patterns in play – that of the thicker cells, i.e. with an intrinsic layer thickness of 900 nm and 600 nm, and that of the thinner cell, i.e. with an intrinsic layer thickness of 300 nm. Indeed, the 300 nm difference in intrinsic layer thicknesses between the thickest devices does not seem to influence the degradation pattern and final state of the device much. Meanwhile, the same thickness increase yields a very different degradation pattern when going from a 300 nm intrinsic layer to a 600 nm intrinsic layer. A 30%-35% decrease in J_{SC} is observed in the thicker devices, while the 300 nm intrinsic layer device shows a relative J_{SC} decrease of approximately 7%. As such, a threshold value in thickness seems to be present, for which the material degradation under red light soaking causes a barrier which dramatically impedes charge carrier propagation. As seen in FIGURE 4-1, this was also the case for the initial performance values of the R_0-type solar cells; the thickness dependence of V_{OC} seems to be reproduced in the fill factor, while the J_{SC} thickness dependence is reproduced in the efficiency of the device.

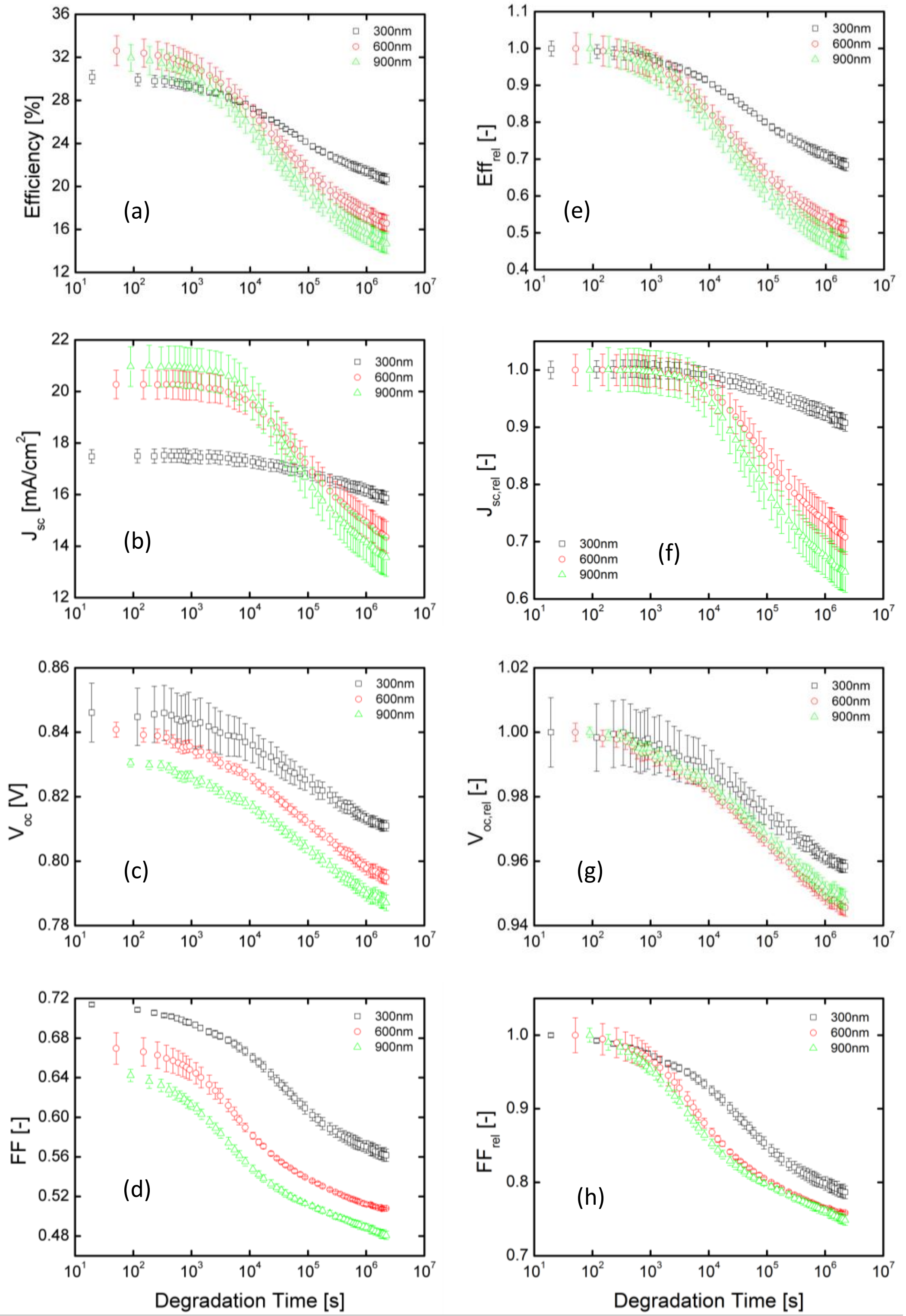

FIGURE 5-1: Degradation evolution of R_0 solar cells' external parameters presented for $T = 25℃$ and three intrinsic layer thicknesses. Plots (a)–(d) present the absolute values, while plots (e) – (h) show the relative degradation of the solar cells.

Efficiency Fitting

As in discussed in Chapter 2, the degradation in a-Si:H solar cell efficiency is often regarded as a quantitative measure of defect density alterations within the amorphous material. Using equation Eq. 2-19, the fitted efficiency curves shown in FIGURE 5-2 are produced. Moreover, TABLE 5-1 provides an overview of the fitting parameters, which may be interpreted in terms of defect and degradation kinetics. In FIGURE 5-2, the absolute efficiency plots shown in FIGURE 5-1 are plotted again, with the corresponding fitted stretched exponential curve. For the sake of clarity in the plot, only a representative amount of experimental data points are shown. In order to underline the quality of the fit, and the fact that these correspond well with all the data collected, the complete figures are shown plotted in Appendix A of this report with all data points included. As the figure demonstrates, fitted curves are in good agreement with the experimental data. The Matlab code for the fitting routine is found in Appendix C of this report.

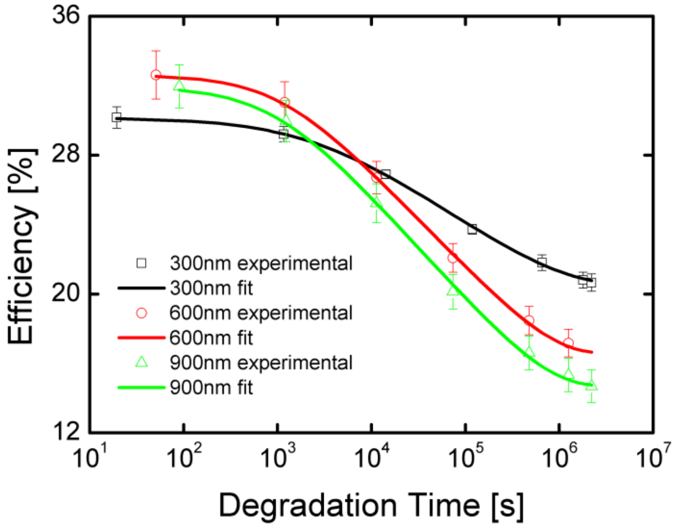

FIGURE 5-2: Fitted efficiency curves for an R_0 thickness series degraded at $T = 25°C$

The dispersive fitting parameter, β, is indicative of how abruptly the slope of the efficiency curve changes throughout the degradation process. Thereby, β yields information related to the magnitude of the efficiency change per unit time. Thus, it is possible to relate β to τ and the solar cell efficiencies through Eq. 5-1 as seen below.

$$\beta \propto \frac{\eta_{initial} - \eta_{final}}{\tau} \qquad \text{Eq. 5-1}$$

As the experimental plots, as well as the values for β, reveal, the thickest devices show a significantly larger density drop per unit time for the given time interval than the 300 nm intrinsic layer sample. The time constant, τ, indicate that the solar cell efficiency levels off later for the thinner devices than for the thicker ones. Similar orders of magnitude for values of τ for R_0 material have been reported in previous studies [35]. Thus, the dispersive coefficient, β, and the time constant, τ, found here are consistent with the real trends in the experimental data, as well as published literature.

Absorber Layer Thickness	n [-]	τ [hours]	β [-]	$\eta_{initial}$ [%]	η_{final} [%]
300 nm	1.76	207.35	0.73	30.17	20.504
600 nm	3.02	202.92	1.07	32.61	16.56
900 nm	2.93	180.19	1.03	31.96	14.68

TABLE 5-1: Fitting parameters for the efficiency as given by equation Eq. 2-19 for an R_0 thickness series degraded at $T = 25°C$

As discussed in Chapter 2, the fitting parameter n is defined in Eq. 2-20 as the logarithm of the ratio of total density of potential defect sites and the initial defect density within the absorber layer. While making sure to interpret this parameter with care, one may note the distinct increase when passing from a 300 nm intrinsic layer to thicker layers. On the basis of the definition of n, this could imply a higher total density of potential defect sites in the thicker devices.

Fill Factor Fitting

As is the case for the conversion efficiency, the evolution of solar cell fill factor during degradation is often considered in directly related to the kinetics of fill factor [35] [55]. The degradation scheme of amorphous silicon is, fairly consistently, considered as made up of two regimes of defect creation; an initial fast regime, and a long-lasting slow regime. Through numerous modeling efforts, the kinetics of the initial defect creation regime have been calculated and found to obey a certain power-law with respect to time [56] [44] [30]. In literature, it is therefore common to find fixed relations of defect concentration such that $N_D \propto t^x$, where N_D is the defect density in the material, t is the time, and x is a time exponent. Values of x that are commonly found as a result of modeling to be 1/3 or 1/2 [20] [28] [57].

In this project, the degradation of the fill factor was analyzed in terms of the fast and slow regime described in the previous paragraph. As can be seen in FIGURE 5-3, the evolution of the normalized, log-scaled fill factor is plotted for R_0-type solar cells of different thicknesses. In this way, the fast and slow regimes of fill factor degradation are rendered more visible.

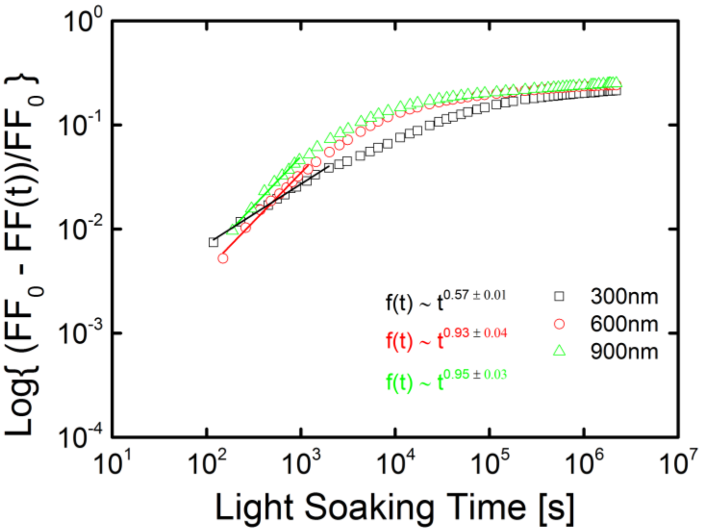

FIGURE 5-3: Normalized, log-scaled fill factor plots of R_0 cells of varying thicknesses with a linear fit of the initial time period. Indicated in the plots are also the relations of fill factor with time.

Moreover, linear fits are made in the region which is considered as representative of the fast degradation. The linear fits yield a certain time exponent, *x*, as described in the previous paragraph, for each of the three curves. In light of the assumption that the fill factor of the solar cells is proportional to the defect density of the material, the time exponents resulting from the fill factor fittings yield an interesting result. The resulting time-exponents are noted in TABLE 5-2, seen below.

Absorber Layer Thickness	Time Exponent
300 nm	0.57±0.01
600 nm	0.93±0.04
900 nm	0.95±0.03

TABLE 5-2: Time exponent value for the fitted region of the fill factor plots in FIGURE 5-3.

In contrast to what is suggested in literature, the value of the time exponent as presented here is not fixed, but rather varies with the intrinsic layer thickness of the device. This may suggest that the kinetics of degradation are not fully described in the models referred to previously.

5.1.2 EQE

In the previous chapter, it was shown that the thickness of the solar cell had a decisive impact on the spectral response of the solar cell. FIGURE 5-4 shows how the degradation of an R_0 solar cell evolves for three different intrinsic layer thicknesses. The EQE degradation shown in the figure below is, as noted earlier, due to a 720 hour light soak at a wavelength of $\lambda = 630\ \mathrm{nm}$ and $\mathrm{T} = 25°\mathrm{C}$. We note the significant increase in performance loss as the intrinsic layer thickness is increased. This is consistent with previous EQE measurements after light induced degradation [51]. Moreover, the EQE degradation occurs across the entire spectral range. In the long wavelength region ($\lambda > 600\ \mathrm{nm}$), the initial EQE of the thicker solar cells surpassed that of the thinner ones. In the degraded state, however, the order of EQE has been reversed in this region.

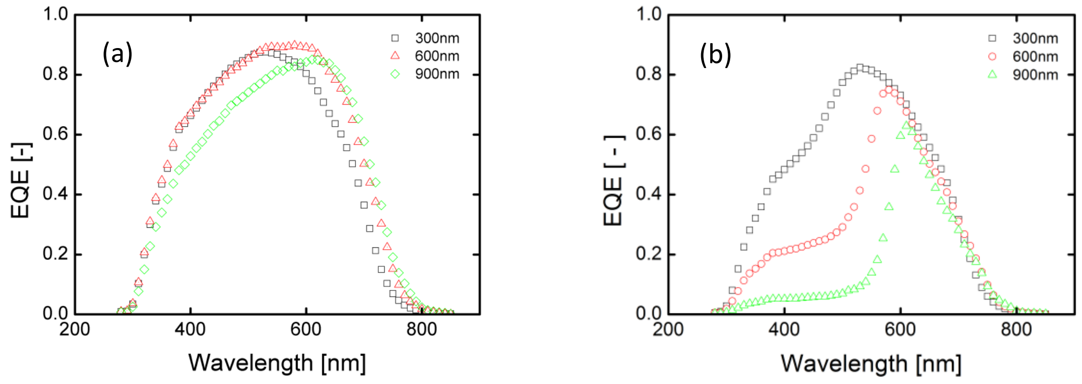

FIGURE 5-4: EQE curves for an R_0 thickness series shown (a) before and (b) after degradation at $\mathrm{T} = 25°\mathrm{C}$ for 720 hours under red light illumination

The strongest performance loss, however, occurs in the shorter wavelength region ($\lambda < 600\ \mathrm{nm}$). Herein, the thickness trend is even more pronounced than for longer wavelengths. Furthermore, the wavelength for which the EQE peaks gradually increases from 550 nm to 600 nm as the absorber layer thickness increases. In other words, both the magnitude of the LID *and* the spectral range over which the most pronounced LID occurs, increases with the thickness of the device. The degradation evolution of EQE has been modeled with reasonable accuracy by assuming defect generation throughout the intrinsic layer [31]. It is clear that the collection of charge carriers generated by shorter wavelengths, i.e. near the p-i interface as discussed in Chapter 4, is the most deficient and most affected by LID. This may imply that the defects generated in the intrinsic layer pose a larger hinders to propagation in the amorphous material for electrons than holes. This interpretation is based on the observation that the response for longer wavelengths, of which a significantly larger proportion is due to charge carrier generation near the i-n interface region, remains relatively elevated for increasing thickness of the i-layer.

5.2 Effect of Temperature on Degradation Characteristics

Applying thermal loads to the amorphous material is known to reduce LID significantly [26]. Additionally, the temperature coefficients of the a-Si:H external parameters are low [15]. This is in contrast to crystalline silicon, for which a temperature increase yields significant changes for all external parameters. Thus, the temperature dependence of a-Si:H is dominated by the role of SWE, or that of thermal annealing, to be more specific. As the SWE is an equilibration process between the light induced generation of metastable defects and consequent thermal annealing, probing this temperature dependence can yield valuable insight to the amorphous material. In this section, the results of the degradation will be presented for different degradation temperatures. Once again the importance of an in-situ degradation setup is stressed, particularly when temperature effects are to be monitored in the amorphous material. Because a-Si:H annealing kinetics is very sensitive to temperature changes, the in-situ measurement allows for monitoring the degradation process without doubting whether observed effects are merely results of temperature fluctuations while performing measurements. The SWE is inherently linked to the amorphous material, and, as seen in the previous section, its severity consequently scales with the amount of a-Si:H in a device (i.e. the intrinsic layer thickness). Therefore, the thickest solar cells, i.e. with an intrinsic layer thickness of 900 nm, were selected for the presentation in this section for the sake of a clear and effective comparison. The figures pertaining to devices of 300 nm and 600 nm intrinsic layer thickness are found in Appendix A of this report.

5.2.1 External Parameters

The effect of temperature on the external parameters is shown for two different devices in FIGURE 5-5, as seen below. The external parameters are plotted for two 900 nm intrinsic layer devices – one R_0 solar cell and one R_{20} solar cell. The R_0 samples were degraded at two temperatures, while the R_{20} samples have been degraded at three distinct temperatures. The temperature increase of the solar cells has the same effect in both type of material – a higher stabilized efficiency. Higher stabilized values are also found for J_{SC} and fill factor of the solar cells. The V_{OC}, however, is consistently reduced as the temperature increases. This is due to the thermal energy which is being provided to the charge carriers within the material. Thereby, electrons may occupy higher energy states. Essentially, this equates a reduction in the effective bandgap of the material, i.e. a lower V_{OC}. The degradation pattern of the external parameters evolves in the same way with temperature increase as it does for an increased thickness. While the shape of the degradation curve for J_{SC} and efficiency is distorted with temperature increase, resulting in interception of these curves in the period of light soaking, V_{OC} and fill factor evolve more or less in parallel, albeit with a different starting point.

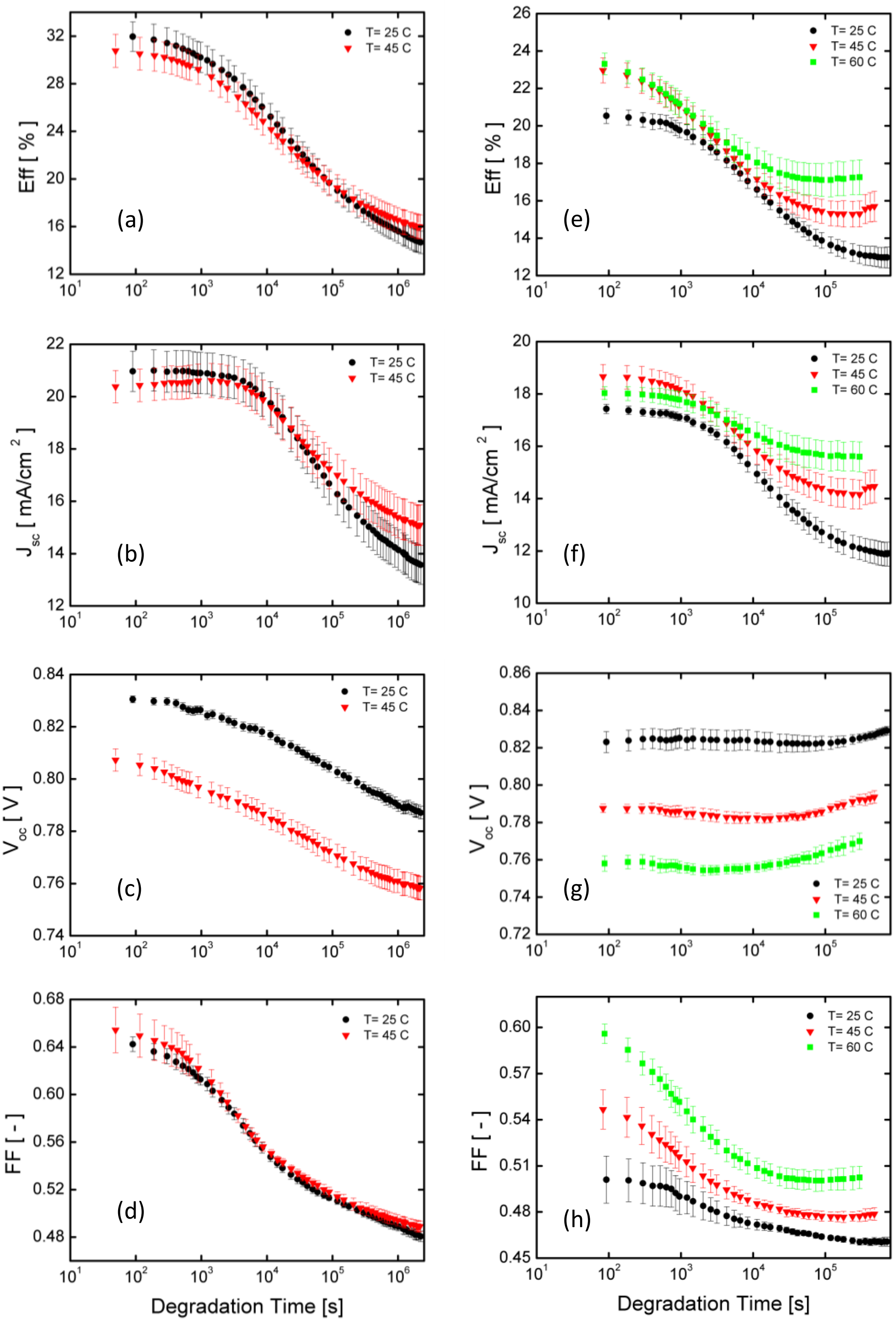

FIGURE 5-5: Degradation evolution of 900 nm intrinsic layer solar cell external parameters presented for different temperatures. Plots (a)–(d) present the external parameters of an R_0 device, while plots (e)–(h) show that of an R_{20} device.

Efficiency Fitting

In order to take a closer look at the efficiency degradation, and the impact of temperature herein, we make use of the fitting model cited in Chapter 2 of this report, i.e. Eq. 2-19. In FIGURE 5-6 below, the efficiency of a 900 nm cell of both R_0 and R_{20} material has been fitted for the different degradation temperatures. The quality of the fit speaks to the range of application of the fitting model, which handles intrinsic layer thickness change, as seen in the previous section, as well as degradation temperature alterations, as seen below.

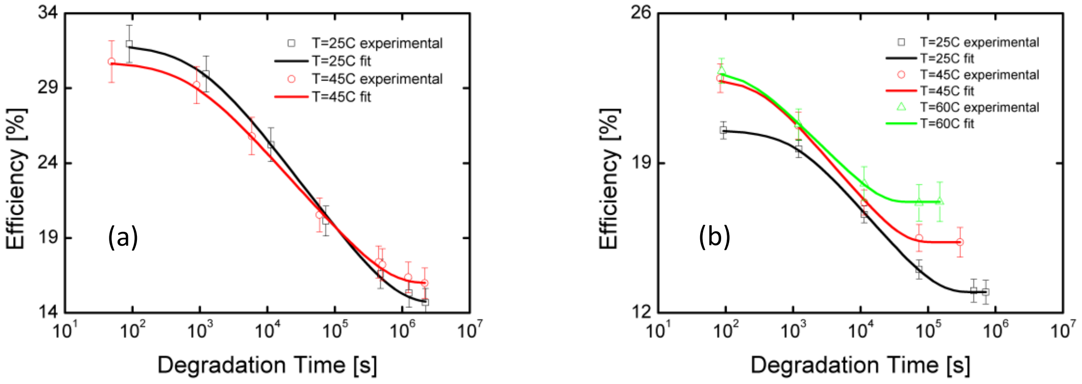

FIGURE 5-6: Degradation evolution of 900 nm intrinsic layer solar cell efficiencies presented for different temperatures. Plot (a) presents the efficiency of an R_0 device, while plot (b) shows that of an R_{20} device.

The fitting parameters are found in TABLE 5-3 and TABLE 5-4 for R_0 and R_{20} samples, respectively. The dispersive parameter, β, shows a tendency to increase with increasing temperature. As pointed out in the previous section, this points to an increased rate of efficiency change. This may seem contradictory to the fact that less degradation is observed. However, by employing Eq. 5-1 it is clear that the efficiency degradation per unit time increases with increasing temperature.

Degradation Temperature [°C]	n [-]	τ [hours]	β [-]	$\eta_{initial}$ [%]	η_{final} [%]
25	2.93	180.19	1.03	31.96	14.68
45	3.13	140.9	1.08	30.77	15.98

TABLE 5-3: Fitting parameters for the efficiency as given by equation Eq. 2-19 for a 900 nm intrinsic layer R_0 sample

Meanwhile, the time constant, τ, shows a clear decrease for higher temperatures. Thus, the solar cell efficiencies do not only stabilize at higher efficiencies as temperature increases, they also stabilize *sooner*. This implies that the equilibration process between defect creation and thermal annealing finds an equilibrium quicker, at higher temperatures, where the thermal annealing process is growing more and more dominant in the solar cell.

Degradation Temperature [°C]	n [-]	τ [hours]	β [-]	$\eta_{initial}$ [%]	η_{final} [%]
25	2.81	32.26	1.37	20.54	12.97
45	3.13	10.1	1.52	22.97	15.3
60	3.51	5.10	1.78	23.31	17.19

TABLE 5-4: Fitting parameters for the efficiency as given by equation Eq. 2-19 for a 900 nm intrinsic layer R_{20} sample

Finally, the evolution of *n* indicates a discernible increase as the temperature of the solar cells rises. As this fitting variable is proportional to the ratio of total density of potential defect sites and the initial defect density within the absorber layer, this may be interpreted in terms of a decrease in initial defect density in the material as a result of temperature increase. This interpretation is in line with the fact that higher of levels of thermal annealing of defects are naturally obtained at higher temperatures. Moreover, the higher initial values for efficiency and fill factor due to increased temperature are consistent with this explanation of the evolution of *n*.

Fill Factor Fitting

The fill factor degradation plots are once again normalized to their initial value and log-scaled in order to analyze the different degradation regimes of the devices. In FIGURE 5-7, the fill factor plots of two different thickness series of R_0-type material are shown for two different degradation temperatures.

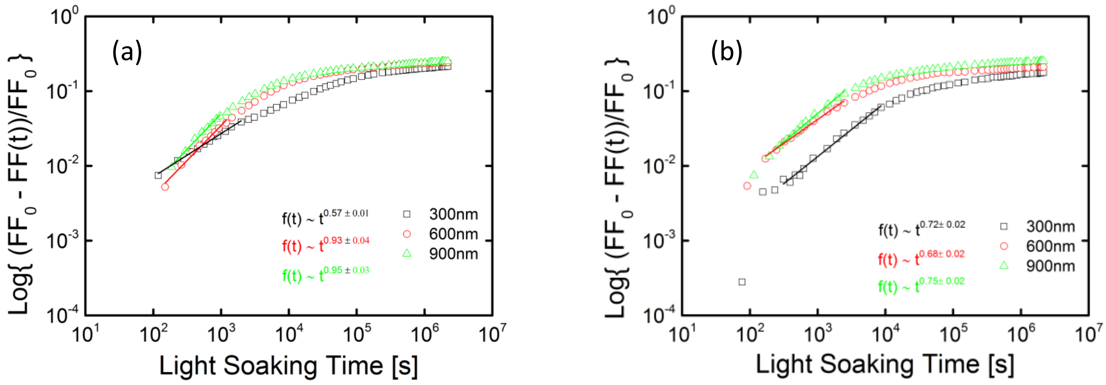

FIGURE 5-7: Normalized, log-scaled fill factor plots of R_0 cells of varying thicknesses with a linear fit of the initial time period. Indicated in the plots are also the relations of fill factor with time. The plots show the fill factor evolution for (a) $T = 25°C$ and (b) $T = 45°C$

Furthermore, the plots once again show the fitted curves in the fast part of the degradation scheme. Herein, the fits are made to obtain the relation of fill factor with time, and the time exponent, *x*, which modulates this proportionality as described in the previous section. The time exponent resulting from the fittings portrayed in FIGURE 5-7 are listed in TABLE 5-5 below. The increase in temperature clearly affects the degradation kinetics of the R_0-type solar cells. Meanwhile, the impact on the cell with temperature seems to vary with thickness. While the temperature increase seems to yield a more rapid defect generation in the thinner cell, the time exponent of the 600 nm and 900 nm intrinsic layer cells shows a distinct decrease due to the change in temperature. Moreover, the time exponent of the three samples is more or less equal in the case of higher degradation temperature, thus underlining the thermal dependence of the degradation kinetics. Once again, the experimental results suggest that the degradation kinetics of the a-Si:H devices do not simply obey a singular power law-but rather that the time exponent is a variable entity.

Absorber Layer Thickness	*x* at $T = 25°C$	*x* at $T = 45°C$
300 nm	0.57±0.01	0.72±0.02
600 nm	0.93±0.04	0.68±0.02
900 nm	0.95±0.03	0.75±0.02

TABLE 5-5: Time exponent value for the fitted region of the fill factor plots in FIGURE 5-7.

5.2.2 EQE

The external quantum efficiency of a solar cell of the same intrinsic layer thickness, degraded at different temperatures, is studied in this sub-section. As shown in FIGURE 5-8(a), the increase in degradation temperature has a remarkable, positive effect on the R_0 EQE. The gain in EQE with a 20°C increase in solar cell temperature during degradation is observed for the entire spectral range. Meanwhile, the EQE enhancement in the shorter wavelength region ($\lambda < 600\ \mathrm{nm}$) is far more significant than the enhancement observed in the longer wavelength region. In terms of the EQE interpretation of the previous sub-chapter, it seems that mainly the electron propagation throughout the material is improved by increasing the temperature. Consequently, we expect that increased degradation temperatures imply partial annealing of light induced defects throughout the intrinsic layer.

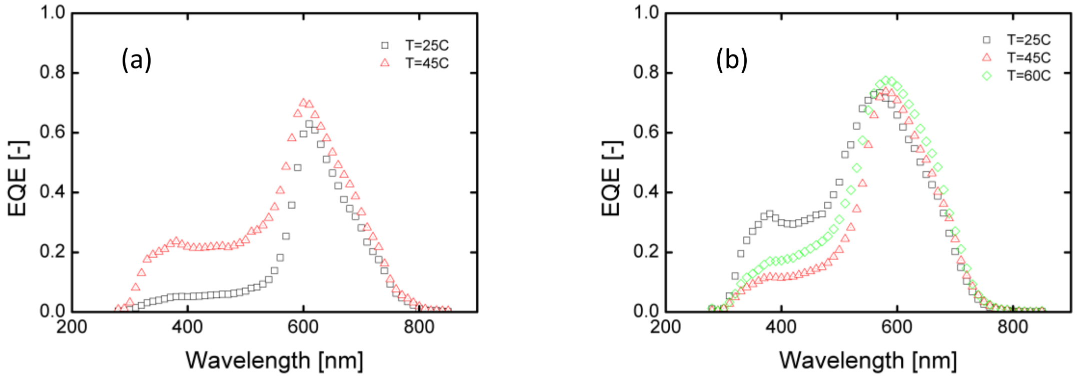

FIGURE 5-8: EQE curves for degraded state of 900 nm intrinsic solar cells degraded at different temperatures. The plots here show the EQE of (a) R_0 type material, and (b) R_{20} type material.

The R_{20} solar cells, depicted in FIGURE 5-8(b), however, do not respond in the same way to the increase in degradation temperature. In the shorter wavelength region ($\lambda < 600\ \mathrm{nm}$), the EQE is negatively influenced by the increase in temperature from $\mathrm{T} = 25°\mathrm{C}$ and $\mathrm{T} = 45°\mathrm{C}$. When the degradation temperature increases from $\mathrm{T} = 45°\mathrm{C}$ to $\mathrm{T} = 60°\mathrm{C}$, the shorter wavelength EQE is increased, yet it still remains lower than that of the cell degraded at $\mathrm{T} = 25°\mathrm{C}$. This artifact may seem like a discrepancy in light of the J_{SC} degradation curves shown in Figure 5.4 (g), which clearly shows that J_{SC} stabilizes at higher values with increased degradation temperature. However, this is not necessarily contradictory with the EQE results, as the degradation was carried out at a wavelength of $\lambda = 630\ \mathrm{nm}$, for which the spectral response adequately reflects the J_{SC} levels after degradation. It is therefore an interesting result that the overall J_{SC} (i.e. spectrally integrated EQE) is *not* positively influenced by the increase in degradation temperature for the R_{20} solar cells. According to the EQE results, we expect that this characteristic will occur for solar cell efficiencies in the degraded state also. The degraded efficiency of the samples will be presented and discussed in the next chapter.

Meanwhile, the longer wavelength EQE shows a small, yet consistent enhancement as degradation temperatures increase. According to the previous interpretation in this chapter, this may imply that the defects which obstruct hole propagation in the material are relatively easily annealed away by applying a larger thermal load. Meanwhile, the EQE evolution in the shorter wavelength region remains an anomaly. The distinct and remarkable difference in EQE results between the R_0 and R_{20}

solar cells calls for a more in-depth analysis of the two material types. Consequently, the next section of this report treats the effect of hydrogen dilution on the degradation characteristics.

5.3 Effect of Hydrogen Dilution on Degradation Characteristics

As discussed in previous chapters, diluting the silane gas with hydrogen during deposition of the absorber layer modifies the nanostructure herein, and hence, the solar cell performance. Naturally, alterations within the solar cell material structure will cause deviations in performance. We showed in the previous chapter that a higher mobility bandgap is expected for the R_{20} than for R_0 type material. Moreover, the initial performance of the hydrogen diluted solar cells show different thickness dependence than the undiluted samples, as shown in Chapter 4. It has been shown that hydrogen diluted solar cells show higher stabilized efficiencies than undiluted solar cells [34] [35]. Meanwhile, the initial characteristics presented in Chapter 4 of this report indicate lower initial solar cell performance for R_{20} samples compared to R_0. Consequently, this section highlights the differences in degradation patterns and characteristics between the undiluted and the diluted solar cells. Direct comparisons are made between the different solar cells at degradation temperatures of $\mathrm{T} = 25℃$ and $\mathrm{T} = 45℃$. Although a sample set of R_{20} material was degraded at $\mathrm{T} = 60℃$, as documented in the previous section, this was not carried out for R_0 solar cells due to time constraints. For reasons explained in the previous section, the thickest solar cells, i.e. with an intrinsic layer thickness of 900 nm, were selected for the presentation in this section for the sake of a clear and effective comparison. The figures pertaining to devices of 300 nm and 600 nm intrinsic layer thickness are found in Appendix A of this report.

5.3.1 External Parameters

The differences in degradation evolution of the external parameters of the R_0 and R_{20} solar cells are highlighted in this section. FIGURE 5-9 compares the degradation characteristics for two different temperatures; $\mathrm{T} = 25℃$ and $\mathrm{T} = 45℃$. The solar cells for which the external parameters are plotted below have an intrinsic layer thickness of 900 nm. As noted previously, the light soaking times are based on the point of stabilized efficiency, and therefore there is a difference in number of measurement points. The R_0 cells degraded at $\mathrm{T} = 25℃$ and $\mathrm{T} = 45℃$ were degraded for 720 hours and 200 hours, respectively. Meanwhile, the R_{20} samples were degraded at $\mathrm{T} = 25℃$ and $\mathrm{T} = 45℃$ for 200 hours and 132 hours, respectively.

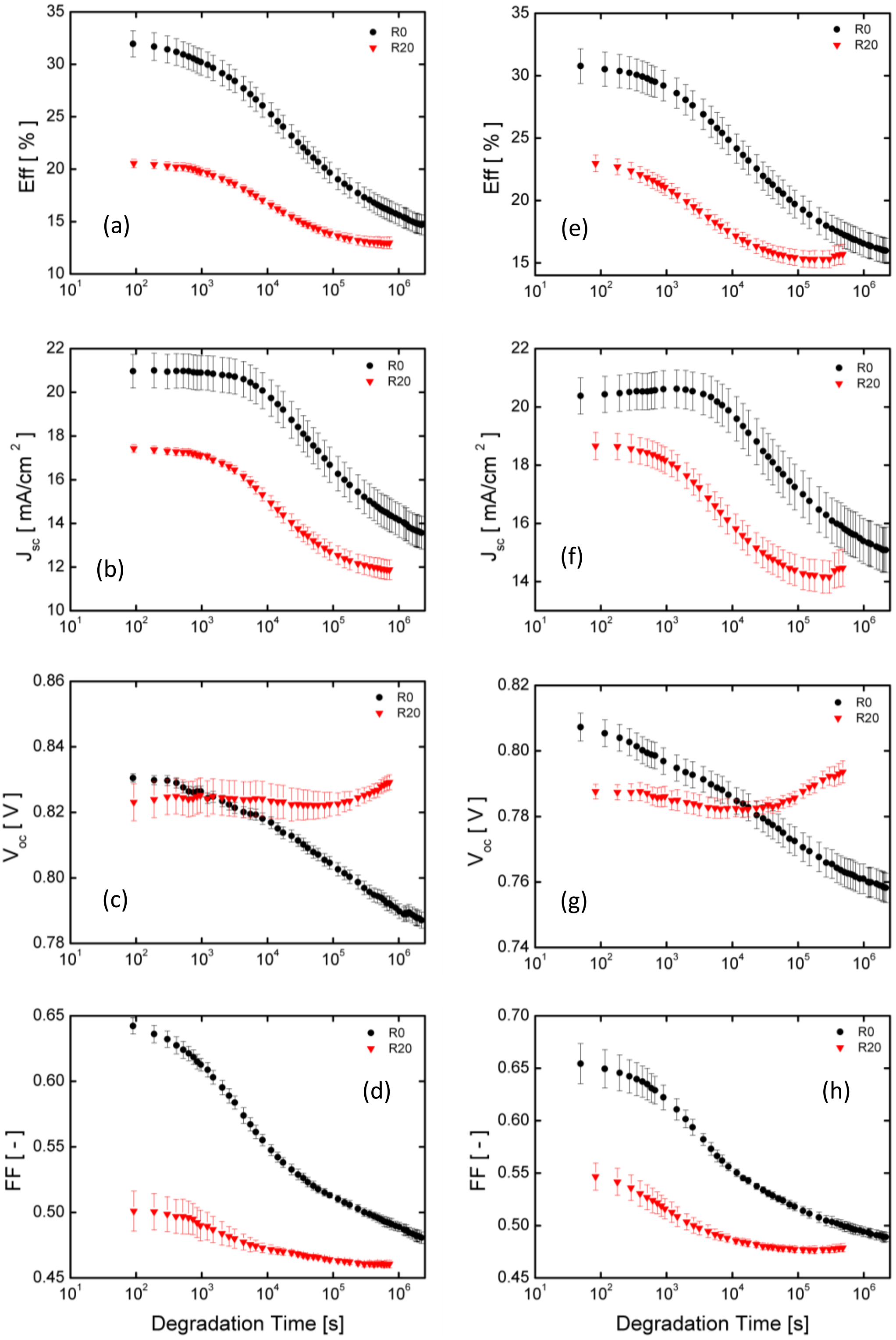

FIGURE 5-9: Degradation evolution of R_0 and R_{20} 900 nm intrinsic layer solar cell external parameters presented for different temperatures. Plots (a)–(d) present the external parameters for a degradation temperature of $\mathrm{T} = 25^{\circ}\mathrm{C}$, while plots (e)–(h) show external parameters for a degradation temperature of $\mathrm{T} = 45^{\circ}\mathrm{C}$.

The degradation patterns show clear trends of earlier stabilization for R_{20} devices, as well as a significant difference in relative degradation as compared to R_0. The efficiency curves level off sooner for the hydrogen diluted samples and would presumably intercept the R_0 degradation curves at its stabilized value. At $\mathrm{T} = 25°\mathrm{C}$, the absolute gain of hydrogen dilution is therefore limited. Meanwhile, the point of interception with the R_0 efficiency curve is higher at higher temperatures – i.e. the R_{20} material benefits stronger from a higher degradation temperature. The same is true for the fill factor of the solar cells presented here.

Referring back to FIGURE 4-6 of the previous chapter, where the initial external parameters of the R_{20} solar cells were presented, there assumed to be a faulty p-layer in these samples. Ultimately, this leads to initial values which are lower than expected for the hydrogen diluted devices. Therefore, we stress the evolution seen above in relative terms. The relative plots of the curves seen above can be found in Appendix A.

The J_{SC} of the two material types degrade similarly. Meanwhile, the initial increase in J_{SC} of R_0 cells during degradation at $\mathrm{T} = 45°\mathrm{C}$ is not observed in the R_{20} samples. The most striking difference in degradation behavior between the two material types, however, pertains to the open circuit voltage. As seen in FIGURE 5-9, the V_{OC} of the R_0 solar cells shows a clear and constant deterioration for both temperatures. In the case of undiluted solar cells, the V_{OC} does not show a tendency to level off. The increase in temperature merely lowers the starting point of the R_0 V_{OC}, as seen in previous sub-sections. Meanwhile, the open circuit voltage of the R_{20} material remains more or less constant throughout the entire degradation process. Additionally, the V_{OC} of the R_{20} solar cells show a tendency to increase after about 30 hours of light soaking, surpassing initial values by the end of the degradation experiment. There are previous reports of V_{OC} increasing as a result of degradation, which is explained as an increase in doping efficiency in n-layer and p-layer during light soaking [35]. Meanwhile, the figures indicate that the increase is more and more significant as the temperature increases. This effect is well demonstrated in FIGURE 5-5(h) in the previous section. A possible interpretation is that this trend in V_{OC} may also be caused by an increased doping efficiency in the doped layers, which would naturally increase with temperature.

Efficiency Fitting

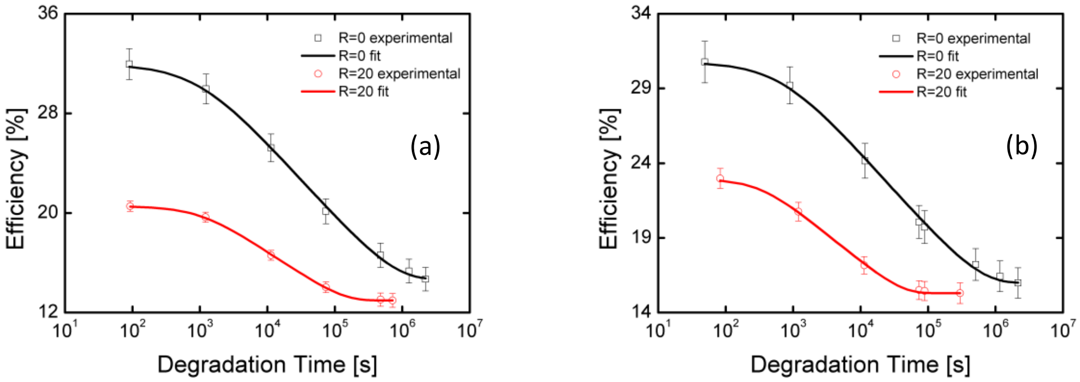

FIGURE 5-10: Degradation evolution of conversion efficiency for different hydrogen dilutions. The figures show the efficiency degradation at a temperature of (a) $\mathrm{T} = 25°\mathrm{C}$, and (b) $\mathrm{T} = 45°\mathrm{C}$.

The efficiency curves seen above were fitted using the same procedure as in previous sections. FIGURE 5-10 above shows the fitted curves for degradation of R_0 and R_{20} solar cells for two different degradation temperatures.

The fitted curves are in good agreement with the experimental data. Once again, only a few representative experimental data points are displayed in the plots for the sake of clarity. The fitting parameters are listed in TABLE 5-6 and TABLE 5-7, below, for degradation temperatures of $\mathrm{T} = 25°\mathrm{C}$ and $\mathrm{T} = 45°\mathrm{C}$, respectively. The dispersion parameter, β, shows a clear increase when passing from R_0 material to R_{20} material. Indeed, the amount of time over which the full degradation occurs is much shorter, resulting in the larger values of this parameter which modulates the stretch in the fitting function. Moreover, this means that the amount of efficiency degradation per unit time is larger for the R_{20} material, according to the relation given in Eq. 5-1.

This is also reflected in the time constant, τ, which consistently decreases as the hydrogen dilution in the material increases. We note that the relative reduction in stabilization time when passing from a degradation temperature of $\mathrm{T} = 25°\mathrm{C}$ to $\mathrm{T} = 45°\mathrm{C}$ is about 67% for the R_{20} samples, compared to 22% in the case of R_0 solar cells.

Hydrogen Dilution, R [-]	*n* [-]	τ [hours]	β [-]	$\eta_{initial}$ [%]	η_{final} [%]
0	2.93	180.19	1.03	31.96	14.68
20	2.81	32.26	1.36	20.54	12.97

TABLE 5-6: Fitting parameters for the efficiency as given by equation Eq. 2-19 for 900 nm intrinsic layer R_0 and R_{20} samples degraded at $\mathrm{T} = 25°\mathrm{C}$

Hydrogen Dilution, R [-]	*n* [-]	τ [hours]	β [-]	$\eta_{initial}$ [%]	η_{final} [%]
0	3.13	140.9	1.08	30.77	15.98
20	3.13	10.1	1.52	22.97	15.3

TABLE 5-7: Fitting parameters for the efficiency as given by equation Eq. 2-19 for 900 nm intrinsic layer R_0 and R_{20} samples degraded at $\mathrm{T} = 45°\mathrm{C}$

Finally, *n*, which is defined in Eq. 2-20 as being proportional to the ratio of total density of potential defect sites and the initial defect density within the absorber layer, shows the least clear trend of all the fitting parameters. In the case of a degradation temperature of $\mathrm{T} = 25°\mathrm{C}$, *n* decreases noticeably with increasing hydrogen dilution. In line with the interpretations presented in the previous section, this may imply that the total density of potential defect sites is higher in the undiluted material. This is consistent with the supposed higher order of structure within the R_{20}-type material [35]. Meanwhile, for a degradation temperature of $\mathrm{T} = 45°\mathrm{C}$, the *n*-value of the fitting curves are equal. A possible explanation for this could be that the thermal annealing effects have a stronger impact on the diluted than the undiluted material when increasing the temperature by 20°C. Thereby, the initial defect density of the R_{20} material may drop significantly more than of the R_0 device, leading to an *n*-value which is more or less the same for the two devices. This is also in line with the impact that the temperature increase has on the two types of materials. The degradation temperature increase yielded a relative enhancement in final efficiency of 20% for the R_{20} devices. Meanwhile, the relative enhancement in final efficiency of the R_0 was around 8%. This is consistent with the interpretation of the results for the *n*-value as presented in this section. Meanwhile, it is underlined that *n* is a variable which remains difficult and dubious to interpret.

Fill Factor Fitting

Once more, the fill factor evolution of the solar cells is considered in closer detail. FIGURE 5-11 shows the normalized log-scaled fill factor plots of the fill factor degradation for R_0-type and R_{20}-type material degraded at $T = 25°C$. Thereby, the fast and slow regimes described in previous sections are rendered visible, and the initial, fast degradation regime is fitted.

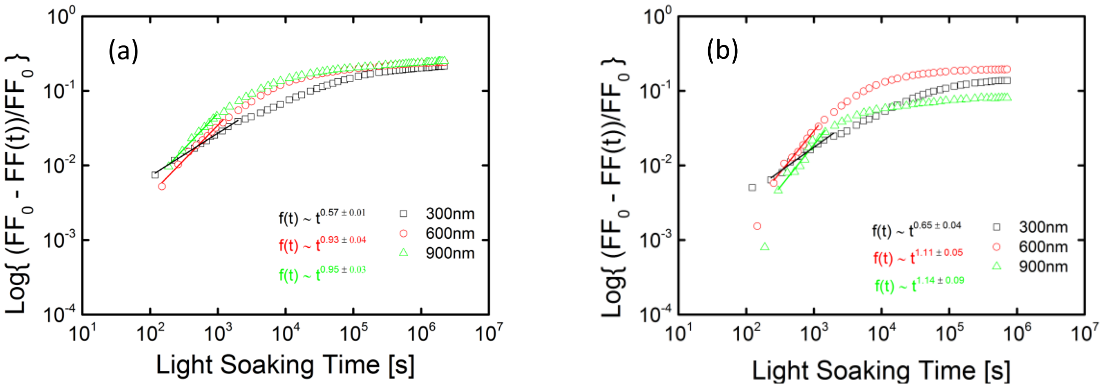

FIGURE 5-11: Normalized, log-scaled fill factor plots cells of varying thicknesses degraded at $T = 25°C$ with a linear fit of the initial time period. Indicated in the plots are also the relations of fill factor with time. The plots show the fill factor evolution for (a) R_0-type material and (b) R_{20}-type material.

The fitting results of the time exponent are noted in TABLE 5-8 below. A distinct increase is noted in the time exponent as the hydrogen dilution ratio increases from 0 to 20. Thus, the initial, fast regime of the fill factor degradation appears to be quicker in the hydrogen diluted samples than in the undiluted samples. This is also consistent with the observations from the efficiency fittings discussed in the previous section. Moreover, the values of the time exponent as calculated for R_{20}-type cells also deviate from the commonly found values of 1/2 or 1/3 [26] [56]. Most importantly, however, is the fact that the time exponent is sensitive to the hydrogen dilution of the absorber layer material of the solar cell. This is another indication that fixed values of time exponents in the power law of solar cell degradation may not be a suitable model for the SWE.

Absorber Layer Thickness	x for R_0 − material	x for R_{20} − material
300 nm	0.57±0.01	0.65±0.04
600 nm	0.93±0.04	1.11±0.05
900 nm	0.95±0.03	1.14±0.09

TABLE 5-8: Time exponent value for the fitted region of the fill factor plots in FIGURE 5-11.

5.3.2 EQE

The external quantum efficiency plots, as shown below in FIGURE 5-12 reveal that, once more, the trends in solar cell performance are seemingly unclear and inconsistent when increasing the hydrogen dilution ratio of the absorber layer. FIGURE 5-12 presents the degraded EQE of a 900 nm solar cell for varying hydrogen dilution ratios, and for the two different degradation temperatures $T = 25°C$ and $T = 45°C$. In the case of a degradation temperature of $T = 25°C$, the increase in hydrogen dilution yields clear improvements in spectral response. Moreover, the EQE enhancement is mainly located in the lower wavelength region ($\lambda < 600$ nm). In terms of the EQE interpretation provided in this report, this may indicate a lowering of defect generation throughout the intrinsic layer. Consequently, the increased hydrogen dilution yields a more favorable environment for electron propagation after degradation. Meanwhile, the spectral response in the longer wavelength region remains more or less independent of the hydrogen dilution. This is yet another indication that hole propagation in the device is less affected by the type of defects generated in the device.

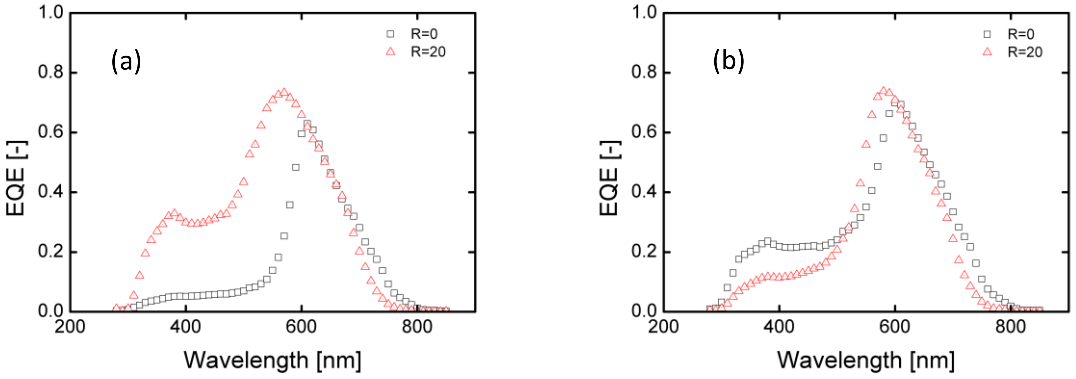

FIGURE 5-12: Degraded EQE for different hydrogen dilutions. The figures show the EQE results for degradation temperatures of (a) $\mathrm{T} = 25℃$, and (b) $\mathrm{T} = 45℃$.

At an increased degradation temperature of $\mathrm{T} = 45℃$, the EQE characteristics of both R_0 and R_{20} devices are altered, as seen in the figure above. As was noted in the previous section, the EQE of the R_{20} solar cell is worsened by the increase in degradation temperature. As such, the temperature increase has a positive effect for the R_{20} solar cell in spectral range under which it was degraded, i.e. at a wavelength of $\lambda = 630\ \mathrm{nm}$. Meanwhile, this is not the case for the entire spectral range, and will therefore most likely not be the case for efficiencies obtained under an AM1.5 spectrum. This will be investigated and discussed in the next chapter. Meanwhile, the R_0 solar cell EQE increases across the entire spectral range, as expected when higher thermal loads are imposed during degradation. We note that the spectral response of the two types of devices is similar in the long wavelength region. Meanwhile, the R_0 device EQE surpasses that of the R_{20} device for wavelengths shorter than 550 nm. The unexpected EQE results for the R_{20} device were originally believed to stem from the initial characteristics of the device. As noted in Chapter 4, there is reason to assume that the bandgap of the p-layer in the R_{20} devices is too low. Thereby, increased absorption in the blue part of the spectrum is inevitable, naturally leading to losses in spectral response. However, this cannot explain the EQE response of the R_{20}-samples at lower temperatures, where the degraded blue response is significantly better than for the R_0-sample. The peculiar temperature characteristics of the R_{20}-type devices will be further discussed in the next chapter.

Chapter 6: Thermal Annealing Characteristics of a-Si:H Solar Cells

In this chapter, the results from the thermal annealing process are presented and discussed for the different solar cell conditions which were explored throughout this project. As mentioned previously in this report, thermal annealing is considered the opposing process to defect creation within the amorphous material. As such, it is an integral part of the SWE, which results form an equilibration between these two processes. Much scientific attention has therefore been paid to annealing kinetics within a-Si:H solar cells, in order to gain a more profound understanding of light induced degradation [26] [44] [58]. The analysis of amorphous solar cell behavior presented in this report is therefore not complete without reviewing the thermal annealing kinetics. Employing the same form as the previous chapter, the effects of thickness, temperature, and hydrogen dilution on thermal annealing are presented here.

For the sake of consistency, the temperature of all thermal anneals which were carried out was fixed to $\mathrm{T} = 130°\mathrm{C}$. Moreover, all anneals were in the dark, in order to avoid effects of light soaking. Between annealing runs, the solar cells have been stored in the dark at room temperature. As this has shown to cause slight levels of annealing [59], this will be accounted for when discussing and analyzing the results in the following sections. The thermal anneals were carried out in intervals of varying durations, which increases with the total annealing time of the solar cells. Thus, the steep initial increase in solar cell performance, followed by a long-term stabilization, is well captured in the data. We note here that the results presented in this section are based on representative averages of up to 10 solar cells. These 10 samples are the same which were tracked throughout the degradation process, as discussed in the previous chapter. However, certain cells are omitted from the averages presented here, due to solar cell breakdown throughout the degradation process. The error bars seen in the plots represent three standard deviations within the group on which averages are based.

For the sake of comparison, the external parameter plots shown in this chapter are all normalized to the as-deposited average value of the solar cells in question. Initial external parameter values are found in previous chapters of this report. In all the external parameter plots found in this chapter, the first data point represents the degraded state of the solar cell, i.e. 0 hours of thermal annealing.

6.1 Effect of Thickness on Annealing

As was shown in the previous chapter, the thickness of the solar cell device under consideration affected the degradation considerably. It was shown that the increase in thickness did not only equate an increase in degradation, but also an alteration of the degradation kinetics of several external parameters of the solar cell. Consequently, the thickness dependency of the annealing process is probed in this section. Herein, the evolution of R_0 cells of two different intrinsic layer thicknesses, 300 nm and 900 nm, is tracked. The solar cells in question were degraded at a temperature of $\mathrm{T} = 25°\mathrm{C}$. The thinnest and the thickest devices are chosen to be presented in this section for the sake of a clear and effective demonstration of the thickness dependence. The plots corresponding to the intermediate intrinsic layer thickness, 600 nm, are found in Appendix B of this report.

6.1.1 External Parameters

In FIGURE 6-1, seen below, the evolution of external parameters under thermal annealing is shown for R_0 cells with intrinsic layers measuring 300 nm and 900 nm. After 20 hours of thermal annealing at $\mathrm{T} = 130°\mathrm{C}$, the efficiencies have recovered to a value of 90% or more for both intrinsic layer samples. Meanwhile, the evolution of the efficiency for the 300 nm intrinsic layer device remains relatively stagnant after 2.5 hours of thermal annealing. It is therefore assumed that some permanent damage has been inferred on the solar cells.

Meanwhile, the 900 nm intrinsic layer efficiency shows continued annealing effects throughout the entire 20 hours shown in the figures above. The same is true for the J_{SC} and the fill factor of the solar cells. Meanwhile, the final J_{SC}, fill factor, and efficiency of the 900 nm intrinsic layer cells is the same as that of the 300 nm intrinsic layer samples after 2.5 hours of annealing. By the shape of the annealing curves of these external parameters, it is clear that the 900 nm devices are stabilizing after about 20 hours of annealing. The 300 nm sample, on the other hand, entered this stabilization phase after 2.5 hours of annealing. It is expected that the characteristics of the 900 nm sample which pursue 20 hours of annealing resemble those of the 300 nm after 2.5 hours.

In both cells, however, a rapid initial recovery is seen in all external parameters, after one hour of annealing. The 300 nm intrinsic layer samples regain 15% of their initial fill factor, while the 900 nm intrinsic layer samples regain 23%. In terms of efficiency, the gain for 300 nm and 900 nm intrinsic layers samples is 12% and 40%, respectively. The gain in J_{SC} for the 300 nm and 900 nm intrinsic layer samples is 8% and 40%, respectively. In all cases, this initial increase represents far more than what is recovered during the remaining hours of annealing. In literature, the degradation of solar cells is often considered as a creation of defects in two different regimes: fast defect creation and slow defect creation [26] [58]. The annealing results presented here imply that the same principle applies in defect removal. This may be interpreted as two different types of metastable – those which have lower annealing energies, henceforth referred to as soft, and those which have higher annealing energies, henceforth referred to as hard. The results presented in FIGURE 6-1 implies that larger numbers of both soft and hard defects are generated in the thicker sample. Moreover, the plots suggest that a larger proportion of LID stems from soft defects in the thicker devices compared to the thinner samples.

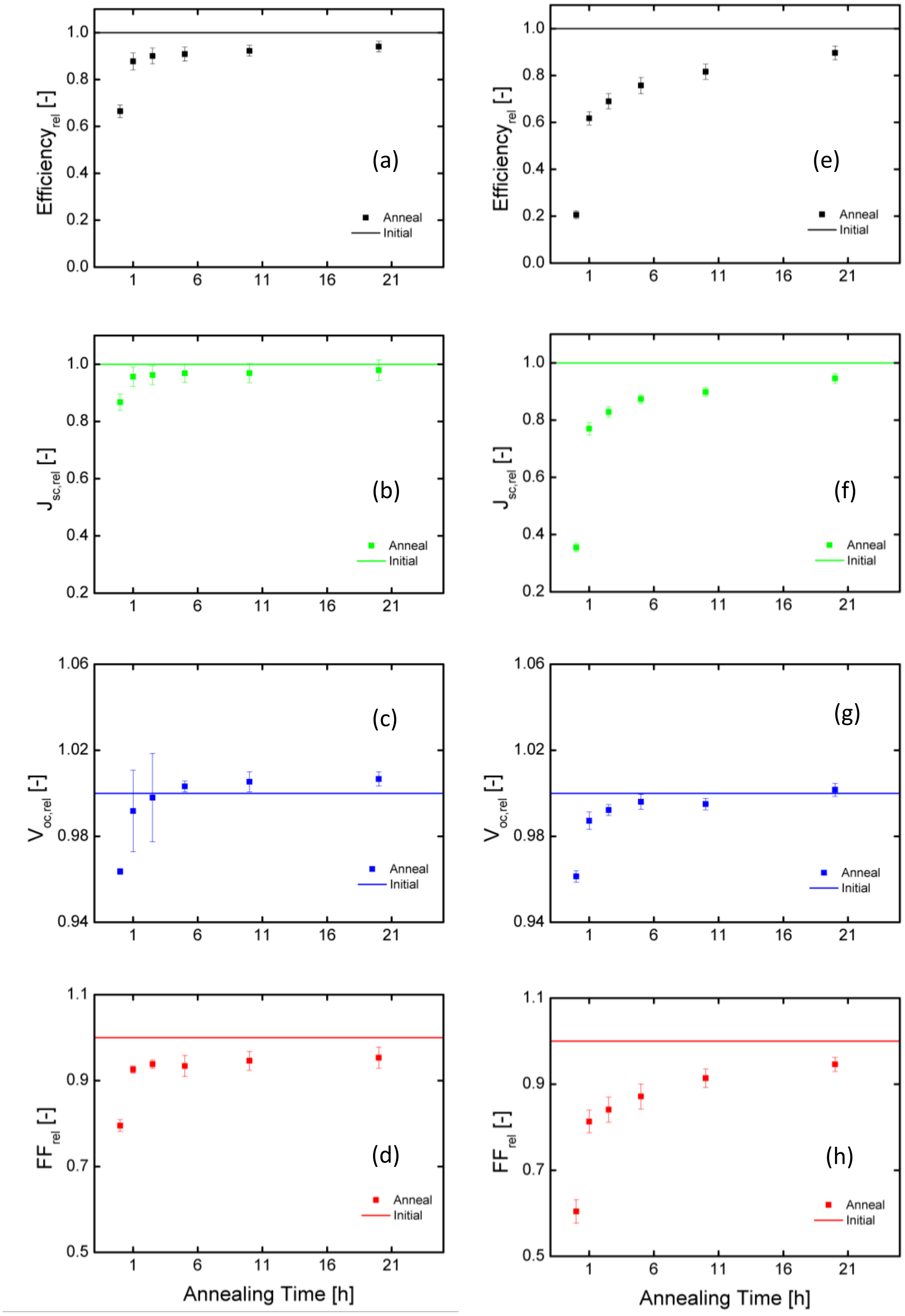

FIGURE 6-1: Relative annealing evolution of R_0 solar cells' external parameters. The solar cells were degraded at $T = 25°C$. The external parameter evolution is shown for cells of (a)–(d) 300 nm intrinsic layer thickness, and (e)–(h) 900 nm intrinsic layer thickness.

Finally, FIGURE 6-1 reveals that the V_{OC} recovery of the samples is seemingly thickness independent. The initial performance increase during the first hour of annealing, as well as the pursuing enhancement, in open circuit voltage is the same for the two intrinsic layer thicknesses. In the previous chapter, it was shown that the V_{OC} degradation was also largely thickness independent. In terms of the interpretation presented in the previous paragraph, the electric field within the device does not affect the type of defects in the material – soft or hard.

6.1.2 EQE

The external quantum efficiency evolution during thermal annealing offers a different view of the enhancement in J_{SC} as depicted in FIGURE 6-1. For the sake of clarity, only a few EQE plots are shown in FIGURE 6-2 below – the as-deposited EQE, the degraded EQE (0 hr), the EQE after one hour of annealing (1hr), and the EQE after 20 hours of annealing (20hr). As the EQE plots show, the first hour of annealing yields a significant increase in quantum efficiency for the entire spectral range. The spectral range where the initial EQE increase is the greatest, however, is within the shorter wavelength region ($\lambda < 600\ \mathrm{nm}$). As seen in the previous chapter, as well as the figure below, this is also where the largest degradation occurs during light soaking. Moreover, it is clear that the EQE of the 300 nm intrinsic layer sample is completely recovered after 20 hours of annealing, whereas the 900 nm intrinsic layer solar cell still has a deficient EQE in the shorter wavelength region.

The relative recovery in EQE is greater in the shorter wavelength region than in the longer wavelength region. However, the quantum efficiency of the device, independent of intrinsic layer thickness, approaches the initial levels in the longer wavelength region after one hour of annealing.

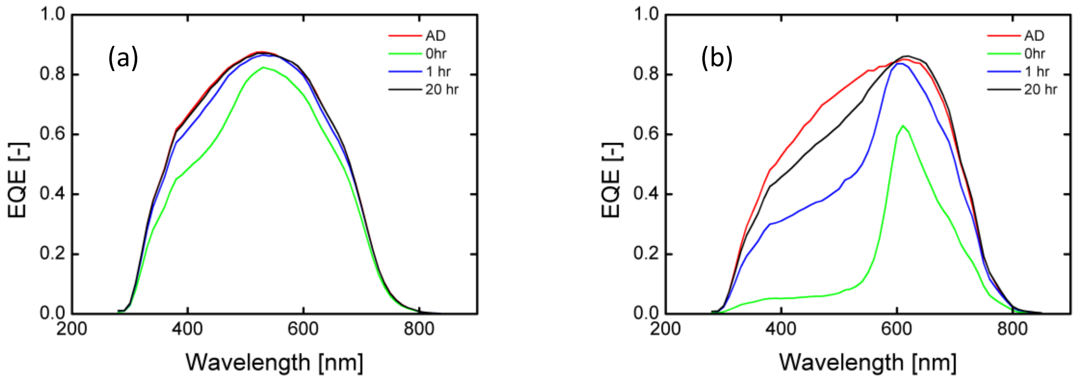

FIGURE 6-2: EQE evolution of R_0 solar cells. The solar cells were degraded at $\mathrm{T} = 25°\mathrm{C}$. The EQE evolution is shown for a (a) 300 nm intrinsic layer cell, and (b) 900 nm intrinsic layer cell.

Moreover, the EQE in the longer wavelength region of the thickest device surpasses that of the thinner one after one hour of annealing, as well as after subsequent anneals. In other words, despite a significantly degraded spectral response in the blue region, the 900 nm absorber layer solar cell's EQE for longer wavelengths still surpasses that of the 300 nm sample. This indicates that collection of charge carriers generated deep within, or even at the bottom of the intrinsic layer is more efficient than collection of charge carriers generated at the top of the intrinsic layer. As such, this is consistent with the interpretation that electrons generated near the p-i interface region are subject to larger propagation obstacles than holes generated close to the i-n interface. It should be underlined that the larger EQE at longer wavelengths for thicker devices is also caused by the mere fact that a larger number of electron hole pairs are generated.

6.2 Effect of Degradation Temperature on Annealing

In this section, the annealing results of solar cells which were degraded at different temperatures are compiled, presented, and compared. As discussed in the previous chapter, increased degradation temperatures will lead to a shift in the equilibrium between light induced defect creation and defect removal via thermal annealing. Therefore, light soaking at higher temperatures will inevitably yield cells which perform better in the degraded state. The point of investigation in this section is how this degraded performance, which stems from the choice of degradation temperature, will affect the annealing process. To this end, solar cell annealing characteristics are compared for two different temperatures, $\mathrm{T} = 25°\mathrm{C}$ and $\mathrm{T} = 45°\mathrm{C}$. As pointed out in the previous chapter, the temperature dependence of SWE characteristics is more visible in the thicker devices. For this reason, the comparisons presented here are carried out for solar cells of 900 nm intrinsic layer thickness. In order to provide a more nuanced view of how degradation temperature impacts the solar cells under thermal annealing, one set of R_0 cells and one set of R_{20}-cells are discussed in this section.

6.2.1 External Parameters

The external parameter evolution under thermal annealing of 900 nm intrinsic layer R_0 type solar cells are compared in FIGURE 6-3, below. The difference between the samples compared is the temperature at which they were degraded, as discussed in the previous chapter. Therefore, as seen in FIGURE 6-3, the *degraded* state of the cells degraded at $\mathrm{T} = 45°\mathrm{C}$ is significantly improved with respect to that of the cells degraded at $\mathrm{T} = 25°\mathrm{C}$. Meanwhile, this is the only difference in the external parameter evolution between the two samples. The rapid initial increase in performance within the first hour of annealing is present in both cases; however, this initial hour of exposure to temperatures of $\mathrm{T} = 130°\mathrm{C}$ leaves the performance at exactly the same level for the two sample devices. Moreover, after the first hour of thermal treatment, subsequent anneals lead to the same performance levels in the two solar cells.

Thus, for two devices degraded at different temperatures, the difference in the relative increase during the first hour of annealing is equal to the difference in performance level in the degraded state. This is another implication of the existence of two types of defects in the material after LID – soft and hard. As discussed in the previous section, the initial increase in solar cell performance probes the softer defects, which are the easiest to anneal. Due to the elevated degradation temperature of the R_0 device for which the external parameters are depicted in FIGURE 6-3(e)-(d), it is probable that a portion of the softer defects are annealed out during degradation. As previously noted, increasing the degradation temperature shifts the equilibrium between defect creation and defect annealing in the amorphous material. The results presented in this section imply that this shift in equilibrium is consistent with the removal of softer defects in the material, whereas the hard defects remain unaffected.

FIGURE 6-4, as seen below, depicts the same external parameter comparison as in FIGURE 6-3 for R_{20} samples which were degraded at $\mathrm{T} = 25°\mathrm{C}$ and $\mathrm{T} = 45°\mathrm{C}$. It is clear that the solar cells degraded at higher temperatures have a *lower* degraded efficiency than the solar cells degraded at lower temperatures. As discussed in the previous chapter, this is not a discrepancy of the measurement, even if the degradation curves seen in FIGURE 5-5 showed higher stabilized efficiencies for higher degradation temperatures. The EQE curves of the degraded state of the R_{20} solar cells revealed increased degradation temperatures yielded improved EQE in the spectral range under which the degradation was carried out and monitored. Meanwhile, the increase in temperature had a negative effect in the lower wavelength region ($\lambda < 600\ \mathrm{nm}$) of the R_{20} solar cells. As was predicted in the previous chapter, this is reflected in the AM1.5 efficiency of the solar cells, which is seen in the FIGURE 6-4 (a) and (e) below.

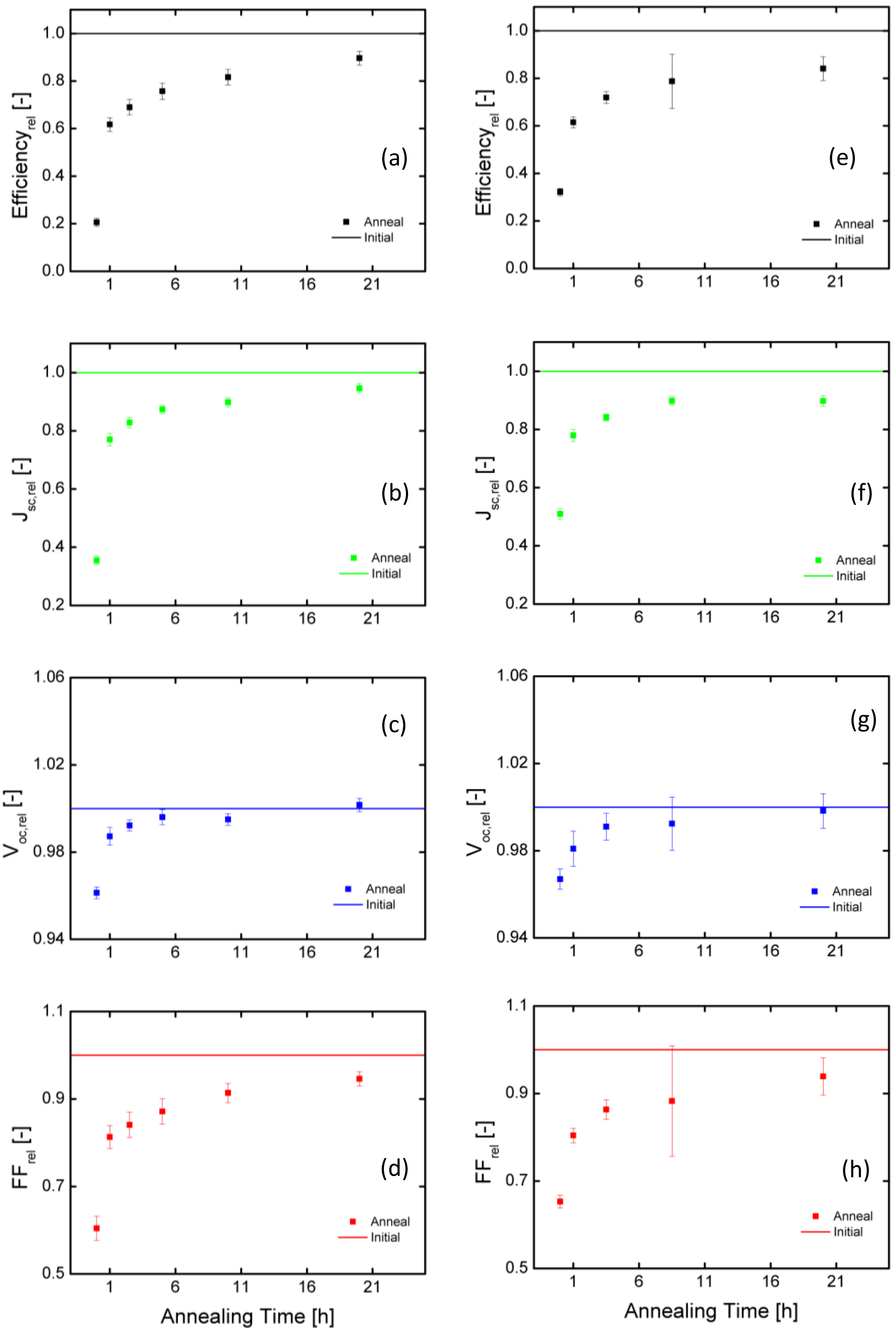

FIGURE 6-3: Relative annealing evolution of R_0 solar cells' external parameters for samples of 900 nm intrinsic layer thickness. The external parameter evolution is shown for cells degraded at (a) – (d) $T = 25°C$, and (e) – (h) $T = 45°C$.

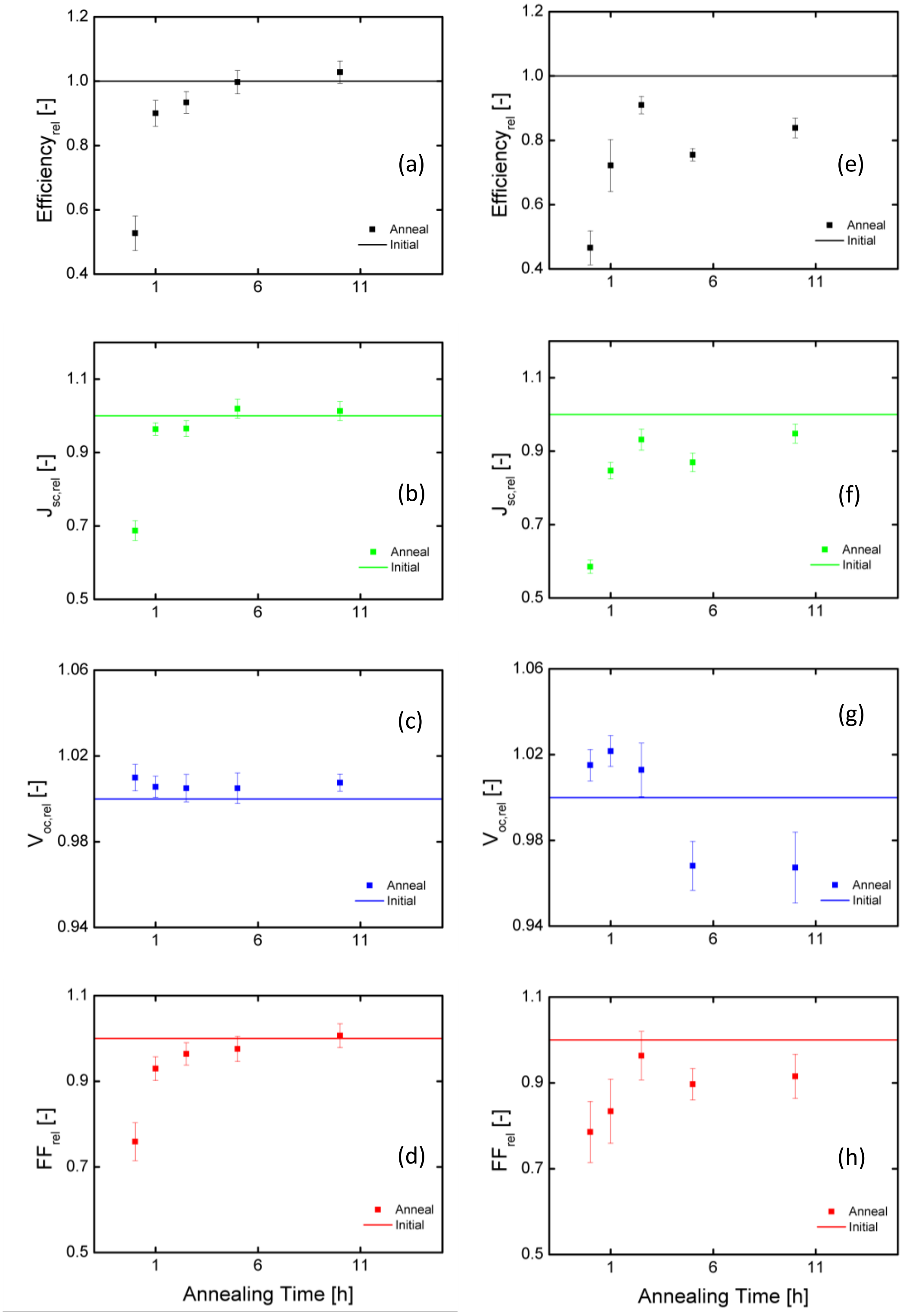

FIGURE 6-4: Relative annealing evolution of R_{20} solar cells' external parameters for samples of 900 nm intrinsic layer thickness. The external parameter evolution is shown for cells degraded at (a) – (d) $T = 25°C$, and (e) – (h) $T = 45°C$.

The external parameters of the R_{20} samples also show significant alterations in annealing pattern as the temperature at which they were degraded increases. While the samples degraded at $T = 25°C$ demonstrate continuous enhancement in solar cell external parameters as a function of annealing time, the samples degraded at $T = 45°C$ do not reproduce this behavior. Rather, fluctuations in solar cell parameters are observed after 2.5 hours of annealing. The solar cell efficiency sees a decrease of

10% of its initial value between 2.5 hours of annealing and 5 hours of annealing. During the subsequent 5 hours of annealing, a 5% efficiency increase is observed, leaving the final performance level of the solar cell at a lower stage than after 2.5 hours of annealing. Moreover, and in contrast to the annealing characteristics of the R_{20} cells which were degraded at $\mathrm{T} = 25°\mathrm{C}$, the solar cells which were degraded at a higher temperature do not recover their initial performance. The decrease in solar cell efficiency after 2.5 hours of annealing coincides with a sudden dip in V_{OC}. Although the relative alterations are minor, this sudden drop is seemingly mirrored in the other external parameters, and in particular the fill factor. Although the kinetics of annealing are difficult to interpret here, we note the negative influence of degradation temperature increase on the degraded state and the annealed state under STC.

6.2.2 EQE

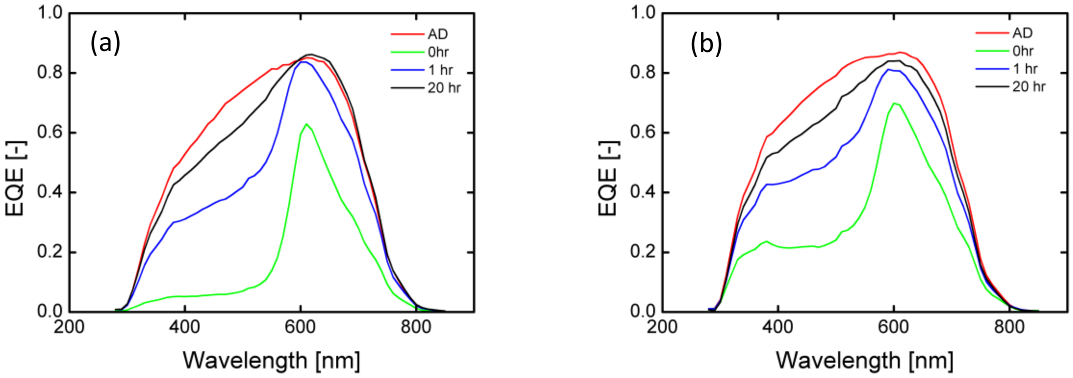

FIGURE 6-5: EQE evolution of 900 nm intrinsic layer R_0 solar cells. The solar cells were degraded at (a) $\mathrm{T} = 25°\mathrm{C}$. and (b) $\mathrm{T} = 45°\mathrm{C}$

The quantum efficiency evolution of 900 nm intrinsic layer solar cells is plotted for R_0 samples and R_{20} samples in FIGURE 6-5 and FIGURE 6-6, respectively. In each figure, the EQE evolution is compared for two samples which were degraded at different temperatures. In the case of R_0 samples, the degradation temperature increase causes distinct improvement across the entire spectral range in the degraded state. As seen in the external parameter discussion in the previous section, the first hour of thermal annealing yields the same integrated spectral response, i.e. J_{SC}, independent of the temperature at which the samples were degraded. This is demonstrated in FIGURE 6-5 by the surface area under the EQE after one hour of annealing, which is equal for both samples. The EQE evolution due to further annealing is also similar, and both devices show more or less full recovery in the longer wavelength region $(\lambda > 600\ \mathrm{nm})$ after 20 hours of annealing. Thus, the degradation temperature of the R_0 solar cells does not impact the annealing characteristics of the solar cells.

The R_{20} solar cell EQE, as depicted in FIGURE 6-6 below, indicate a dependence on the thermal treatment during degradation. Not only is the degraded EQE of the solar cell considerably altered for wavelengths less than 500 nm, but the final level of recuperation in EQE also varies with the degradation temperature. It is important to stress the fact that performance in the spectral region for which LID was carried out and monitored, i.e. at $\lambda = 630\ \mathrm{nm}$, is actually enhanced as degradation temperature increases. Moreover, EQE in longer spectral regions is more or less fully recovered after one hour of annealing, independent of degradation temperature.

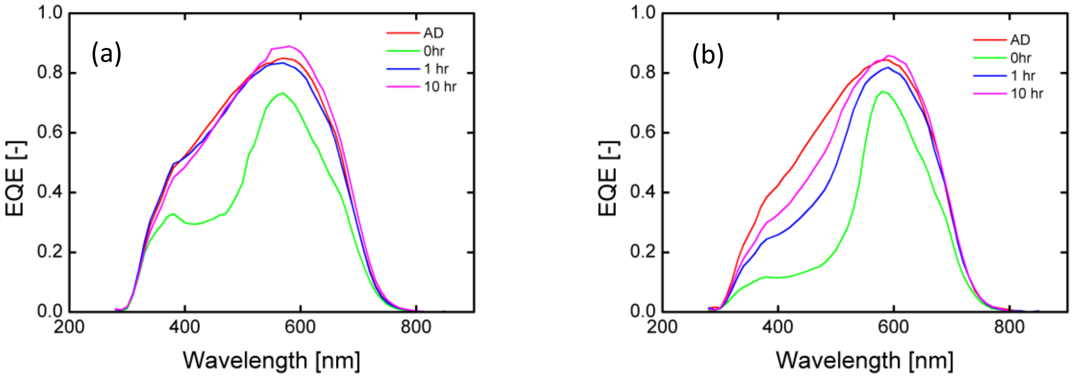

FIGURE 6-6: EQE evolution of 900 nm intrinsic layer R_{20} solar cells. The solar cells were degraded at (a)$\mathrm{T} = 25℃$. and (b) $\mathrm{T} = 45℃$

6.3 Effect of Hydrogen Dilution on Annealing

In this section, the role of hydrogen dilution in the thermal annealing characteristics of a-Si:H will be investigated and discussed. The inherent material structure of the hydrogen diluted material is more stable and structured than its undiluted counterpart. This material characteristic is associated with a higher resistance to defect creation, and thus, the SWE. The point of investigation in this section is whether or not these very material characteristics impact how efficiently defects can be removed once generated and located within the amorphous material.

In the previous section, the effect of temperature on annealing kinetics for both R_0 and R_{20} devices was presented and discussed. Therefore, the results treated in this section relate to the differences in annealing due to hydrogen dilution at one specific temperature. The temperature of standard test conditions, i.e. $T = 25°C$, has been chosen to this end. STC conditions are presented as a point of reference for the sake of ease of comparison. Furthermore, all results presented in this section pertain to solar cells with an intrinsic layer thickness of 900 nm.

6.3.1 External Parameters

The external parameters of 900 nm intrinsic layer solar cells are compared in FIGURE 6-7 below for R_0-type material and R_{20}-type material. The efficiency evolution due to thermal annealing displays similar trends for both material types. More precisely, the relative efficiency evolution as a function of annealing time is more or less identical, apart from a translational shift in efficiency values due to different starting points. Indeed, the initial increase in efficiency during the first hour of annealing reaches 40% percent of the initial value in both cases. The R_{20} efficiency does not stabilize as it approaches its initial value, but continues to increase with consequent anneals. After a total of 5 hours of annealing, the R_{20} efficiency is back to its initial value. Meanwhile, the R_0 efficiency at this point in time is at about 75% of its initial value, meaning that the initial gap in relative degraded values of 25% - 30% persists throughout the annealing process. Similar tendencies exist for J_{SC} and fill factor of the solar cells. Eventually, this leads to a solar cell performance level in the R_{20} device which surpasses its initial value within 10 hours of thermal annealing. The similarity in annealing characteristics of the external parameters, independent of hydrogen dilution ratios, indicates the existence of soft and hard defects in both material types. Meanwhile, the initial performance in the R_{20} material is rapidly approached in the first annealing step, which may imply that the R_{20} has a better resistance to light induced creation of hard defects than the R_0-type material. Additionally, the fact that the annealing in R_{20} samples leads to higher performance levels than the initial starting point of the solar cell may indicate that there are less hard defects in the R_{20} material even in the as-deposited state.

By observing the V_{OC} annealing characteristics of the R_{20} solar cell in FIGURE 6-7(g), it can be seen that it differs significantly from that of the R_0-type devices, and that it remains almost constant. Moreover, the R_{20} V_{OC} maintains a value which is slightly larger than its as-deposited level for the entire annealing sequence. This is a manifestation of a larger built-in electric field in the device, which ultimately will play a role in the annealing evolution. Previous studies have shown that annealing at reverse bias improves the recovery of initial solar cell parameters [60]. Essentially, an elevated built-in potential may have the same effect, and it is plausible that this characteristic yields more favorable conditions for defect removal in the R_{20} material, which, as can be seen in FIGURE 5-9(g), has a V_{OC} that does not degrade during light soaking.

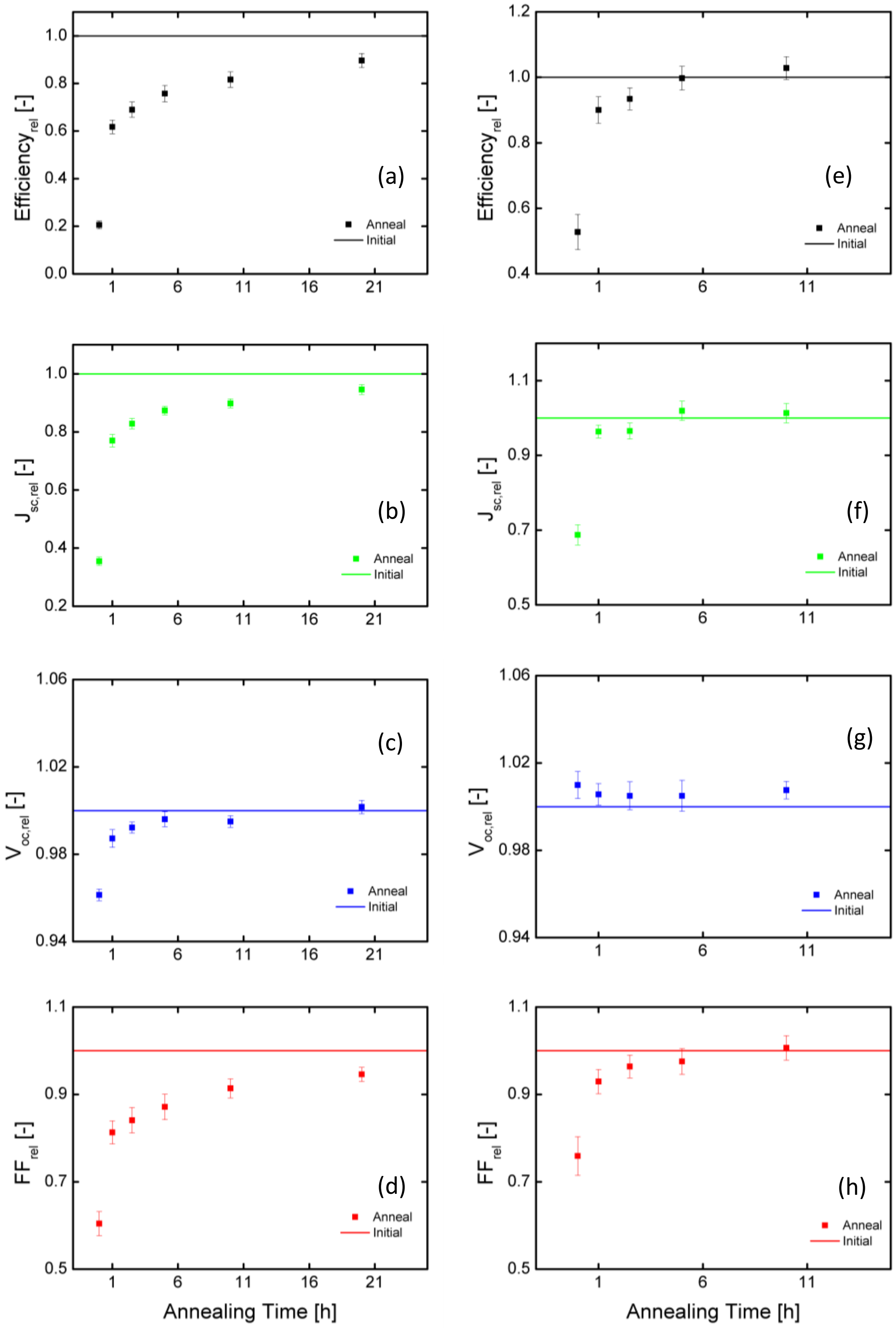

FIGURE 6-7: Relative annealing evolution of solar cells of 900 nm intrinsic layer thickness degraded at $\mathrm{T} = 25^{\circ}\mathrm{C}$. The external parameter evolution is shown for cells of hydrogen dilution ratio (a) R_0 and (b) R_{20}.

6.3.2 EQE

FIGURE 6-8, as seen below, depicts the evolution in EQE for R_0 and R_{20} solar cells degraded at $\mathrm{T} = 25^{\circ}\mathrm{C}$, and with an intrinsic layer thickness measuring 900 nm. As pointed out and discussed in the previous chapter, the degraded state performance of the R_{20}-type exceeds that of the R_0-type solar cells. As seen in the external parameter evolution presented in the previous sub-section, the most drastic increase in performance occurs during the first hour of annealing, and the R_{20} performance after 10 hours of annealing surpasses its initial points. This is well demonstrated in the EQE plots below.

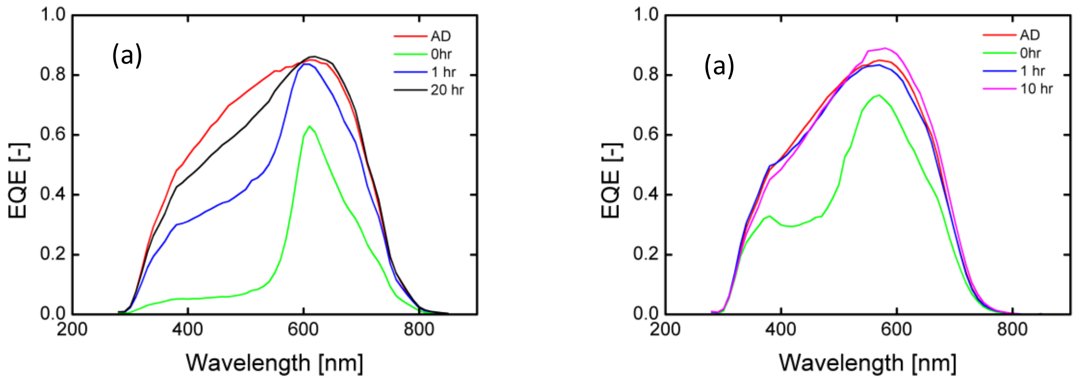

FIGURE 6-8: EQE evolution of 900 nm intrinsic layer solar cells degraded at $T = 25°C$. The solar cells have hydrogen dilution ratios of (a) R_0 and (b) R_{20}

In R_0-type material, the initial value of spectral response in the longer wavelength regions ($\lambda > 600\ \mathrm{nm}$) is recovered completely, while the EQE in the lower wavelength region remains deficient. Meanwhile, the R_{20}-type device recovers completely within the first hour of thermal annealing. This is in line with the interpretation that more soft defects are generated in the R_0 material than in the R_{20} material, as discussed in the previous section. Moreover, the full recovery of R_{20} EQE as presented in FIGURE 6-8 may also indicate that this material type prevents the generation of hard defects, as opposed to its undiluted counterpart. Due to the fact that the permanent degradation in the R_0 devices is associated with the presence of hard defects, this implies that the hard defects cause a drop in shorter wavelength spectral response.

Meanwhile, it is evident from the degraded state EQE that the defects considered herein as soft also impact the shorter wavelength spectral response to a larger extent than the longer wavelength region. Thus, charge carriers generated as a result of illumination at longer wavelength are more easily collected than those generated by short-wavelength photons in the presence of light induced defects, regardless of whether they are soft or hard. Once again, this may be interpreted in terms of hole and electron propagation in the material, and thus evoke the possibility that hole collection in the amorphous material is less affected by its inherent defect-rich environment than electron diffusion. Furthermore, the results presented here indicate that this is the case for both soft and hard defects.

6.4 Dark IV Measurements of Degraded and Annealed Samples

Because the amorphous material is prone to thermal annealing, as was thoroughly discussed in this chapter, and prone to thermal annealing, monitoring a temperature-dependent characteristic after degradation is not straightforward. In order to obtain a state of the solar cells in which such a measurement is feasible without altering the properties of the material, the cells were annealed for some time after degradation before performing the measurement. Thus, a state of stability was imposed which allowed for measuring the dark current-voltage characteristics of the solar cells. In this section, the dark IV results after degradation and a given annealing time will be presented for R_0-type material and R_{20}-type material. The results are discussed with respect to the as-deposited dark IV-characteristics. The dark IV results shown in this section pertain to solar cells degraded at $\mathrm{T} = 45°\mathrm{C}$.

Throughout the data processing of the collected data, it became clear that the thinner cells were more prone to discrepancies and perturbations in the dark IV measurements. Ambiguous measurement results for the 600 nm and 300 nm samples were obtained, which made it impossible to associate a trend or discussion to these in this section. However, the measurements showed clear tendencies of increased discrepancies and perturbations as the bias voltage decreased. Lowering the forward bias voltage or increasing negative bias voltages is equivalent to a stronger internal electric field in the device. The effects of this are expected to be more strongly felt in the thinner devices, as the electric fields herein are the largest. Alterations in recombination current through emissions caused by potential barrier lowering, i.e. the Poole-Frenkel Effect, are expected to be most dominant in thinner devices [61]. Therefore, this is presented as a possible explanation of the unambiguous and peculiar dark IV measurements of thinner devices. For this reason, only the dark IV measurement results of the 900 nm samples are presented and discussed here.

6.4.1 R_0-Type Material

The 900 nm intrinsic layer R_0-type sample was annealed for 20 hours at $\mathrm{T} = 130°\mathrm{C}$ after degradation before a new dark IV measurement was made. As is visible from FIGURE 6-3, the solar cell performance is not entirely recovered, but is at a point in its annealing progress where exposure to higher temperatures for shorter periods does not have a large effect. FIGURE 6-9 below shows the comparison between as-deposited and the annealed dark IV for two different temperatures, $\mathrm{T} = 40°\mathrm{C}$ and $\mathrm{T} = 80°\mathrm{C}$.

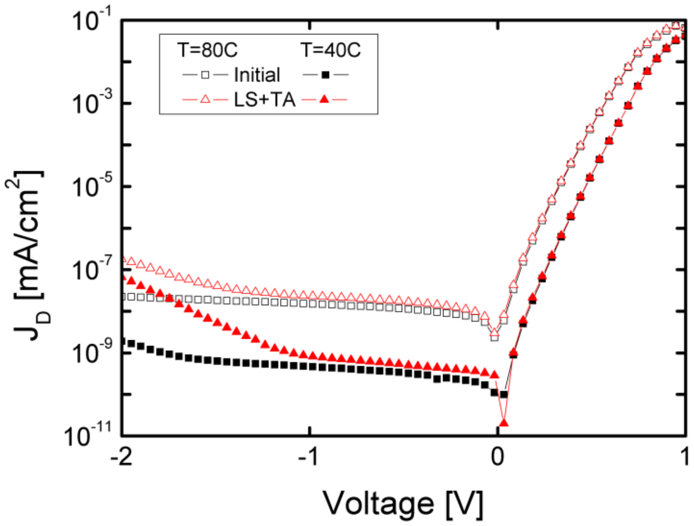

FIGURE 6-9: Dark IV measurement of an R_0-type 900 nm intrinsic layer solar cell in its as-deposited (Initial) and annealed (LS+TA) state for two different temperatures. The solar cell was degraded at $\mathrm{T} = 45$°C for 200 hours followed by 20 hours of thermal annealing at $\mathrm{T} = 45$°C .

The plot in FIGURE 6-9 reveals no significant difference in dark current for small forward bias voltages. The change in dark current is more evident as the reverse bias grows stronger. According to the interpretation of dark current, this is consistent with the Poole-Frenkel effect as mentioned earlier in this section. As the bias voltage is decreased, the electric field in the device is enhanced, and may result in a barrier lowering for charge emission from trap states in the sub-band gap region. This, in turn, may result in increased dark current.

Thermal Activation Energy of Recombination

Consequently, the activation energy of recombination of the device is calculated according to equation Eq. 2-10, as presented in Chapter 2 of this report. FIGURE 6-10 below displays the activation energy of the device in its as-deposited state, and after LID and thermal annealing. The plots show the activation energy for both forward and reverse bias voltages.

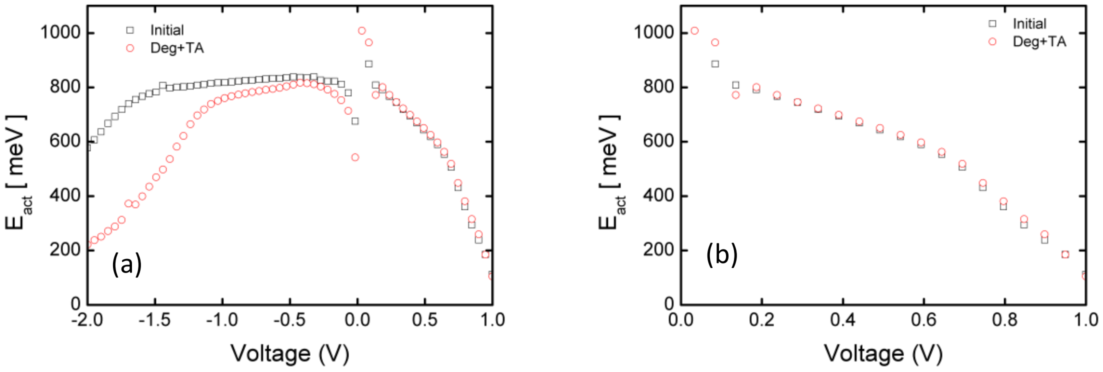

FIGURE 6-10: Activation energy of a R_0-type 900 nm intrinsic layer solar cell in its as-deposited state (initial) and degraded and annealed state (Deg+TA). The sample was degraded for 200 hours at $\mathrm{T} = 45$°C, and subsequently annealed for 20 hours at $\mathrm{T} = 130$°C. The figure shows the activation energy for (a) the full voltage range, and (b) only forward bias voltages.

The voltage dependent activation energy of the dark current, as shown in FIGURE 6-10, is seemingly identical for initial and the degraded/annealed state in the forward bias voltage range. The method proposed by Pieters *et al*., as cited in Chapter 2 of this report, is employed in order to obtain the mobility band gap, E_{mob}, and the thermal ideality factor, m_{th}, of the intrinsic layer of the solar cell before and after degradation. As the mobility band gap and thermal ideality factor of the R_0-material as presented in Chapter 4 are based on an average of data points associated with three different samples, these are recalculated for the 900 nm sample only for the sake of comparison. Eq. 2-11 yields $m_{th,init} = 2.00$ and $E_{mob,init} = 1.61\text{ eV}$ for the as-deposited state of sample, and $m_{th,deg+TA} = 2.09$ and $E_{mob,deg+TA} = 1.65\text{ eV}$ for the degraded and annealed state of the sample. Thus, the value of the thermal ideality factor is still consistent with the theory presented by Pieters *et al.* The thermal activation energy yields a mobility bandgap for the degraded and annealed state which is practically equal to that of the initial state.

The reverse bias voltage range shown in FIGURE 6-10(a), however, reveals a strong decrease in activation energy with increased internal electric field (i.e. reduced bias voltage) in the degraded/annealed state. This is consistent with the Poole-Frenkel effect, which may be seen as a lowering of the activation energy of the recombination current in the device.

Ideality Factor

The ideality factor, defined in Eq. 2-9 and plotted in FIGURE 6-11 reveals the recovery of the dark current-voltage characteristics in the forward bias voltage range of the R_0-type solar cell after annealing. Once again, we note from FIGURE 6-3 of this chapter that degradation effects are still visible through the external parameters of the device. Meanwhile, this is not visible in the ideality factor figures presented in this section. As discussed in previous sections, the ideality factor is interpreted as a manifestation of the energetic spread of the defects in the band gap. More specifically, the ideality factor is often considered a probe of the p-i interface. Hence, the equal ideality factors, as seen in the figure below, combined with the visible degradation effects in the solar cell's external parameters, may imply that the remaining defects in the material are not probed by the ideality factor due to their energetic distribution within the bandgap.

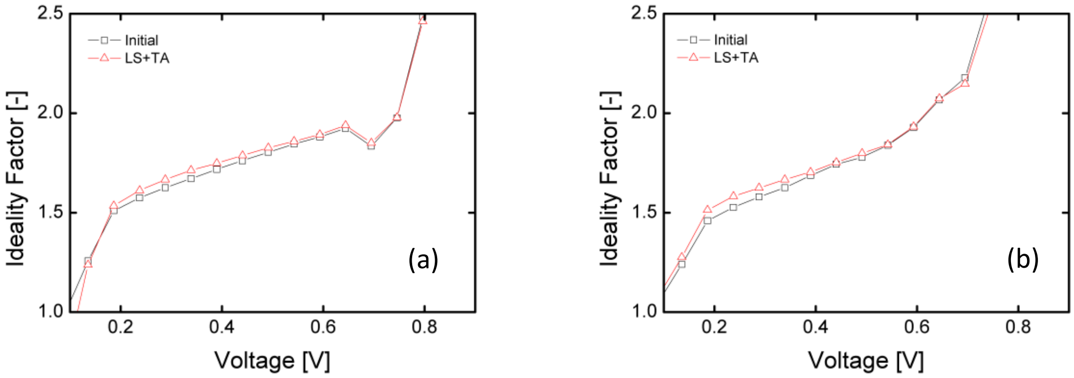

FIGURE 6-11: Voltage-dependent ideality factor of a 900 nm intrinsic layer R_0-type solar cell. The plots show the ideality factor in the as-deposited state (initial) and the degraded and annealed state (LS+TA). Shown here is the ideality factor at (a) $\mathrm{T} = 40℃$, and (b) $\mathrm{T} = 80℃$.

6.4.2 R_{20}-Type Material

FIGURE 6-12 below shows the dark current-voltage characteristics of a 900 nm intrinsic layer R_{20}-type solar cell for different temperatures. The dark IV is plotted in the same way as for the R_0-type material, showing the initial state of the device, as well as the degraded and annealed state of the device.

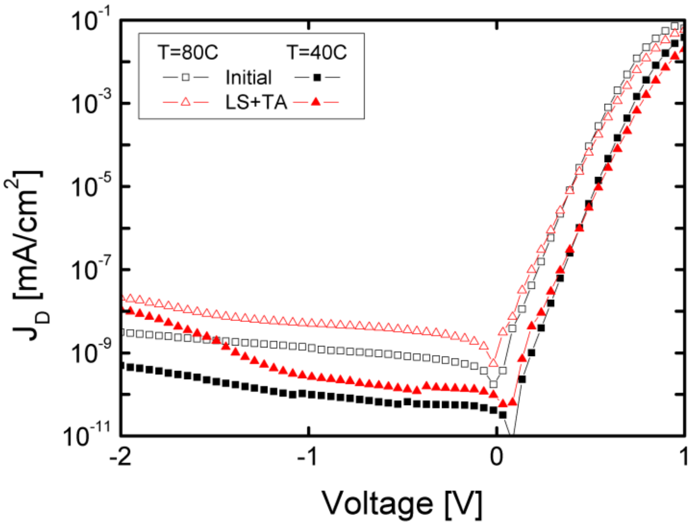

FIGURE 6-12: Dark IV measurement of an R_{20}-type 900 nm intrinsic layer solar cell in its as-deposited (Initial) and annealed (LS+TA) state for two different temperatures. The solar cell was degraded at $\mathrm{T} = 45°\mathrm{C}$ for 132 hours followed by 1 hour of thermal annealing at $\mathrm{T} = 45°\mathrm{C}$.

The device was degraded for 132 hours at $\mathrm{T} = 45°\mathrm{C}$, and annealed for 1 hour at $\mathrm{T} = 130°\mathrm{C}$. In the case of the R_{20}-type devices, it was decided to perform the dark IV measurement after merely one hour of annealing due to the rapid rate with which these solar cells approached their initial performance levels. Thereby, it was considered that a degraded state which was stable enough for a temperature-dependent measurement was obtained after a one hour anneal.

The plot reveals a distinct increase in dark current for forward bias voltages lower than 0.6 V for the degraded/annealed state of the solar cell. This implies higher rates of SRH recombination, as discussed in Chapter 4 of this report. Moreover, the increase in the observed bending of the dark IV curve observed at higher forward bias voltages is indicative of increased series resistance in the degraded solar cell as compared to the initial state. This is consistent with series resistance measurements throughout degradation. Finally, the strong increase in dark current for reverse bias voltages is observed for the degraded state of the device with respect to the initial state. Once again, this is interpreted in terms of the Poole-Frenkel effect, and as such, may serve as another indication of increased defect density in the bandgap of the intrinsic layer material.

Thermal Activation Energy of Recombination

Consequently, the thermal activation energy of recombination is re-calculated for the R_{20}-type device according to Eq. 2-10. FIGURE 6-13 below shows the thermal activation energy plots for forward and reverse bias for the 900 nm intrinsic layer R_{20} device before and after degradation.

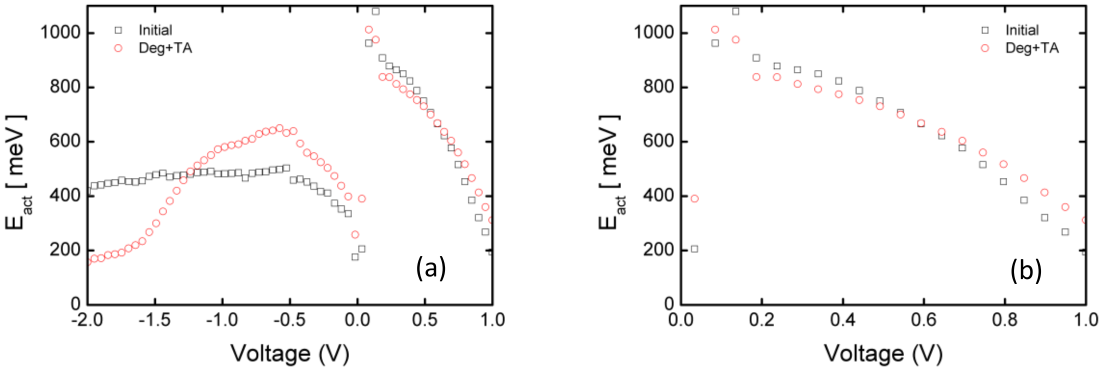

FIGURE 6-13: Activation energy of a R_{20}-type 900 nm intrinsic layer solar cell in its as-deposited state (initial) and degraded and annealed state (Deg+TA). The sample was degraded for 132 hours at $T = 45°C$, and subsequently annealed for 1 hours at $T = 130°C$. The figure shows the activation energy for (a) the full voltage range, and (b) only forward bias voltages.

The plots reveal that the activation energy of the R_{20}-type device is significantly altered after degradation and one hour of annealing. Moreover, the change in activation energy is visible in both the forward bias voltage range, and the reverse bias voltage range. For higher forward voltage bias, the activation energy of the degraded state is higher than that of the initial state. This likely due to the increase in series resistance effects, as noted in the previous section, which impose dissipative losses in the device. For lower values of forward bias voltage, however, the activation energy of recombination is reduced for the degraded state of the device. In reverse bias, the trend to which we associate the Poole-Frenkel effect is visible through a significant drop in activation energy at strong reverse bias voltage.

Subsequently, the mobility bandgap, E_{mob}, and thermal ideality factor, m_{th}, are calculated for the device in its initial and degraded state, using Eq. 2-11. The values found here are $E_{mob,initial} = 1.85\text{ eV}$ and $m_{th,initial} = 1.98$ for the initial state of the device, and $E_{mob,deg+TA} = 2.07\text{ eV}$ and $m_{th,deg+TA} = 2.5$ for the degraded and annealed state of the device. Thereby, it is found that the thermal ideality factor of the degraded state of the R_{20} material is inconsistent with the values reported previously in literature [14]. Hence, the calculated mobility bandgap for the degraded state of the device via the method proposed by Pieters *et al.* does not seem valid for this application.

Ideality Factor

The voltage-dependent ideality factor, as defined in Eq. 2-9, is shown in FIGURE 6-14 below for the as-deposited state and the degraded state of the R_{20}-type 900 nm intrinsic layer solar cell for two different temperatures. The plots reveal a distinct increase in the ideality factor across the entire voltage range shown here, which is associated with SRH recombination as noted earlier. The increase in ideality factor indicates a significant alteration in the spread of the defects in the device. As discussed in Chapter 2 of this report, the ideality factor represents the added defect density which can participate in the recombination current due to further splitting the quasi-Fermi energy levels of the trap states. According to this interpretation, the ideality factor results of the R_{20} samples, as shown below, may imply a defect distribution which is significantly altered in the p-i interface region. Therefore, the results presented in this section and seen in FIGURE 6-14 are either in contrast to the claim that defect creation in the device occurs throughout the bulk of the intrinsic layer, or that the ideality factor and dark IV measurement probe the p-i interface.

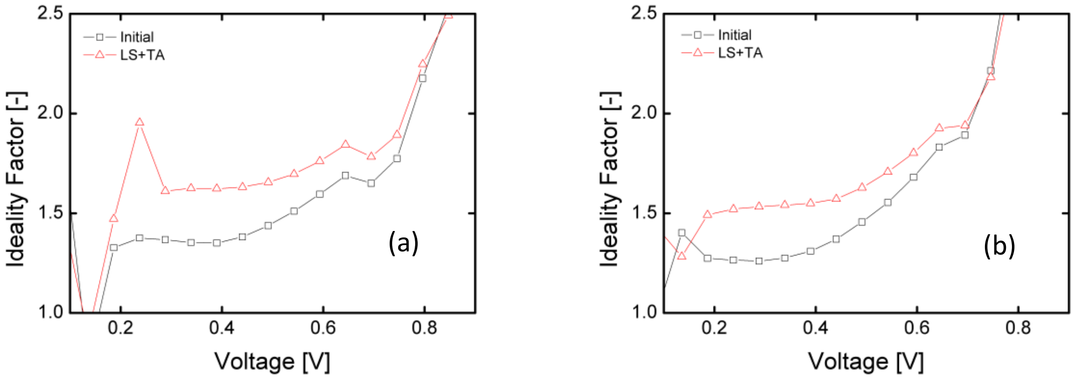

FIGURE 6-14: Voltage-dependent ideality factor of a 900 nm intrinsic layer R_{20}-type solar cell. The plots show the ideality factor in the as-deposited state (initial) and the degraded and annealed state (LS+TA). Shown here is the ideality factor at (a) $\mathrm{T} = 40$℃, and (b) $\mathrm{T} = 80$℃.

Chapter 7: Conclusions and Future Recommendations

In this chapter, the results and key points of analysis of this report are presented and summarized. Due to an extensive amount of experimental data, the reader is referred back to Chapters IV-VI for the detailed figures and discussion pertaining to the concluding remarks of this section. Moreover, some recommendations for future work and analysis will be presented herein.

7.1 Concluding Remarks

Conclusions from Initial Characterization

We have shown that the initial external parameters of hydrogenated amorphous silicon solar cells are dependent on absorber layer thickness, as well as hydrogen dilution in the intrinsic layer. Illuminated voltage-current characteristics indicate that in R_0-material, the initial V_{OC} and fill factor consistently decrease with intrinsic layer thickness, while initial efficiency and J_{SC} are maximized for an intrinsic layer thickness of 600 nm. Thereby, there exists an optimized equilibrium between initial absorption and recombination in the amorphous material, which is found for devices which are thicker than the standard solar cell. The illuminated voltage-current characteristics of R_{20} material indicate that it has a lower defect density than R_0 material, an increased bandgap, and presumably, a higher structural order. The thickness independence of the R_{20} material is also clear from the IV-measurements.

The thickness dependence of the initial external quantum efficiency of the devices indicates a tendency of reduced EQE in the blue part of the spectrum and increased EQE in the red part of the spectrum as thickness increases. This is interpreted in terms of carrier collection efficiency and spatial distribution of charge carrier generation. The trends presented in this report may imply that the hole propagation may not be the limiting factor in charge carrier collection in the a-Si:H material, but rather the electrons.

The results of dark voltage-current measurements imply that the dark IV and the voltage-dependent ideality factor are more or less thickness independent. This implies a distribution of native defects which is centered close to the p-i interface region. Moreover, the validity of mobility bandgap and thermal ideality factor calculation, as presented by Bart Pieters, is reinforced by the results obtained from dark IV measurements. The mobility bandgap of the R_0 material is found to be 1.63 eV.

The assumed reduction in defect density for material of increased hydrogen dilution is consistent with measurements of dark voltage-current characteristics. These measurements demonstrate the lower recombination current of the R_{20} devices compared with R_0 devices, which is interpreted in terms of a lower defect density. The ideality factor in the bias voltage range where SRH recombination is dominant also shows a distinct reduction with increased hydrogen dilution ratio, which also indicates a lowered defect density in the material. Moreover, the mobility bandgap of the R_{20} material is found to be 1.85 eV, indicating a significant increase with respect to the R_0 material.

This is indicative of higher order material structure, and a lower defect density. It is noted that Pieters' method of calculating the material mobility bandgap seems to be applicable to a-Si:H of non-zero hydrogen dilution ratios.

Conclusions from Degradation

In-situ measurements during degradation yield high-quality results, which are all the more reliable as they are well defined averages of five to ten solar cells. The experimental value of the well-controlled degradation setup adds to the gravity of the conclusions presented in this section.

The experimental results verify the thickness dependence of degradation and stabilized performance of hydrogenated amorphous silicon. Increased absorber layer thickness clearly results in lower stabilized performance, independent of hydrogen dilution ratio values. Meanwhile, the thickness dependences of the degradation patterns of the external parameters differ. The fill factor and V_{OC} degradation is independent of the intrinsic layer thickness. This trend in open circuit voltage degradation is interpreted as an indication that defect creation occurs deep within the device. Moreover, there seems to be an intrinsic layer thickness threshold between 300 nm and 600 nm, for which the degradation of the solar cell is significantly worsened. The 300 nm difference in intrinsic layer thickness between the 600 nm sample and the 900 nm sample, however, has little effect on the degradation characteristics of the solar cell. Fitting of efficiency degradation indicates that the thicker samples degrade more in a shorter time period. The fitting results also indicate higher total defect density in the thicker device after degradation.

The external quantum efficiency degradation is clearly thickness dependent. This dependence is clearly demonstrated for both hydrogen dilution ratios considered in this project. Moreover, the thickness dependence of the EQE degradation is consistent with previous findings and simulation results which indicate its origin as defect creation throughout the intrinsic layer. The degraded EQE measurements imply that these defects may pose larger barriers to electron propagation than hole propagation in the amorphous material.

We have shown that increased degradation temperatures cause higher stabilized performance under illumination of wavelength $\lambda = 630\ \mathrm{nm}$ for both R_0 and R_{20} material. Moreover, the degradation pattern of solar cell V_{OC} and fill factor are also shown to be independent of temperature. These two external parameters degrade in parallel, with different starting points based on temperature. Efficiency fittings reveal that the samples stabilize sooner at higher temperatures. Moreover, the fitted curves indicate that samples degraded at higher temperature show higher levels of degradation per unit time before they stabilize.

The study of hydrogen dilution impact on degradation kinetics shows that R_{20} devices consistently exhibit a significant reduction in relative degradation compared to R_0 solar cells. This is consistent with previous reports in literature. The fitted efficiency curves showed that the hydrogen diluted samples stabilize earlier than the undiluted samples. Due to a well-controlled in-situ degradation measurement setup, it is clear that V_{OC} in R_{20} solar cells remains constant throughout the degradation process, and even increases at the end. This V_{OC} increase as a result of degradation is emphasized by increased degradation temperatures. On the other hand, in R_0-material, the V_{OC} degrades consistently for all temperatures and absorber layer thicknesses tested here.

Meanwhile, the degradation study showed that the R_{20} AM1.5 performance is reduced for higher degradation temperature. On the other hand, the performance under red light, i.e. the wavelength for which the solar cells were degraded and monitored, is increased. EQE plots and illuminated IV measurements reveal that an increase in degradation temperature reduces the spectral response in the shorter wavelength region, and reduces stabilized efficiencies.

The degradation experiments also revealed that the kinetics of SWE in complete devices are perhaps not well incorporated in the existing numerical models of LID. The light induced degradation of solar cell fill factor was interpreted in terms of two regimes – slow and fast. Through a time-related power law, the fast degradation was investigated further. The results suggest that the variable referred to in Chapter 5 of this report as the time-exponent, x, is not a constant for a given material/device but rather varies according to device structure and degradation conditions. This is also in line with the efficiency fitting procedure, where the time constant, τ, showed a similar tendency to vary. Previous values of 1/3 and 1/2 for the time-exponent, x, were not reproduced in the experimental results presented in this report.

Conclusions from Annealing

Some permanent degradation is noted in the R_0 devices after LID. Regardless of intrinsic layer thickness, the first hour of annealing leads to a rapid increase in solar cell performance. The kinetics of the annealing process may indicate the existence of hard and soft defects within the material, and it is indicated that permanent degradation may stem from the hard defects. Moreover, the annealing results suggest that the main part of the LID stems from soft defects. In terms of this interpretation, it is possible that a larger proportion of the light induced defects are soft in the thicker devices when compared to thinner devices.

The thickness dependence of the thermal annealing process shows that EQE in the longer wavelength region recovers faster than the EQE in the shorter wavelength region. In terms of the classical view on charge carrier generation profile as a function of depth in the device, this is interpreted as another indication that hole propagation is less affected by the defects in the material than electron propagation. Moreover, the permanent degradation, which herein is associated with hard defects, occurs in the blue part of the spectrum.

It was found that annealing kinetics in R_0 solar cells are independent of degradation temperature. Rather, the degraded state of the solar cell performance was the only thing affected by the degradation temperature. This is interpreted as a sign that soft and hard defects are indeed in play in the amorphous material. The increase in degradation temperature yields fewer soft defects in the degraded state of the device, but does not affect the density of the hard defects. Meanwhile, the annealing kinetics in R_{20} samples are shown to depend on the temperature during degradation. EQE measurements and illuminated IV-measurements reveal that R_{20} devices degraded at higher temperatures show fluctuations in their performance levels after a few hours of annealing. This anomaly could not be explained here. However, we note the peculiar dependency of the R_{20} devices on degradation temperature.

Meanwhile, the annealing kinetics of R_0 and R_{20} samples which were degraded at $\mathrm{T} = 25°\mathrm{C}$ are equal, albeit with different starting points. The R_{20} samples showed a tendency to fully recuperate, and even surpass, the initial performance levels. The evolution of solar cell performance due to annealing has been interpreted in terms of defect types, and it was suggested that the R_{20} samples generate the same amount of soft defects as the R_0 devices. Meanwhile, the results may indicate a lower generation of hard defects in the R_{20} material, as opposed to the R_0 material. This is consistent with the interpretation that permanent damage is inflicted by the existence of hard defects in the material, which by definition require more than a thermal anneal at $T = 130°C$ to be removed.

The results show that EQE is fully recovered in the longer wavelength region due to thermal annealing, independent of hydrogen dilution of the intrinsic layer material. Thereby, the EQE in the red part of the spectrum is consistently more elevated than the spectral response in the shorter wavelength region. This is interpreted in terms of carrier collection, and it is possible that hole propagation in the device is less affected by the remaining defects in the a-Si:H intrinsic layer caused by the SWE. Furthermore, the R_{20}-type solar cell's EQE shows a full recovery throughout the entire spectral region. In terms of the discussion on soft and hard defects presented in this report, it is suggested that the degradation in the lower wavelength region of the spectral response in the undiluted material solar cells is caused by the hard defects. This is also consistent with the claim that hydrogen diluted material is more resistant to creation of hard defects.

The dark current-voltage characteristics were measured in a state where the solar cells were only partially annealed, and thus still showing clear signs of degradation. The R_0-type solar cell surveyed in this report was annealed for 20 hours before the dark IV measurement was carried out. At this stage, the solar cell showed the same thermal ideality factor and mobility bandgap as in its initial state. The numerical modeling theory of Pieters *et al.* therefore still seems valid for the annealed-degraded R_0-cell at this stage. Furthermore, the voltage-dependent ideality factor was more or less identical to the initial values. In terms of spatial defect distribution within the device, this may suggest that the p-i interface region is largely unchanged due to the remaining light induced defects in the device. Meanwhile, there were clear signs of reduced thermal activation energy of the recombination current for strong reverse bias. This may be indicative of the Poole-Frenkel effect, and therefore, that the defect density in the R_0-type material after 20 hours of annealing is still at higher values compared to the as-deposited state. As was pointed out in Chapter 6 of this report, the remaining defects in the R_0-sample at this point in its annealing process are believed to be hard defects. As such, the thermal activation energy seems to indicate that these hard defects will actively contribute to the dark current under the influence of a strong internal electric field.

The dark IV results of the R_{20}-type solar cell after 1 hour of annealing showed clear signs of alteration and degradation for both forward and reverse bias voltages. The thermal ideality factor, and consequently, the mobility bandgap of the annealed-degraded state is not consistent with the theory presented by Pieters *et al.* Moreover, a clear alteration in the voltage-dependent ideality factor is observed, which, according to the interpretation of the ideality factor presented in this report, suggests a clear change in the energetic distribution of defects. Meanwhile, the results obtained here for the R_{20}-type solar cells do not indicate that the p-i interface region is unaffected by the LID. The observed drop in activation energy for strong reverse bias is also observed for the R_{20}-type device. This is again associated with the Poole-Frenkel effect within the degraded solar cell.

7.2 Future Recommendations

Wavelength Dependence of Degradation

One of the aims of this project was to investigate the degradation characteristics of solar cells exposed to infrared light of wavelength $\lambda = 630\ \mathrm{nm}$. As any measurement of EQE will show, the performance of the solar cell devices is highly dependent on the spectral region for which it is considered. Moreover, this study has shown how the degradation affects the spectral response of a solar cell differently for different wavelengths. It is believed that the degradation kinetics also might vary as a result of a change in light soaking wavelength. In terms of mapping out the defect generation as a function of depth in the device, alterations in wavelength may yield a higher resolution and more decisive evidence. Furthermore, the in-situ degradation setup of the PVMD is an excellent instrument for monitoring degradation evolution of the solar cells. As such, the degradation characteristics for different light soaking wavelength can be picked up, compared, and analyzed with a high degree of precision and reliability.

Hydrogen Dilution Dependence of Degradation

In this study, the degradation evolution of undiluted solar cells was compared to that of solar cells with a hydrogen dilution of R = 20. The differences in degradation profiles and annealing characteristics indicate that the material properties of the two types of devices play a definite role in the SWE. The dependence of degradation and annealing on hydrogen dilution ratio became all the more visible for higher degradation temperatures. Therefore, it would be interesting to investigate this matter more thoroughly. It was suggested in this report that hydrogen diluted samples may show reduced levels of the hard defects compared to undiluted solar cells. By quantitative comparisons of a larger selection of hydrogen dilution values, this claim may be verified and placed in context with nanostructural analyses of a-Si:H.

Intensity Dependence of Degradation

The light soaking intensity was a fixed parameter for all samples tested in this project. As mentioned earlier in this report, the light soaking intensity was arbitrarily set to the value for which the short circuit current of the first R_0-type solar cell of 600 nm was equal to its short circuit current, I_{SC}, under the AM1.5 spectrum. By altering the light intensity, one is ultimately manipulating the excess charge carrier density within the material. Consequently, the recombination levels during illumination within the material will inevitably change. This may yield valuable information as to defect creation and LID behavior of the amorphous material. Again, using the custom degradation setup with in-situ measurement possibilities will yield reliable, high-resolution results, which may pick up differences which previously have gone unnoticed.

Temperature Dependence of Degradation

In this project the temperature dependence of SWE was investigated in some detail for solar cells devices with non-H-diluted and H-diluted intrinsic layers. While the degradation of R_0-type solar cells was monitored for two different temperatures, the R_{20} was degraded at an additional third temperature as well. In order to make clearer comparisons, and achieve a higher resolution in the temperature-dependence of the SWE, it is desirable to repeat several more degradation runs between $20℃$ and $60℃$ with smaller intervals. Furthermore, degrading solar cells at sub-zero temperatures is another interesting option to explore. Degrading solar cells at room temperature and over probes the realistic outdoor performance scenario of the solar cell, and includes effects of thermal annealing and thermal induction of defects. In order to minimize the effect of these two processes on LID, however, decreasing the degradation temperature drastically is an interesting alternative. This may yield a clearer picture of the kinetics of defect creation and the activation energy of defect creation discussed in Chapter 5 of this report.

Modeling Degradation and Solar Cell Behavior

Previous studies have shown the capability of solar cell modeling to accurately predict and explain experimental results. The *Advanced Semiconductor Analysis (ASA)* software package, developed at the TU Delft, is a comprehensive and powerful tool to this end. Originally, it was intended that a part of this Master thesis project would consist of modeling the light induced degradation which we monitored and measured. As such, it was hoped that ASA could provide valuable information on the evolution of spatial defect distribution within the amorphous material, recombination profiles, energy band diagrams, et cetera. Due to time constraints, this was not carried out as a part of this project. Meanwhile, some efforts were made to understand how to go about this process. The primary concern with a complex modeling software is the vast number of variables and parameters. In order to trust the model implemented, it is therefore essential to construct it based on realistic values and experimental data. In other words, it is essential to create a well-calibrated model of the as-deposited solar cells one would like to simulate. This consists of thoroughly characterizing the material used in the solar cell device, and the different layers. The thickness of each layer should be precisely measured. Moreover, the wavelength dependent optical constants of each layer, as well as the surface texturing, should be measured and used as input in the model. When simulated absorptivity and reflectivity match the experimental values, the optical part of the model is set. This means that calibration to opto-electrical characteristics like EQE and illuminated IV can be carried out without adjusting any other parameters than those pertaining to the electrical properties of the material. As a final calibration step, the dark IV simulations should aptly reflect the measured values. When the optical and electrical calibration of the solar cell is complete, it is possible to use it in a study of light induced degradation. Hence, a thorough and consistent approach is highly recommended for future modeling analysis. In practice, this implies that when a solar cell is to be analyzed, each unique layer of which it is comprised should be deposited separately in order to extract the necessary inputs to the solar cell model.

Appendix A : Degradation Figures

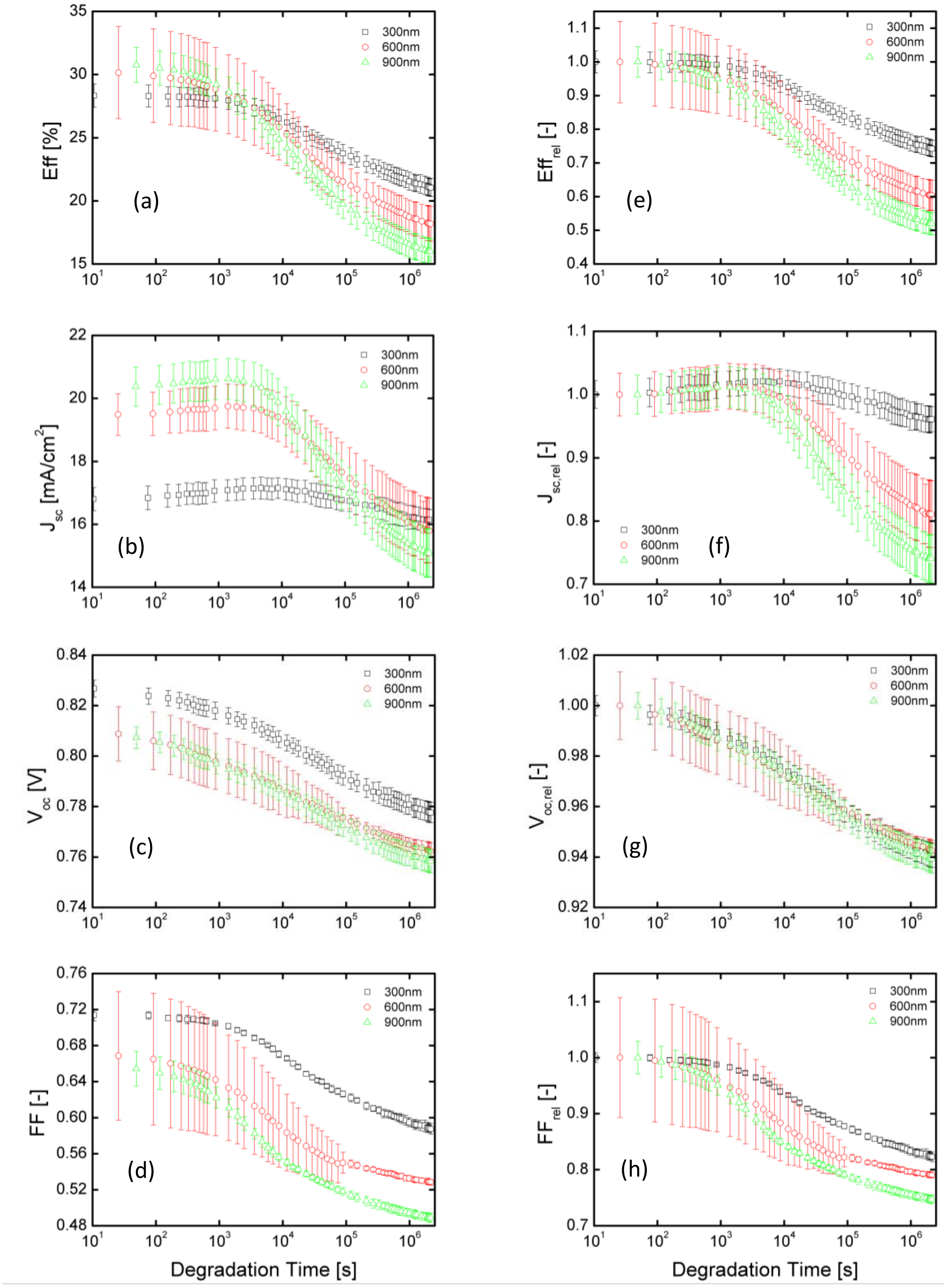

A-1: External parameter evolution of a R_0 solar cell thickness series under light soaking at $T = 45°C$. The samples were degraded for 200 hours under LEDs of wavelength $\lambda = 630$ nm. The degradation is depicted in (a)-(d) absolute terms, and (e)-(h) relative terms.

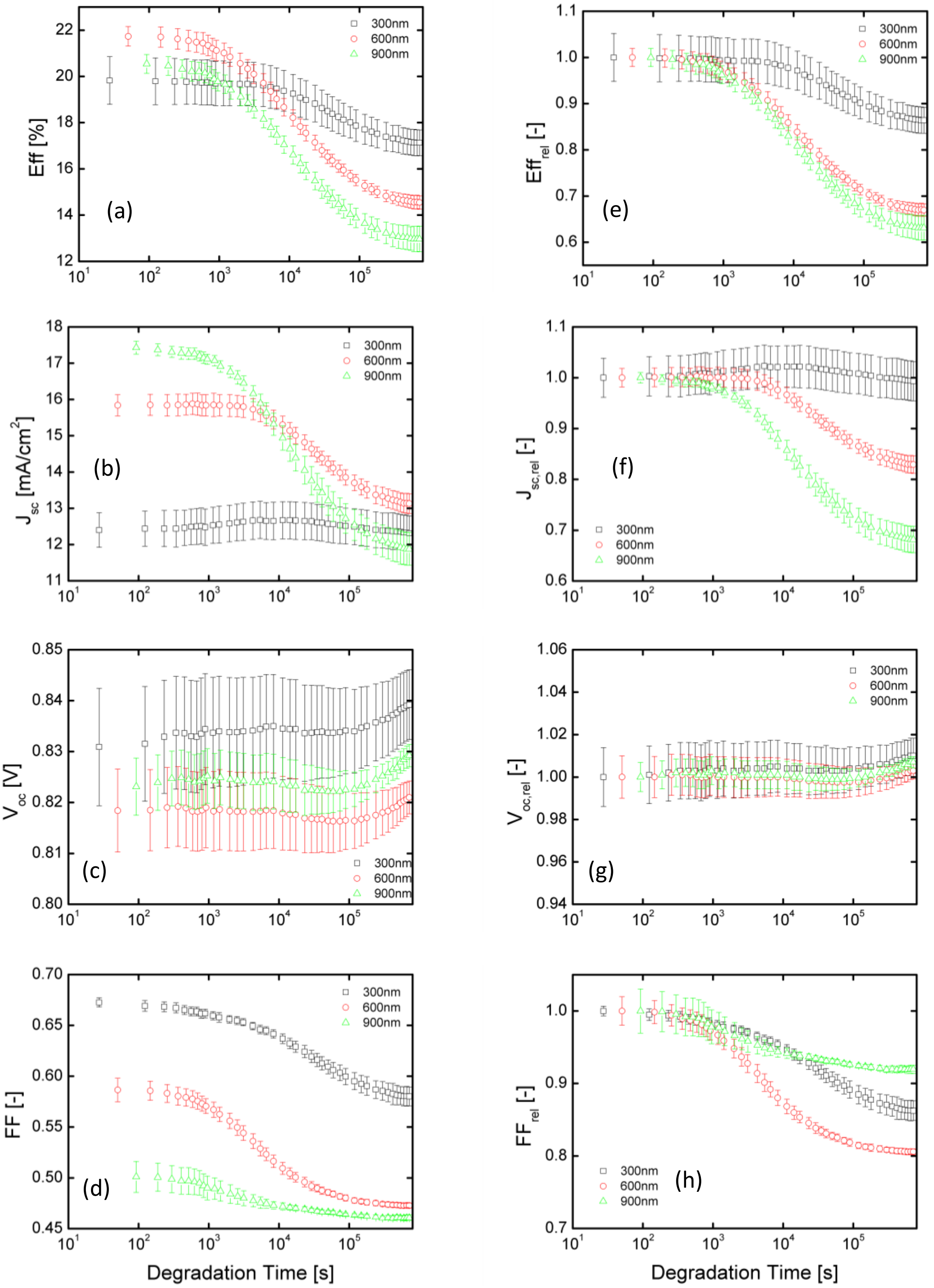

A-2: External parameter evolution of a R_{20} solar cell thickness series under light soaking at $\mathrm{T} = 25^{\circ}\mathrm{C}$. The samples were degraded for 200 hours under LEDs of wavelength $\lambda = 630\ \mathrm{nm}$. The degradation is depicted in (a)-(d) absolute terms, and (e)-(h) relative terms.

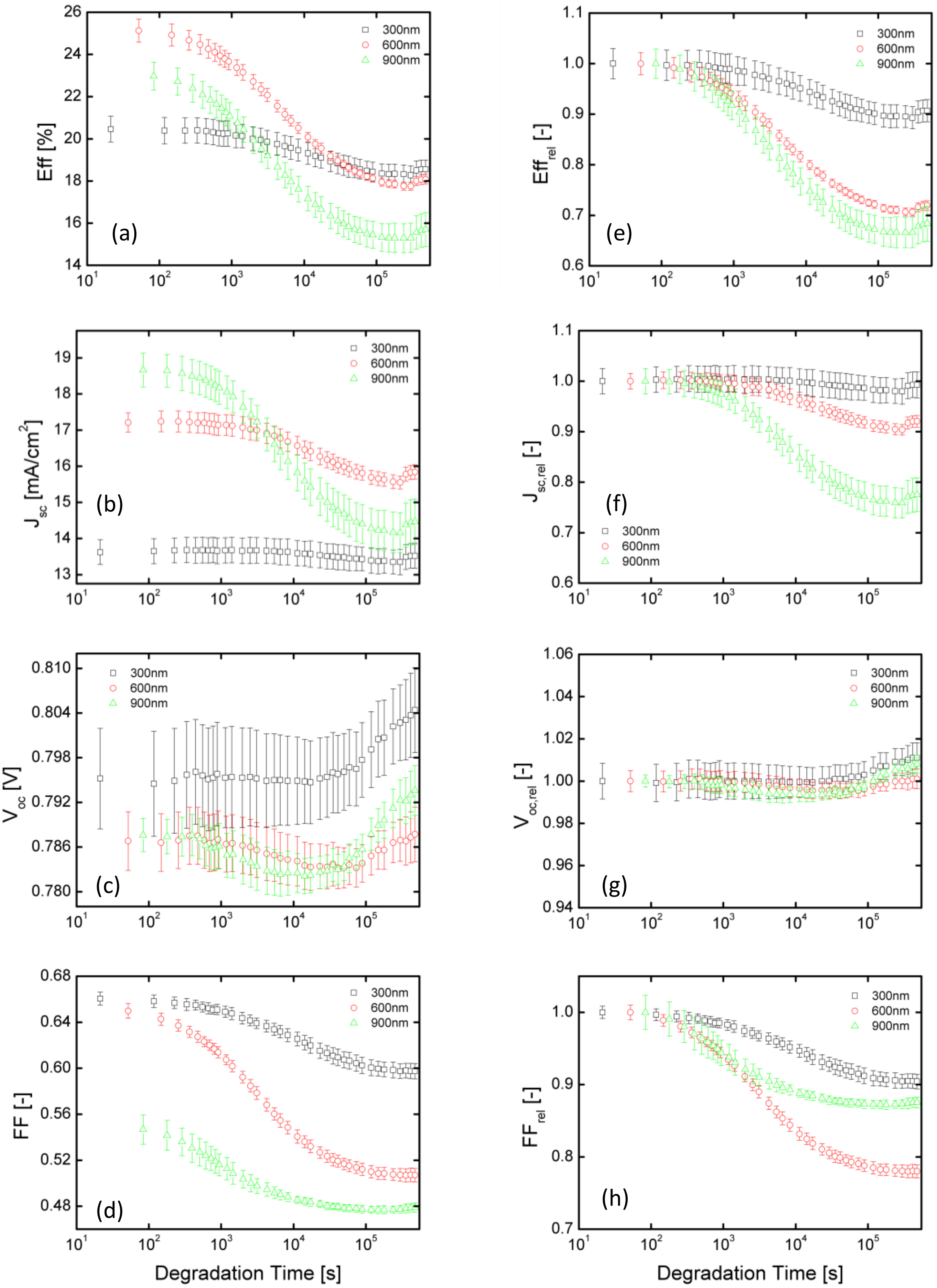

A-3: External parameter evolution of a R_{20} solar cell thickness series under light soaking at $T = 45$°C. The samples were degraded for 132 hours under LEDs of wavelength $\lambda = 630$ nm. The degradation is depicted in (a)-(d) absolute terms, and (e)-(h) relative terms.

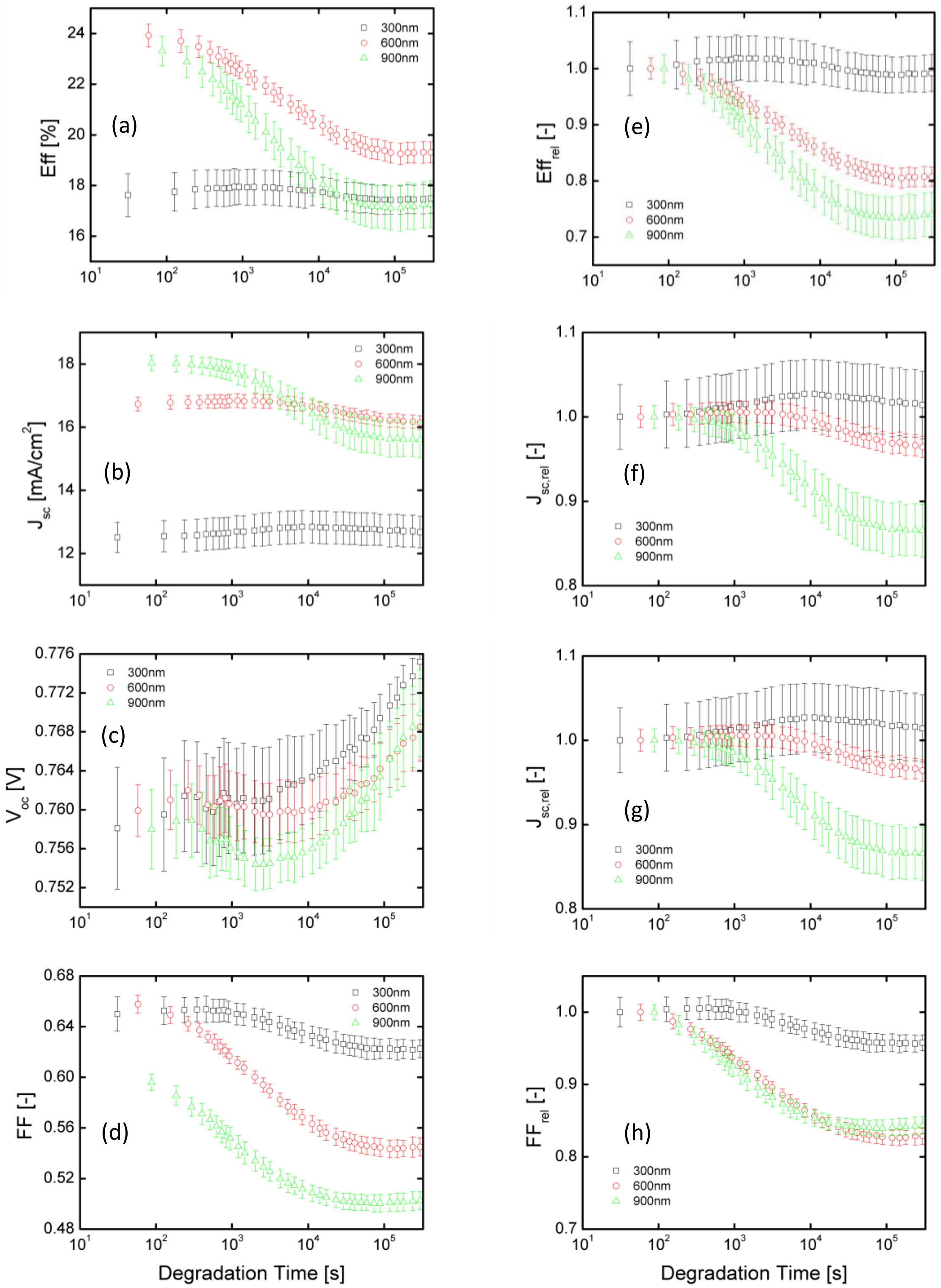

A-4: External parameter evolution of a R_{20} solar cell thickness series under light soaking at $\mathrm{T} = 60°\mathrm{C}$. The samples were degraded for 83 hours under LEDs of wavelength $\lambda = 630\ \mathrm{nm}$. The degradation is depicted in (a)-(d) absolute terms, and (e)-(h) relative terms.

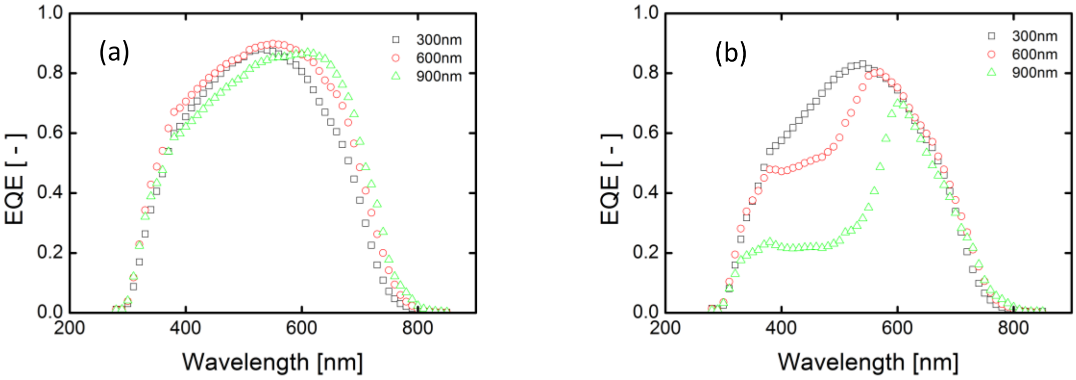

A-5: EQE of a thickness series of R_0-type solar cells degraded at $\mathrm{T} = 45°\mathrm{C}$ for 200 hours under LED light of wavelength $\lambda = 630\ \mathrm{nm}$. The EQE is shown for (a) initial state, and (b) degraded state

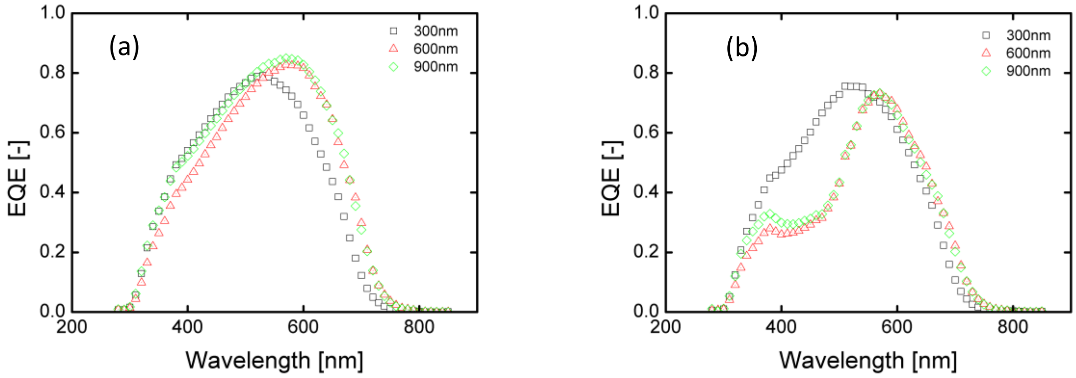

A-6: EQE of a thickness series of R_{20}-type solar cells degraded at $\mathrm{T} = 25°\mathrm{C}$ for 200 hours under LED light of wavelength $\lambda = 630\ \mathrm{nm}$. The EQE is shown for (a) initial state, and (b) degraded state

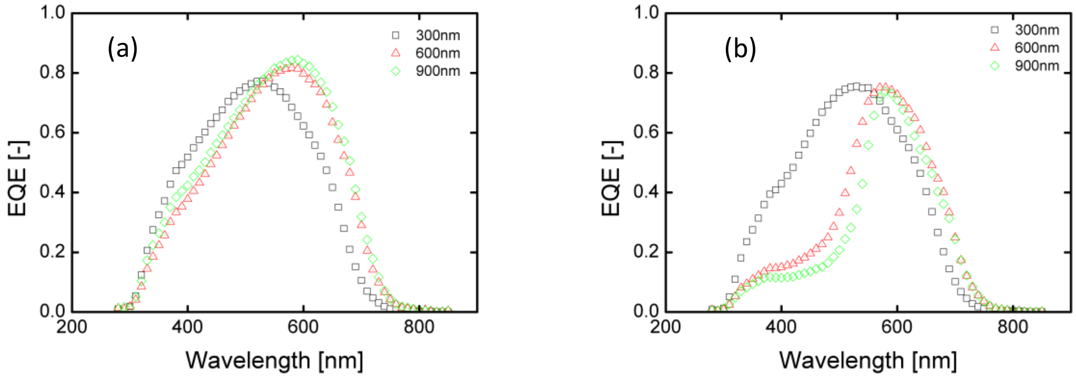

A-7: EQE of a thickness series of R_{20}-type solar cells degraded at $\mathrm{T} = 45°\mathrm{C}$ for 132 hours under LED light of wavelength $\lambda = 630\ \mathrm{nm}$. The EQE is shown for (a) initial state, and (b) degraded state

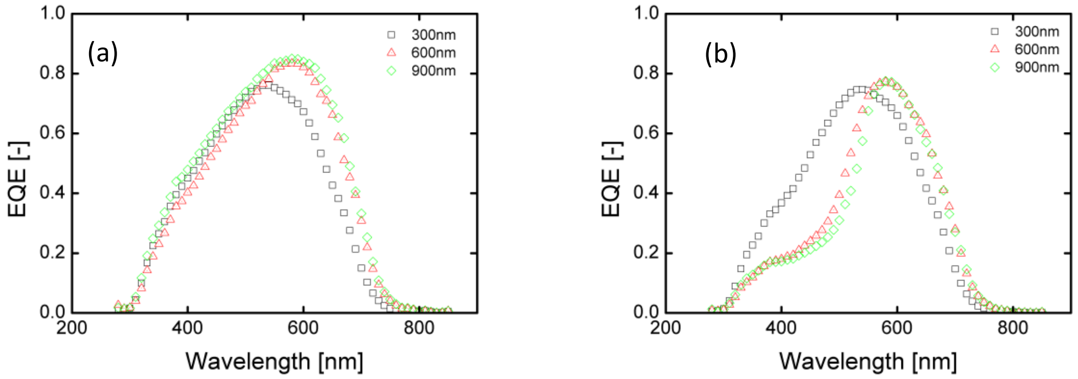

A-8: EQE of a thickness series of R_{20}-type solar cells degraded at $\mathrm{T} = 60°\mathrm{C}$ for 83 hours under LED light of wavelength $\lambda = 630\ \mathrm{nm}$. The EQE is shown for (a) initial state, and (b) degraded state.

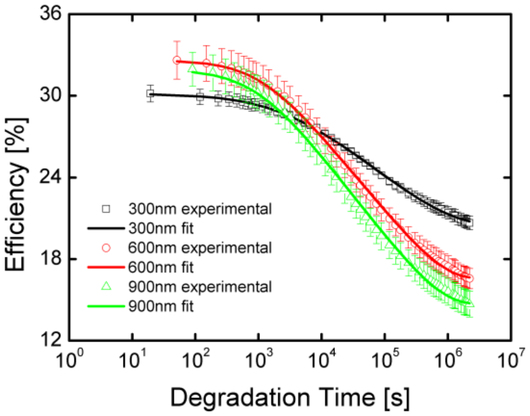

A-9: Fitted efficiency curves for an R_0-type thickness series degraded cells degraded at $\mathrm{T} = 25°\mathrm{C}$ for 700 hours under LED light of wavelength $\lambda = 630\ \mathrm{nm}$.

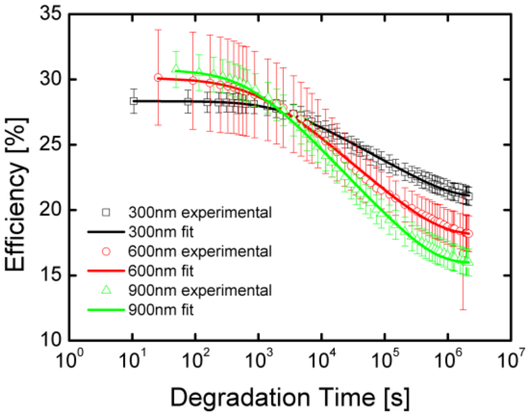

A-10: Fitted efficiency curves for an R_0-type thickness series degraded cells degraded at $\mathrm{T} = 45°\mathrm{C}$ for 200 hours under LED light of wavelength $\lambda = 630\ \mathrm{nm}$.

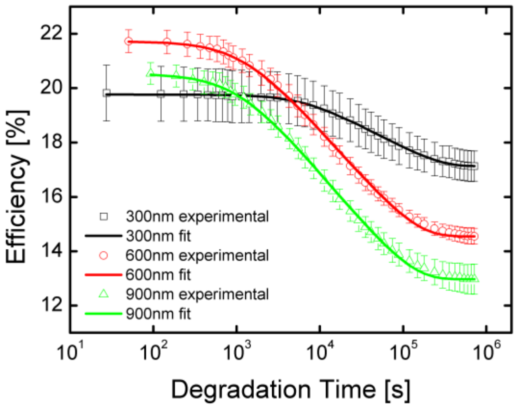

A-11: Fitted efficiency curves for an R_{20}-type thickness series degraded cells degraded at $\mathrm{T} = 25℃$ for 200 hours under LED light of wavelength $\lambda = 630$ nm.

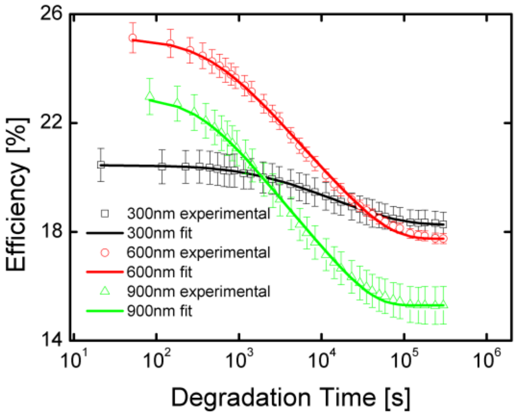

A-12: Fitted efficiency curves for an R_{20}-type thickness series degraded cells degraded at $\mathrm{T} = 45℃$ for 132 hours under LED light of wavelength $\lambda = 630$ nm.

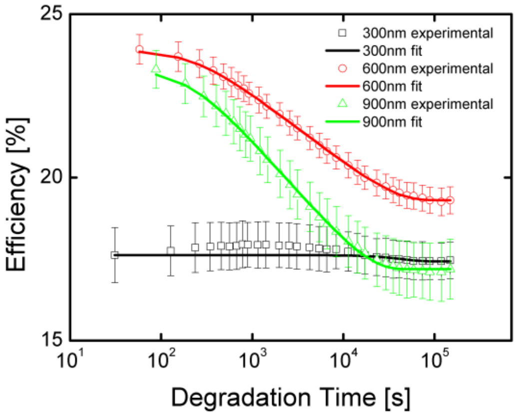

A-13: Fitted efficiency curves for an R_{20}-type thickness series degraded cells degraded at $\mathrm{T} = 60℃$ for 83 hours under LED light of wavelength $\lambda = 630$ nm.

Appendix B : Annealing Figures

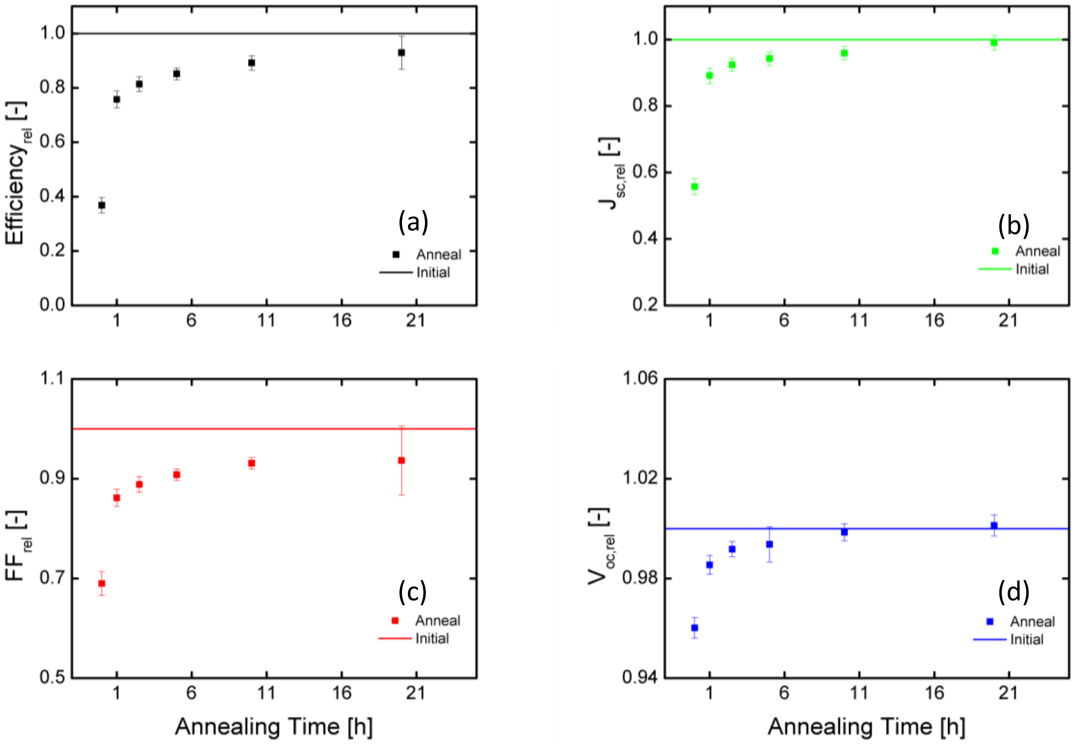

B-1: 10 cell-averaged annealing evolution of a R_0-type 600 nm intrinsic layer solar cell degraded at $\mathrm{T} = 25°\mathrm{C}$ for 700 hours under under LED light of wavelength $\lambda = 630$ nm. The sample is annealed for 20 hours at $\mathrm{T} = 130°\mathrm{C}$.

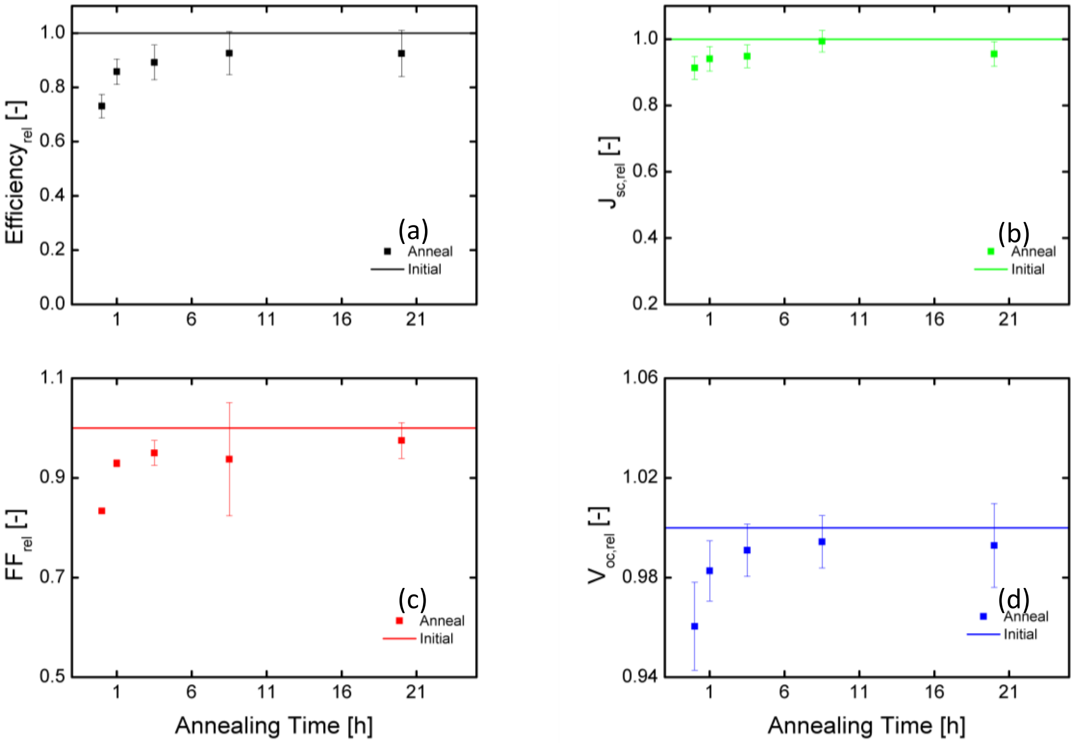

B-2: 3-cell averaged annealing evolution of a R_0-type 300 nm intrinsic layer solar cell degraded at $\mathrm{T} = 45°\mathrm{C}$ for 200 hours under under LED light of wavelength $\lambda = 630$ nm. The sample is annealed for 20 hours at $\mathrm{T} = 130°\mathrm{C}$.

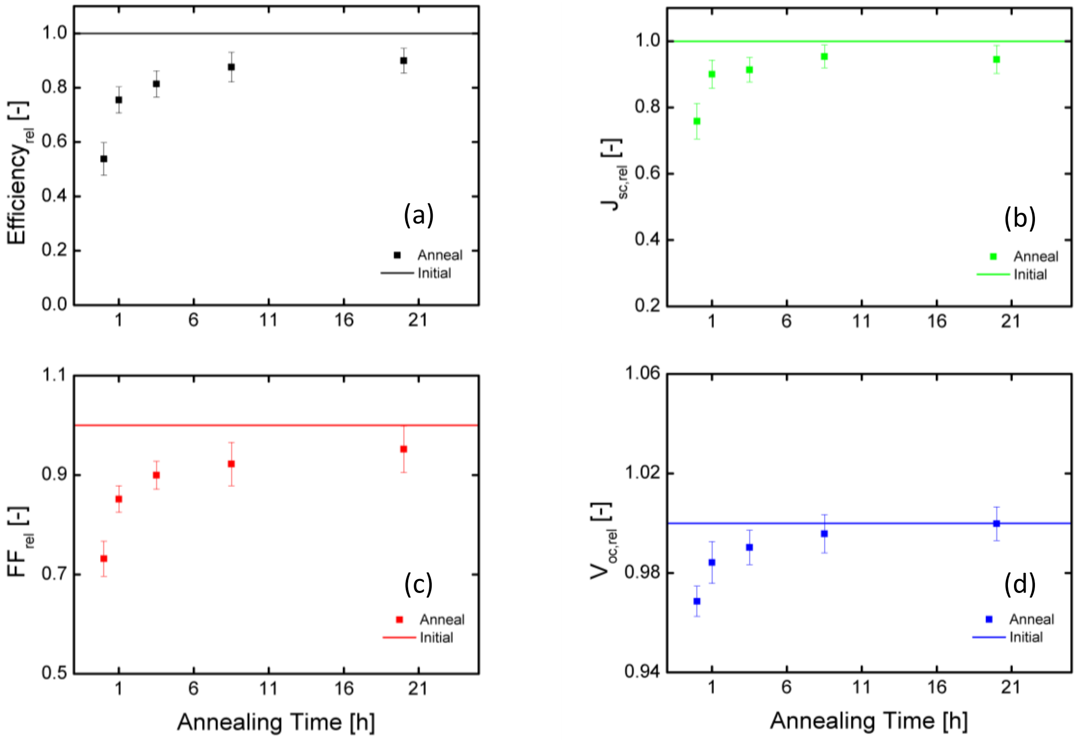

B-3: 8-cell averaged annealing evolution of a R_0-type 600 nm intrinsic layer solar cell degraded at $\mathrm{T} = 45°\mathrm{C}$ for 200 hours under under LED light of wavelength $\lambda = 630$ nm. The sample is annealed for 20 hours at $\mathrm{T} = 130°\mathrm{C}$.

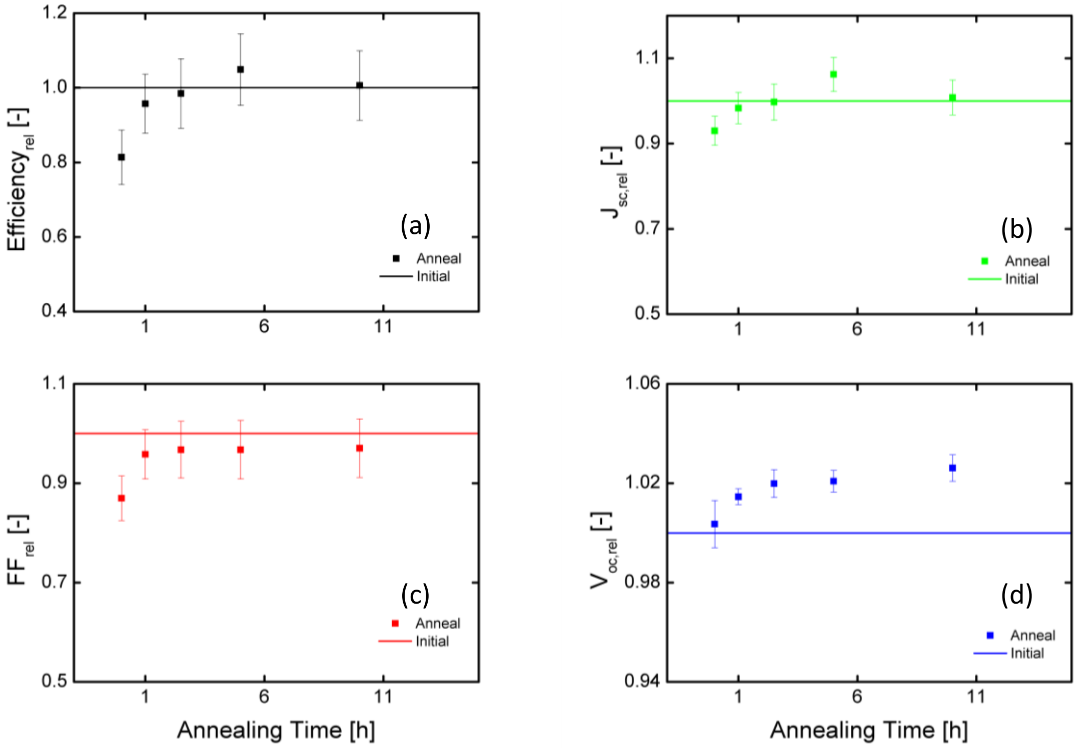

B-4: 7-cell averaged annealing evolution of a R_{20}-type 300 nm intrinsic layer solar cell degraded at $\mathrm{T} = 25°\mathrm{C}$ for 200 hours under under LED light of wavelength $\lambda = 630$ nm. The sample is annealed for 10 hours at $\mathrm{T} = 130°\mathrm{C}$.

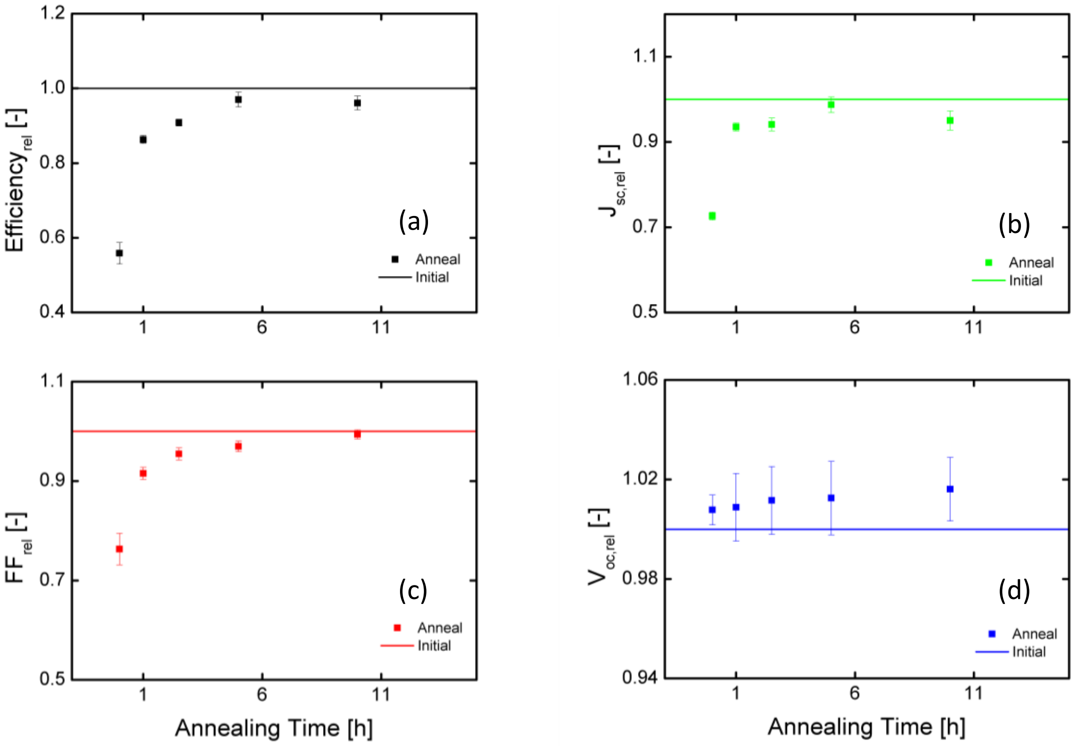

B-5: 6-cell averaged annealing evolution of a R_{20}-type 600 nm intrinsic layer solar cell degraded at $\mathrm{T} = 25℃$ for 200 hours under under LED light of wavelength $\lambda = 630\ \mathrm{nm}$. The sample is annealed for 10 hours at $\mathrm{T} = 130℃$.

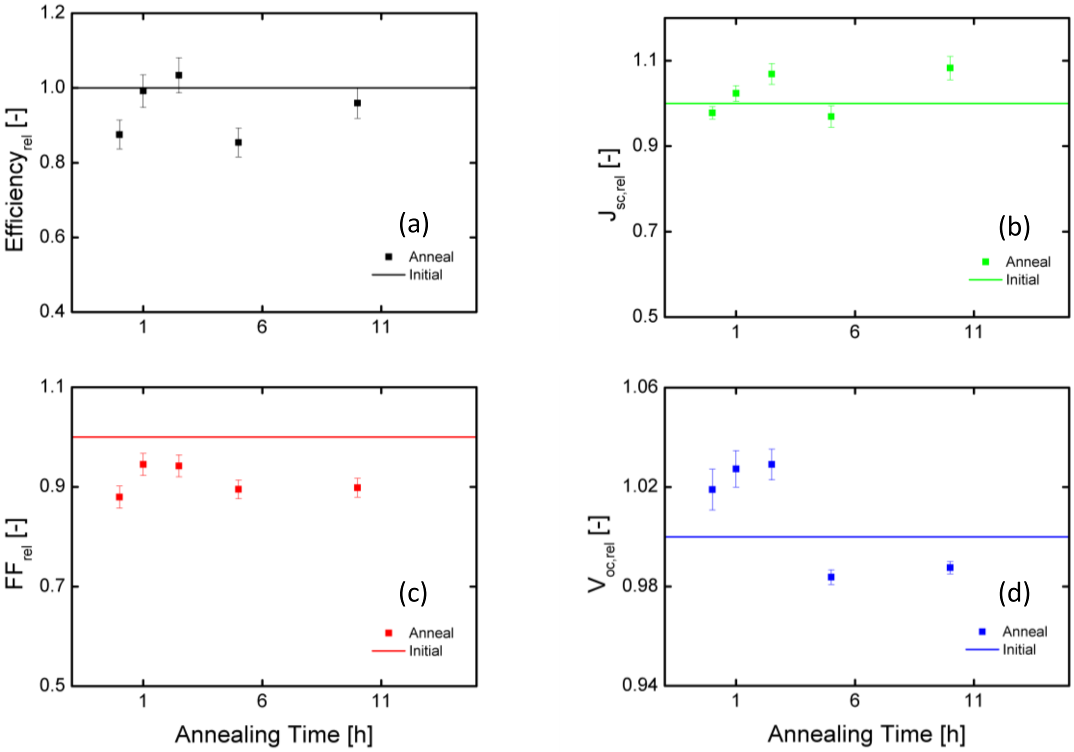

B-6: 4-cell averaged annealing evolution of a R_{20}-type 300 nm intrinsic layer solar cell degraded at $\mathrm{T} = 45℃$ for 132 hours under under LED light of wavelength $\lambda = 630\ \mathrm{nm}$. The sample is annealed for 10 hours at $\mathrm{T} = 130℃$.

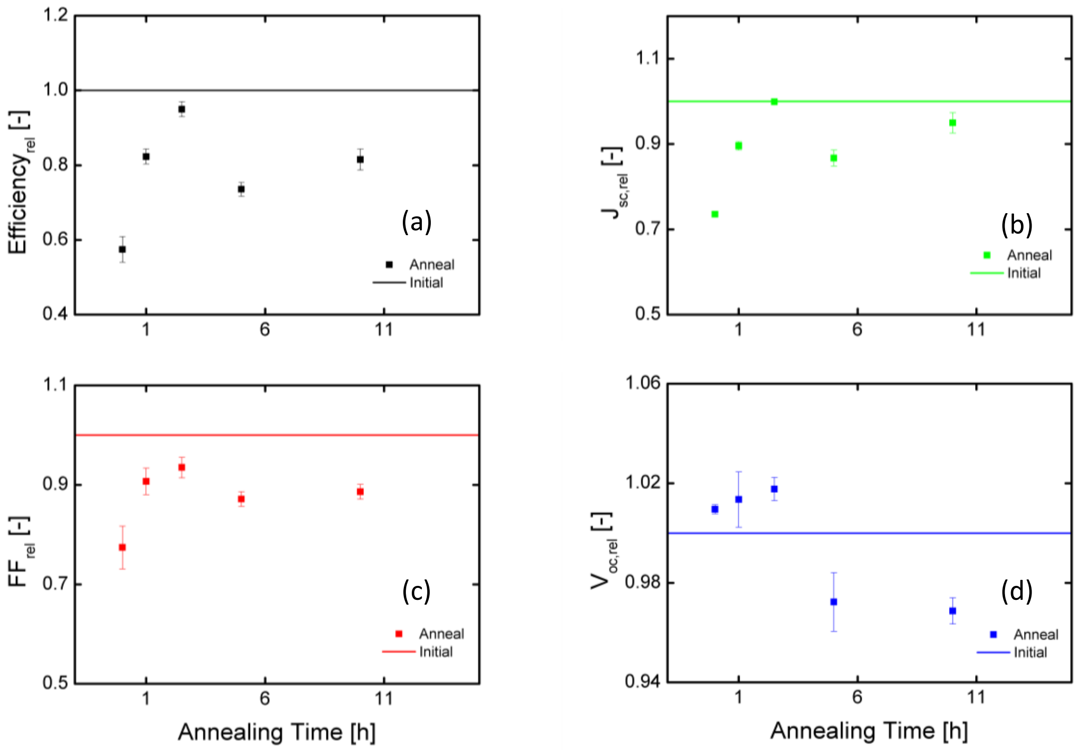

B-7: 4-cell averaged annealing evolution of a R_{20}-type 600 nm intrinsic layer solar cell degraded at $T = 45°C$ for 132 hours under under LED light of wavelength $\lambda = 630$ nm. The sample is annealed for 10 hours at $T = 130°C$.

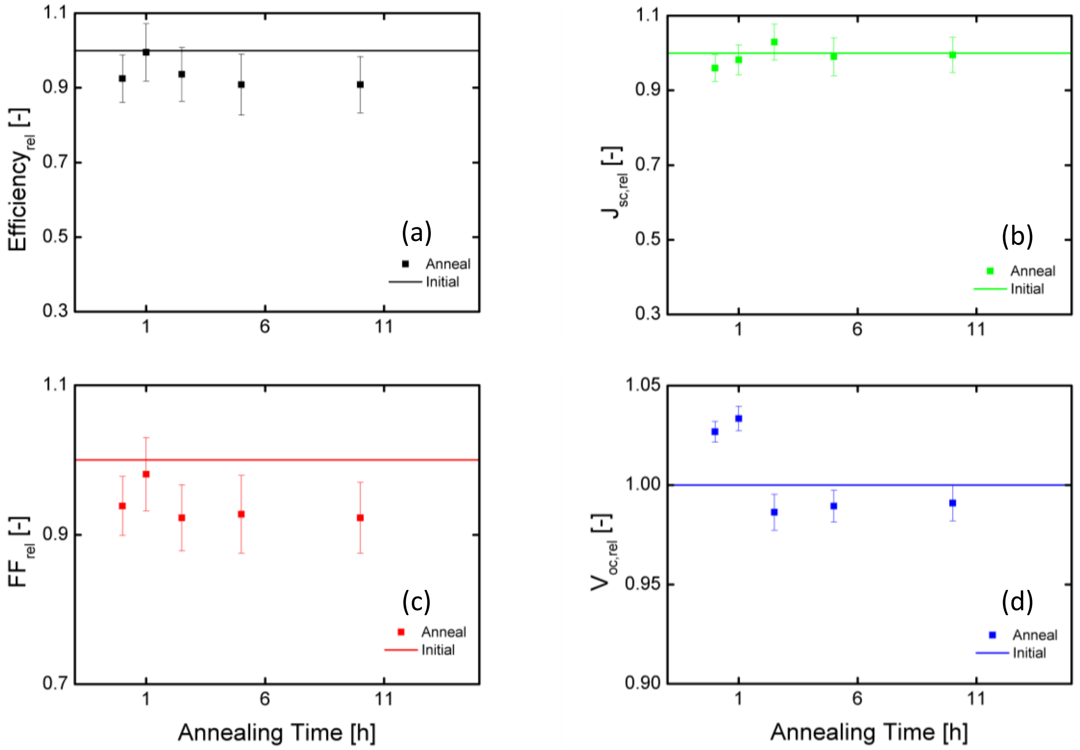

B-8: 7-cell averaged annealing evolution of a R_{20}-type 300 nm intrinsic layer solar cell degraded at $T = 60°C$ for 83 hours under under LED light of wavelength $\lambda = 630$ nm. The sample is annealed for 10 hours at $T = 130°C$.

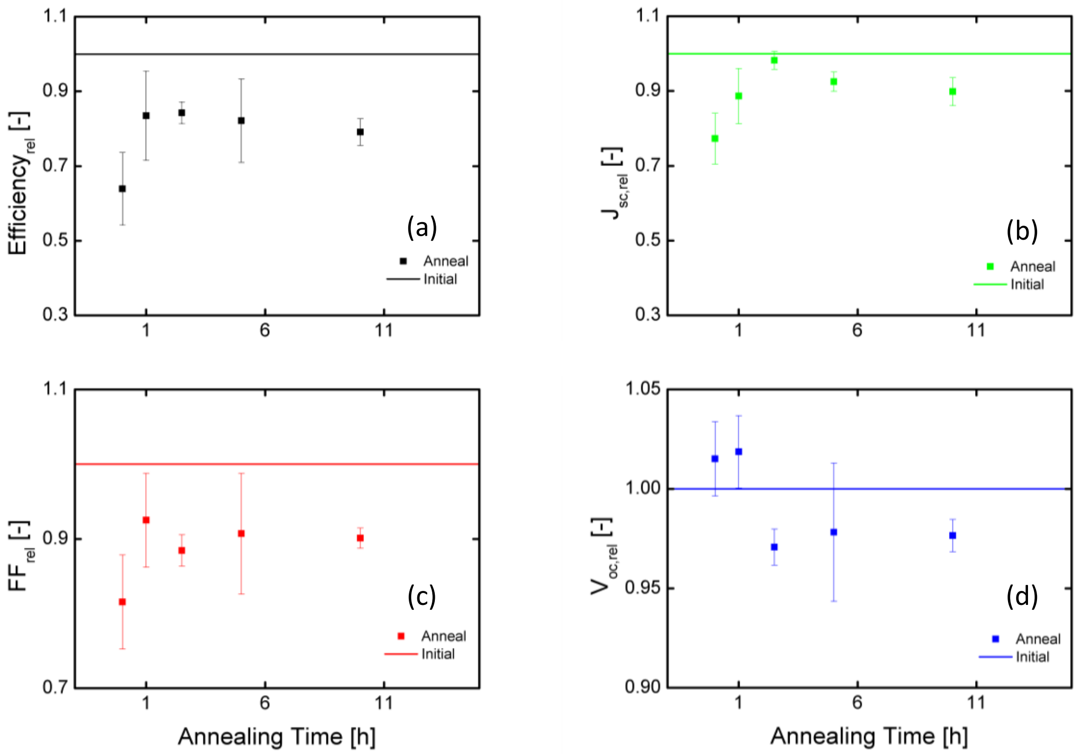

B-9: 10-cell averaged annealing evolution of a R_{20}-type 600 nm intrinsic layer solar cell degraded at $\mathrm{T} = 60°\mathrm{C}$ for 83 hours under under LED light of wavelength $\lambda = 630$ nm. The sample is annealed for 10 hours at $\mathrm{T} = 130°\mathrm{C}$.

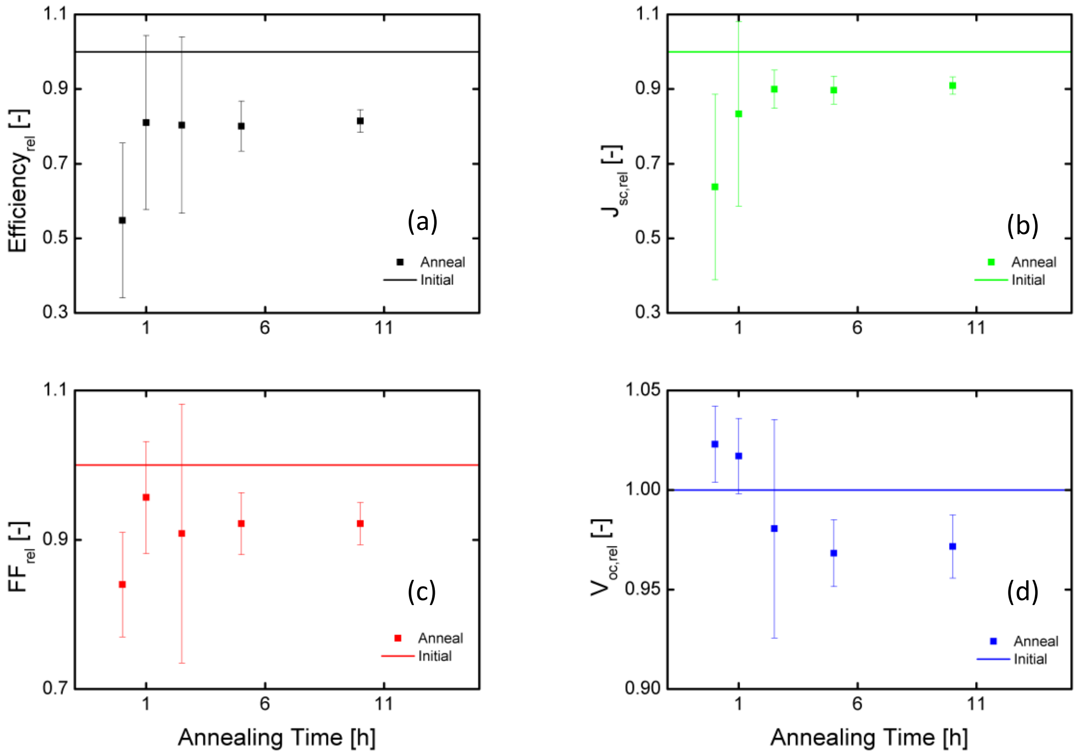

B-10: 10-cell averaged annealing evolution of a R_{20}-type 900 nm intrinsic layer solar cell degraded at $\mathrm{T} = 60°\mathrm{C}$ for 83 hours under under LED light of wavelength $\lambda = 630$ nm. The sample is annealed for 10 hours at $\mathrm{T} = 130°\mathrm{C}$.

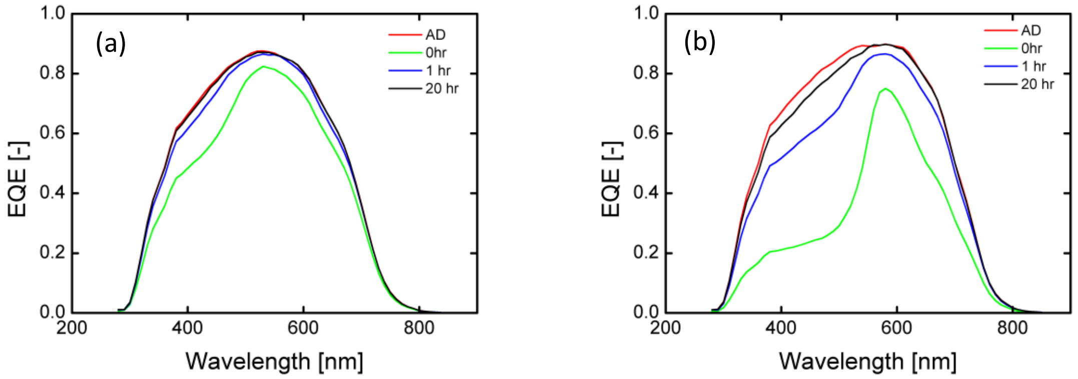

B-11: EQE evolution during thermal annealing of R_0-type solar cells with intrinsic layer thickness of (a) 300 nm, and (b) 600 nm. The samples were degraded at $\mathrm{T} = 25°\mathrm{C}$ for 700 hours under under LED light of wavelength $\lambda = 630\ \mathrm{nm}$. The samples were annealed for 20 hours at $\mathrm{T} = 130°\mathrm{C}$.

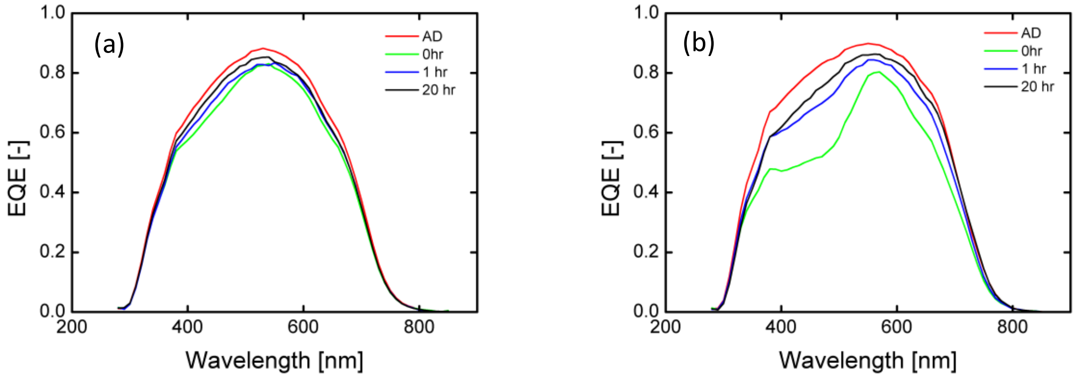

B-12: EQE evolution during thermal annealing of R_0-type solar cells with intrinsic layer thickness of (a) 300 nm, and (b) 600 nm. The samples were degraded at $\mathrm{T} = 45°\mathrm{C}$ for 200 hours under under LED light of wavelength $\lambda = 630\ \mathrm{nm}$. The samples were annealed for 20 hours at $\mathrm{T} = 130°\mathrm{C}$.

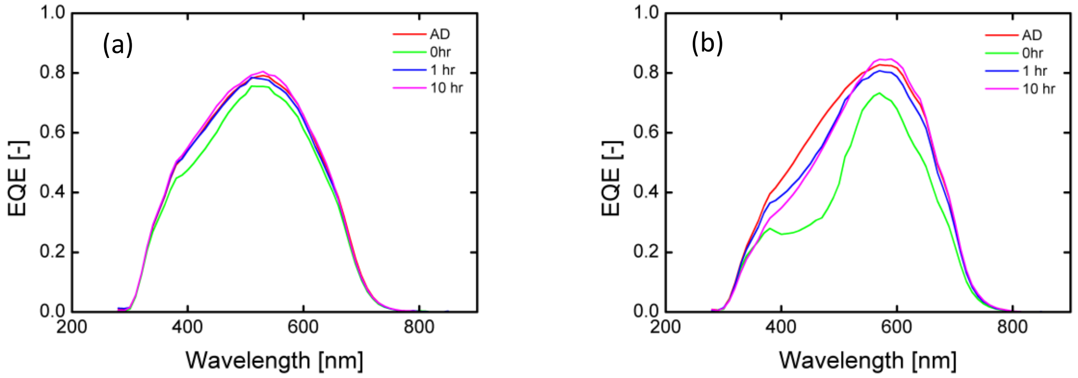

B-13: EQE evolution during thermal annealing of R_{20}-type solar cells with intrinsic layer thickness of (a) 300 nm, and (b) 600 nm. The samples were degraded at $\mathrm{T} = 25°\mathrm{C}$ for 200 hours under under LED light of wavelength $\lambda = 630\ \mathrm{nm}$. The samples were annealed for 10 hours at $\mathrm{T} = 130°\mathrm{C}$.

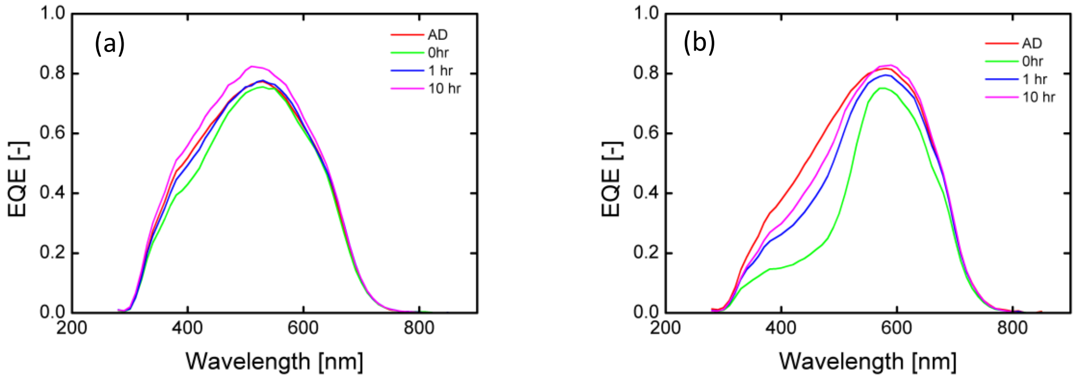

B-14: EQE evolution during thermal annealing of R_{20}-type solar cells with intrinsic layer thickness of (a) 300 nm, and (b) 600 nm. The samples were degraded at $\mathrm{T} = 45℃$ for 132 hours under under LED light of wavelength $\lambda = 630\ \mathrm{nm}$. The samples were annealed for 10 hours at $\mathrm{T} = 130℃$.

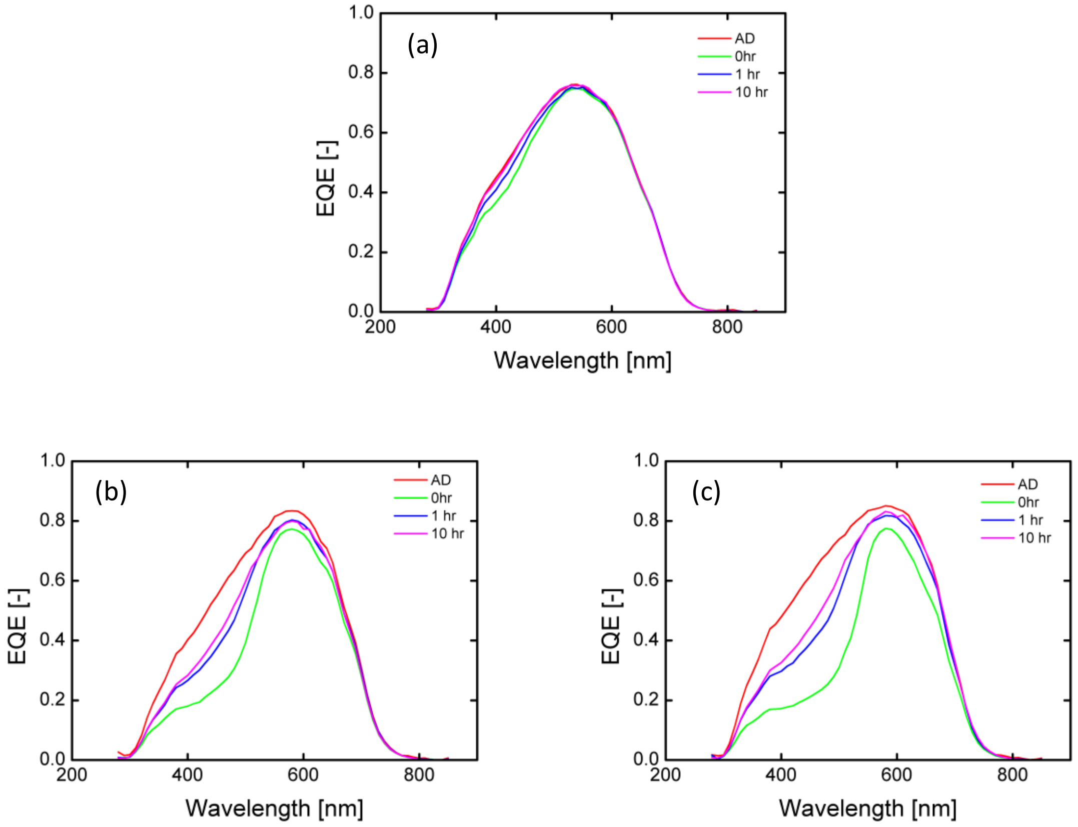

B-15: EQE evolution during thermal annealing of R_{20}-type solar cells with intrinsic layer thickness of (a) 300 nm, (b) 600 nm, and (c) 900 nm. The samples were degraded at $\mathrm{T} = 60℃$ for 83 hours under under LED light of wavelength $\lambda = 630\ \mathrm{nm}$. The samples were annealed for 10 hours at $\mathrm{T} = 130℃$.

Appendix C : Matlab Code

Data Processing of Degradation Results

```
%This script is intended for quick access to,and re-arrangment of, data
%within the degradation measurement records(file extension .epd). It is
%designed calculate an average of the best 'n' cells which satisfy a given
%yield requirements. Both the yield and the maximum number of cells to be
%considered are defined within the script.

%Log files containing averaged external parameters in both relative and
%absolute form are produced. Moreover, the aforementioned log-files contain
%the standard deviation of the collection of data.

%The choice of cells is based on the fill factor in the degraded state of
%the solar cell. The 'n' cells which have a fill factor within a given
%yield of the best degraded fill factor, are considered in the average.

%The appropriate cell numbers are recorded, and a list is created for each
%characterization measurement of the sample using the PASAN illuminated-IV
%measurement setup. As such, it is assumed that there exists IV-records
%of the initial state of the sample, the degraded state of the sample, and
%the annealed state of the sample. For each of these states, a list of the
%solar cells considered is produced in exactly the same format as within
%the .asc-file produced by the PASAN measurement system (i.e. containing
%cell position on the slab, etc.).



%%%%%%%%%%%%%%%%%%%%%%%%%%%%%%%%%%%%%%%%%%%%%%%%%%%%%%%%%%%%%%%%%%%%%%%%%%%
%
%%% DEFINE YIELD AND ‘n’ NUMBER OF CELLS TO BE CONSIDERED
%
%%%%%%%%%%%%%%%%%%%%%%%%%%%%%%%%%%%%%%%%%%%%%%%%%%%%%%%%%%%%%%%%%%%%%%%%%%%

clear all;
clc;

%set yield
yield=95;
%maximum number of cells to be considered
n_cells=10;



%%%%%%%%%%%%%%%%%%%%%%%%%%%%%%%%%%%%%%%%%%%%%%%%%%%%%%%%%%%%%%%%%%%%%%%%%%%
%
%%% DEFINE SAMPLE NAME AND PATH NAMES
%
%%%%%%%%%%%%%%%%%%%%%%%%%%%%%%%%%%%%%%%%%%%%%%%%%%%%%%%%%%%%%%%%%%%%%%%%%%%

%Define sample name
sample_name='A6735-III';


%Current directory
home_dir=cd;
```

```
%Define location of degradation files
sample_path=['C:\Users\Kim\Documents\TU Delft\SET 2nd year\MSc
Project\Degradation\R20 material\Third Sample Set\' sample_name];
%Define location of PASAN measurements for initial state of the sample
charact_path_init=['C:\Users\Kim\Documents\TU Delft\SET 2nd year\MSc
Project\Characterization Measurements\Pasan\R20\Third Sample Set\'
sample_name '\'];
%Define location of PASAN measurements for initial state of the sample
charact_path_deg=['C:\Users\Kim\Documents\TU Delft\SET 2nd year\MSc
Project\Characterization Measurements\Pasan\R20\Third Sample Set\'
sample_name2 'deg\'];
%Define location of PASAN measurements for initial state of the sample
charact_path_TA=['C:\Users\Kim\Documents\TU Delft\SET 2nd year\MSc
Project\Characterization Measurements\Pasan\R20\Third Sample Set\'
sample_name 'degTA\'];
%Enter folder containing degradation data
cd(sample_path);



%%%%%%%%%%%%%%%%%%%%%%%%%%%%%%%%%%%%%%%%%%%%%%%%%%%%%%%%%%%%%%%%%%%%%%%%%%%
%
%%% RETRIEVE DEGRADATION DATA FROM .LOG-FILES
%
%%%%%%%%%%%%%%%%%%%%%%%%%%%%%%%%%%%%%%%%%%%%%%%%%%%%%%%%%%%%%%%%%%%%%%%%%%%

%% Retrieve data from log files (time vector, Temperature, Jsc, FF, Voc,
Eff)
%Create a file-list containing the names of all the .epd files
%and create a matlab structure based on the number of cells/dots
dataList=dir(['*.epd']);
dataCell=cell(1,length(dataList));
best_ff=0;
format shorte;

%Read external parameter degradation record of each cell/dot in the sample
%Find the best fill factor at the end of the degradation run
for i=1:length(dataList)

    %Read data
    fid=fopen(dataList(i).name);
    data = textscan(fid,'%*f %f %*f %*s %*s %*f %f %f %*f %f %f %*f %*f %f
%f','HeaderLines',7,'Delimiter','\t','CollectOutput',1);
    fclose(fid);

    %Find best fill factor
    if data{1}(length(data{1}),5)>=best_ff
        best_ff=data{1}(length(data{1}),5);
    end
    dataCell(1,i)=data(1);
end
```

```
%%%%%%%%%%%%%%%%%%%%%%%%%%%%%%%%%%%%%%%%%%%%%%%%%%%%%%%%%%%%%%%%%%%%%%%%%%%
%
%%% DEFINE WHICH CELLS ARE TO BE CONSIDERED FOR THE AVERAGE
%
%%%%%%%%%%%%%%%%%%%%%%%%%%%%%%%%%%%%%%%%%%%%%%%%%%%%%%%%%%%%%%%%%%%%%%%%%%%


%exclude the dots based on yield, as defined earlier, and number of
%cells/dots to be considered for the average, also defined earlier.

%create dummy vector to hold fill factor values of each cell, as well as
%corresponding cell/dot number
ff_indices_vect=zeros(2,length(dataCell));
for ff=1:length(ff_indices_vect)
    ff_indices_vect(1,ff)=ff;
    ff_indices_vect(2,ff)=dataCell{ff}(length(dataCell{1}),5);
end

i_ext=1;
%Remove cells/dots which do not fullfil the given yield requirement
for i=1:length(dataCell)
    if dataCell{i_ext}(length(dataCell{1}),5)<yield*best_ff
        ff_indices_vect(:,i_ext)=[];
        dataCell(i_ext)=[];
    else
        i_ext=i_ext+1;
    end
end

%variables containing cell-indices corresponding to the Matlab environment
vals=0;
order=0;
%variables containing cell-indices corresponding to dot number
vals2=0;
order2=0;

%Ensure that a maximum of 'n' cells are considered. Moreover, ensure that
%the cells are strucured in a Matlab entity in descending order based on
%fill factor values
if length(dataCell)>n_cells
   %Set Matlab-structure in descending order
   [vals,order] = sort(cellfun(@(v)v(length(dataCell{1}),5),dataCell));
   vals=flipud(vals')';
   order=flipud(order')';

   %Set variable containing dot numbers in descending order
   [vals2,order2] = sort(ff_indices_vect(2,:));
   vals2=flipud(vals2')';
   ff_indices_vect_arranged=ff_indices_vect(1,order2);
   order2=ff_indices_vect_arranged(1,:);
   order2=flipud(order2')';

   %ensure that only 'n' cells are considered in average
   dataCellSorted=dataCell(order);
    while length(dataCellSorted)>n_cells
        dataCellSorted(n_cells+1)=[];
        order(n_cells+1)=[];
        order2(n_cells+1)=[];
```

```
    end
else

    [vals,order] =
sort(cellfun(@(v)v(length(dataCell{1}),5),dataCell),'descend');
    dataCellSorted=dataCell(order);

   %Set variable containing dot numbers in descending order
   [vals2,order2] = sort(ff_indices_vect(2,:));
   vals2=flipud(vals2')';
   ff_indices_vect_arranged=ff_indices_vect(1,order2);
   order2=ff_indices_vect_arranged(1,:);
   order2=flipud(order2')';
end



%%%%%%%%%%%%%%%%%%%%%%%%%%%%%%%%%%%%%%%%%%%%%%%%%%%%%%%%%%%%%%%%%%%%%%%%%%%%
%
%%% PRINT LIST OF CELLS TO BE CONSIDERED
%
%%%%%%%%%%%%%%%%%%%%%%%%%%%%%%%%%%%%%%%%%%%%%%%%%%%%%%%%%%%%%%%%%%%%%%%%%%%%

%Do this for initial, degraded and temperature annealed state
%This requires that the file name nomenclature for each of these three
%states is adapted to the PASAN records.

%generate .dat files for each state of the sample
fid_list1=fopen([charact_path_init 'sorted_names.dat'],'w+');
fid_list2=fopen([charact_path_deg 'sorted_names.dat'],'w+');
fid_list3=fopen([charact_path_TA 'sorted_names.dat'],'w+');

%Generate list based on ordered dot numbers.
for jj=order2
    str_print1=[dataList(jj).name(1:length(sample_name)) '_Id='
dataList(jj).name(length(sample_name)+2:length(dataList(jj).name)-4) '-'];
    str_print2=[dataList(jj).name(1:length(sample_name)) 'deg_Id='
dataList(jj).name(length(sample_name)+2:length(dataList(jj).name)-4) '-'];
    str_print3=[dataList(jj).name(1:length(sample_name)) 'degTA_Id='
dataList(jj).name(length(sample_name)+2:length(dataList(jj).name)-4) '-'];
    end
    str_print_in=dir([charact_path_init str_print1 '*']);
    str_print_deg=dir([charact_path_deg str_print2 '*']);
    str_print_TA=dir([charact_path_TA str_print3 '*']);

    fprintf(fid_list1,'%s\n',str_print_in.name);
    fprintf(fid_list2,'%s\n',str_print_deg.name);
    fprintf(fid_list3,'%s\n',str_print_TA.name);
end
fclose(fid_list1);
fclose(fid_list2);
fclose(fid_list3);


%%%%%%%%%%%%%%%%%%%%%%%%%%%%%%%%%%%%%%%%%%%%%%%%%%%%%%%%%%%%%%%%%%%%%%%%%%%%
%
%%%CREATE MATLAB-STRUCTURE CONTAINING RELATIVE VALUES OF EXTERNAL
%%%PARAMETERS
%
%%%%%%%%%%%%%%%%%%%%%%%%%%%%%%%%%%%%%%%%%%%%%%%%%%%%%%%%%%%%%%%%%%%%%%%%%%%%
```

```
dataCellSortedRel=dataCellSorted;
for j=1:length(dataCellSortedRel)
    for jj=2:length(dataCellSortedRel{1}(1,:))

dataCellSortedRel{j}(:,jj)=dataCellSortedRel{j}(:,jj)/dataCellSortedRel{j}(
1,jj);
    end
end


%%%%%%%%%%%%%%%%%%%%%%%%%%%%%%%%%%%%%%%%%%%%%%%%%%%%%%%%%%%%%%%%%%%%%%%%%%%%%
%
%%% CREATE MATRIX CONTAINING AVERAGE VALUES OF EXTERNAL PARAMETERS
%
%%%%%%%%%%%%%%%%%%%%%%%%%%%%%%%%%%%%%%%%%%%%%%%%%%%%%%%%%%%%%%%%%%%%%%%%%%%%%


%The external parameters of all cells considered are averaged for each
%time step. For consistency, the recording times are also averaged
%A matrix containing the standard deviations of the collection of dots is
%also generated
allDataMatrix_avg=zeros(length(dataCellSorted{1}),length(dataCellSorted{1}(
1,:)));
allDataMatrix_dev=allDataMatrix_avg;


data_cell=cell(1,length(dataCellSorted{1}(1,:)));
for k=1:length(dataCellSorted{1})
    %create data vectors for each time step
    for j=1:length(dataCellSorted)
        for r=1:length(dataCellSorted{1}(1,:))
            data_cell{r}=[data_cell{r}; dataCellSorted{j}(k,r)];
        end
    end

    %save averages of data vectors and standard deviations in alldatamatrix
    for r=1:length(dataCellSorted{1}(1,:))
        allDataMatrix_avg(k,r)=mean(data_cell{r});
        allDataMatrix_dev(k,r)=std(data_cell{r});
    end

    %set data vectors to zero for the next time step
    data_cell=cell(1,length(dataCellSorted{1}(1,:)));


end






%% Generated matrices containing relative values
ii=1;
allDataMatrixRel_avg=allDataMatrix_avg;
allDataMatrixRel_dev=allDataMatrix_dev;
for r=2:length(dataCellSortedRel{1}(1,:))
```

```
allDataMatrixRel_avg(:,r)=allDataMatrixRel_avg(:,r)/allDataMatrix_avg(1,r);

allDataMatrixRel_dev(:,r)=allDataMatrixRel_dev(:,r)/allDataMatrix_avg(1,r);
end


%%%%%%%%%%%%%%%%%%%%%%%%%%%%%%%%%%%%%%%%%%%%%%%%%%%%%%%%%%%%%%%%%%%%%%%%%%%
%
%%% RE-ORGANIZE IN SEPARATE MATRICES
%
%%%%%%%%%%%%%%%%%%%%%%%%%%%%%%%%%%%%%%%%%%%%%%%%%%%%%%%%%%%%%%%%%%%%%%%%%%%


%Each external parameter is defined by a matrix of four columns.
%1st column: avg. time
%2nd column: std. deviation of time
%3rd column: avg. external parameter
%4th column: std. deviation of external parameter
avgVoc=zeros(length(allDataMatrix_avg(:,1)),4);
avgJsc=zeros(length(allDataMatrix_avg(:,1)),4);
avgFF=zeros(length(allDataMatrix_avg(:,1)),4);
avgEff=zeros(length(allDataMatrix_avg(:,1)),4);
avgSser=zeros(length(allDataMatrix_avg(:,1)),4);
avgSsht=zeros(length(allDataMatrix_avg(:,1)),4);

avgVoc(:,1)=allDataMatrix_avg(:,1);
avgVoc(:,2)=allDataMatrix_dev(:,1);
avgVoc(:,3)=allDataMatrix_avg(:,2);
avgVoc(:,4)=allDataMatrix_dev(:,2);

avgJsc(:,1)=allDataMatrix_avg(:,1);
avgJsc(:,2)=allDataMatrix_dev(:,1);
avgJsc(:,3)=allDataMatrix_avg(:,3)*-1;
avgJsc(:,4)=allDataMatrix_dev(:,3);

avgEff(:,1)=allDataMatrix_avg(:,1);
avgEff(:,2)=allDataMatrix_dev(:,1);
avgEff(:,3)=allDataMatrix_avg(:,4);
avgEff(:,4)=allDataMatrix_dev(:,4);

avgFF(:,1)=allDataMatrix_avg(:,1);
avgFF(:,2)=allDataMatrix_dev(:,1);
avgFF(:,3)=allDataMatrix_avg(:,5);
avgFF(:,4)=allDataMatrix_dev(:,5);

avgSser(:,1)=allDataMatrix_avg(:,1);
avgSser(:,2)=allDataMatrix_dev(:,1);
avgSser(:,3)=allDataMatrix_avg(:,6);
avgSser(:,4)=allDataMatrix_dev(:,6);

avgSsht(:,1)=allDataMatrix_avg(:,1);
avgSsht(:,2)=allDataMatrix_dev(:,1);
avgSsht(:,3)=allDataMatrix_avg(:,7);
avgSsht(:,4)=allDataMatrix_dev(:,7);

%% Generate relative matrices for each external parameter
relVoc=zeros(length(allDataMatrixRel_avg(:,1)),4);
relJsc=zeros(length(allDataMatrixRel_avg(:,1)),4);
```

```
relFF=zeros(length(allDataMatrixRel_avg(:,1)),4);
relEff=zeros(length(allDataMatrixRel_avg(:,1)),4);
relSser=zeros(length(allDataMatrixRel_avg(:,1)),4);
relSsht=zeros(length(allDataMatrixRel_avg(:,1)),4);


relVoc(:,1)=allDataMatrixRel_avg(:,1);
relVoc(:,2)=allDataMatrixRel_dev(:,1);
relVoc(:,3)=allDataMatrixRel_avg(:,2);
relVoc(:,4)=allDataMatrixRel_dev(:,2);

relJsc(:,1)=allDataMatrixRel_avg(:,1);
relJsc(:,2)=allDataMatrixRel_dev(:,1);
relJsc(:,3)=allDataMatrixRel_avg(:,3);
relJsc(:,4)=allDataMatrixRel_dev(:,3);

relEff(:,1)=allDataMatrixRel_avg(:,1);
relEff(:,2)=allDataMatrixRel_dev(:,1);
relEff(:,3)=allDataMatrixRel_avg(:,4);
relEff(:,4)=allDataMatrixRel_dev(:,4);

relFF(:,1)=allDataMatrixRel_avg(:,1);
relFF(:,2)=allDataMatrixRel_dev(:,1);
relFF(:,3)=allDataMatrixRel_avg(:,5);
relFF(:,4)=allDataMatrixRel_dev(:,5);

relSser(:,1)=allDataMatrixRel_avg(:,1);
relSser(:,2)=allDataMatrixRel_dev(:,1);
relSser(:,3)=allDataMatrixRel_avg(:,6);
relSser(:,4)=allDataMatrixRel_dev(:,6);

relSsht(:,1)=allDataMatrixRel_avg(:,1);
relSsht(:,2)=allDataMatrixRel_dev(:,1);
relSsht(:,3)=allDataMatrixRel_avg(:,7);
relSsht(:,4)=allDataMatrixRel_dev(:,7);

num_cells=length(dataCellSorted);


%%%%%%%%%%%%%%%%%%%%%%%%%%%%%%%%%%%%%%%%%%%%%%%%%%%%%%%%%%%%%%%%%%%%%%%%%%%%%
%
%%% WRITE DATA MATRICES TO FILE
%
%%%%%%%%%%%%%%%%%%%%%%%%%%%%%%%%%%%%%%%%%%%%%%%%%%%%%%%%%%%%%%%%%%%%%%%%%%%%%


%average values
dlmwrite([sample_name '_Voc.dat'],avgVoc,'delimiter',
'\t','precision','%1.3e');
dlmwrite([sample_name '_Jsc.dat'],avgJsc,'delimiter',
'\t','precision','%1.3e');
dlmwrite([sample_name '_Eff.dat'],avgEff,'delimiter',
'\t','precision','%1.3e');
dlmwrite([sample_name '_FF.dat'],avgFF,'delimiter',
'\t','precision','%1.3e');
dlmwrite([sample_name '_Sser.dat'],avgSser,'delimiter',
'\t','precision','%1.3e');
dlmwrite([sample_name '_Ssht.dat'],avgSsht,'delimiter',
'\t','precision','%1.3e');
%relative values
```

```
dlmwrite([sample_name '_relVoc.dat'],relVoc,'delimiter',
'\t','precision','%1.3e');
dlmwrite([sample_name '_relJsc.dat'],relJsc,'delimiter',
'\t','precision','%1.3e');
dlmwrite([sample_name '_relEff.dat'],relEff,'delimiter',
'\t','precision','%1.3e');
dlmwrite([sample_name '_relFF.dat'],relFF,'delimiter',
'\t','precision','%1.3e');
dlmwrite([sample_name '_relSser.dat'],relSser,'delimiter',
'\t','precision','%1.3e');
dlmwrite([sample_name '_relSsht.dat'],relSsht,'delimiter',
'\t','precision','%1.3e');

%return to home directory
cd(home_dir);
```

Fitting the Efficiency Results

```
%This script is intended to fit the relation given by Terakawa et al.
%to the efficiency degradation data which is obtained through in-situ
%measurements during light soaking. It is assumed that the data in question
%has already been processed into averages, and placed in the appropriate
%directory, by using the "Degradation_Data.m" script.

%The script generates a .dat-file containing the data corresponding to the
%curve which fits the averaged data imported here. Moreover, a .dat-file
%containing the thickness of the intrinsic layer of the sample, as well as
%the final value of the fitting parameters is generated.


clear all;
clc;
hold off;

%%%%%%%%%%%%%%%%%%%%%%%%%%%%%%%%%%%%%%%%%%%%%%%%%%%%%%%%%%%%%%%%%%%%%%%%%%%
%
%%% DEFINE SAMPLE NAME AND PATH NAMES AND IMPORT DATA
%
%%%%%%%%%%%%%%%%%%%%%%%%%%%%%%%%%%%%%%%%%%%%%%%%%%%%%%%%%%%%%%%%%%%%%%%%%%%

sample_name='A6737-III';
thickness=900;
working_dir=cd;
sample_path=['C:\Users\Kim\Documents\TU Delft\SET 2nd year\MSc
Project\Degradation\R20 material\Third Sample Set\' sample_name];
avgEff=dlmread([sample_path '\' sample_name '_Eff.dat'],'\t');


%%%%%%%%%%%%%%%%%%%%%%%%%%%%%%%%%%%%%%%%%%%%%%%%%%%%%%%%%%%%%%%%%%%%%%%%%%%
%
%%% SET VARIABLES FOR OPTIMIZATION PROCEDURE
%
%%%%%%%%%%%%%%%%%%%%%%%%%%%%%%%%%%%%%%%%%%%%%%%%%%%%%%%%%%%%%%%%%%%%%%%%%%%
maximum_iterations=10E28;
maximum_fevals=10E28;
tolerance=10E-6;

Eff_init=avgEff(1,3);
Eff_final=avgEff(length(avgEff(:,1)),3);
Eff_init_min=Eff_init-0.05*Eff_init;
Eff_init_max=Eff_init;
Eff_final_min=Eff_final-0.5*Eff_final;
Eff_final_max=Eff_final;

global xdata ydata;
xdata=avgEff(:,1)
ydata=avgEff(:,3)


%%%%%%%%%%%%%%%%%%%%%%%%%%%%%%%%%%%%%%%%%%%%%%%%%%%%%%%%%%%%%%%%%%%%%%%%%%%
%
%%% SET OPTIONS FOR OPTIMIZATION PROCEDURE
%
```

```
%%%%%%%%%%%%%%%%%%%%%%%%%%%%%%%%%%%%%%%%%%%%%%%%%%%%%%%%%%%%%%%%%%%%%%%%%%%
maxIter=1000;
maxFunVal=10e28;
tolerance=1e-7;

startingPoint=[2,1000,0.8, Eff_final, Eff_init];

options=optimset('fmincon');
options=optimset(options,'Algorithm','interior-point');
options=optimset(options,'MaxIter',maxIter);
options=optimset(options,'MaxFunEvals',maxFunVal);
options=optimset(options,'TolFun',tolerance);

%%%%%%%%%%%%%%%%%%%%%%%%%%%%%%%%%%%%%%%%%%%%%%%%%%%%%%%%%%%%%%%%%%%%%%%%%%%
%
%%% CALL OPTIMIZATION FUNCTION
%
%%%%%%%%%%%%%%%%%%%%%%%%%%%%%%%%%%%%%%%%%%%%%%%%%%%%%%%%%%%%%%%%%%%%%%%%%%%

[estimates,fvalue,eflag]=fmincon(@ObjectFunction,startingPoint,[],[],[],[],
[0  0 0 Eff_final_min Eff_init_min],[5 1000000 2 Eff_final_max
Eff_init_max],'',options);


%%%%%%%%%%%%%%%%%%%%%%%%%%%%%%%%%%%%%%%%%%%%%%%%%%%%%%%%%%%%%%%%%%%%%%%%%%%
%
%%% GENERATE VARIABLE CONTAINING FIT
%
%%%%%%%%%%%%%%%%%%%%%%%%%%%%%%%%%%%%%%%%%%%%%%%%%%%%%%%%%%%%%%%%%%%%%%%%%%%

FittedCurve=zeros(length(avgEff(:,1)),2);
FittedCurve(:,1)=avgEff(:,1);
FittedCurve(:,2)=(-1/estimates(1))*log10(1-(1-(1/(10^estimates(1))))*exp(-
1*(FittedCurve(:,1)/estimates(2)).^estimates(3)));
FittedCurve(:,2)=FittedCurve(:,2)*(estimates(5)-estimates(4))+estimates(4);


%%%%%%%%%%%%%%%%%%%%%%%%%%%%%%%%%%%%%%%%%%%%%%%%%%%%%%%%%%%%%%%%%%%%%%%%%%%
%
%%% PLOT DATA AND FITTED CURVE
%
%%%%%%%%%%%%%%%%%%%%%%%%%%%%%%%%%%%%%%%%%%%%%%%%%%%%%%%%%%%%%%%%%%%%%%%%%%%
semilogx(avgEff(:,1),avgEff(:,3),'r*');
hold on;
semilogx(FittedCurve(:,1),FittedCurve(:,2),'b');

%%%%%%%%%%%%%%%%%%%%%%%%%%%%%%%%%%%%%%%%%%%%%%%%%%%%%%%%%%%%%%%%%%%%%%%%%%%
%
%%% WRITE TO FILE - FITTED CURVE AND FITTING PARAMETERS
%
%%%%%%%%%%%%%%%%%%%%%%%%%%%%%%%%%%%%%%%%%%%%%%%%%%%%%%%%%%%%%%%%%%%%%%%%%%%
cd(sample_path);
estimates=[thickness estimates];
fid=fopen('fitEff_param.dat','w');
x='#This file contains the four fitting parameters';
r='#Thickness';
y='n';
z='Tau';
k='Beta';
```

```
p='FF final';
l='FF initial';
fprintf(fid, '%s\n %s\t %s\t %s\t %s\t %s\t %s\n',x,r,y,z,k,p,l);
dlmwrite('fitEff_param.dat',estimates,'-append','delimiter','\t');
fclose(fid);
dlmwrite([sample_name '_fitEff.dat'],FittedCurve,'delimiter',
'\t','precision','%1.3e');
cd(working_dir);
```

```
%%%%%%%%%%%%%%%%%%%%%%%%%%%%%%%%%%%%%%%%%%%%%%%%%%%%%%%%%%%%%%%%%%%%%%%%%%%
%
%%% OBJECT FUNCTION WHICH IS MINIMIZED BY THE OPTIMIZATION ROUTINE
%
%%%%%%%%%%%%%%%%%%%%%%%%%%%%%%%%%%%%%%%%%%%%%%%%%%%%%%%%%%%%%%%%%%%%%%%%%%%

function f=ObjectFunction(x)

global xdata;
global ydata;

    f= sum(1000 * (ydata - (x(4)+(x(5)-x(4))*(-1/x(1))*log10(1-(1-
(1/(10^x(1))))*exp(-(xdata/x(2)).^x(3))))).^2);
end
```

List of References

[1] J. Neumann, "Climatic Change as a Topic in the Classical Greek and Roman Literature," *Climatic Change,* no. 7, pp. 441-454, 1985.

[2] I. Held and B. Soden, "Water Vapour Feedback and Global Warming," *Annual Review of Energy and the Environment (Annual Reviews),* no. 25, pp. 441-475, 2000.

[3] D. Biello, "www.scientificamerican.com," Scientific American, 11 December 2011. [Online]. Available: http://www.scientificamerican.com/article.cfm?id=climate-talks-consensus-a&page=2. [Accessed 4 April 2013].

[4] F. Convery, "Issues in Emissions Trading - an Introduction," Environmental Institute, University College Dublin, Dublin, 2003.

[5] UNFCCC, "Status of Ratification of the Kyoto Protocol," 2012. [Online]. Available: http://unfccc.int/kyoto_protocol/status_of_ratification/items/2613.php. [Accessed 1 April 2013].

[6] IEA, "World Energy Outlook 2012," OECD/IEA, Paris, 2012.

[7] IEA, "World Energy Outlook 2006," OECD/IEA, Paris, 2006.

[8] IPCC, "Special Report on Renewable Energy and Climate Change Mitigation," Intergovernmental Panel on Climate Change, 2011.

[9] Green Rhino Energy, "Green Rhino Energy," Green Rhino Energy Ltd, [Online]. Available: http://www.greenrhinoenergy.com/solar/radiation/spectra.php. [Accessed 6 April 2013].

[10] USDOE, "Sunshot Vision Study February 2012," USDOE, 2012.

[11] M. Jensen, "Atom-like Properties of Quantum Dots Could Double Solar Cell Efficiencies," *Journal of Young Investigators,* 2010.

[12] P. Hoertz, A. Staniszewski, A. Marton, G. Higgins, C. Incarvito, A. Rheingold and G. Meyer, "Toward Exceeding the Shockley-Queisser Limit:Photoinduced Interfacial Charge Transfer Processes that Store Energy in Excess of the Equilibrated Excited State," *Journal of American Chemical Society,* no. 128, pp. 8234-8245, 2006.

[13] S. Hegedus, "Thin Film Solar Modules: The Low Cost, High Throughput and Versatile Alternative to Si Wafers," *Progress in Photovoltaics: Research and Applications,* no. 14, pp. 393-411, 2006.

[14] R. Kind, "Dark Current Characteristics of Amorphous Silicon Solar Cells, MSc Thesis," Technische Universiteit Delft, Delft, 2010.

[15] M. Zeman and R. Schropp, Amorphous and Microcrystalline Silicon Solar Cells: Modeling, Materials, and Device Technology, Boston/Dordrecht/London: Kluwer Academic Publishers, 1998.

[16] A. Smets, W. Kessels and M. v. d. Sanden, "Vacancies and Voids in Hydrogenated Amorphous Silicon," *Applied Physics Letters,* vol. 82, no. 10, pp. 1547-1549, 2003.

[17] A. Smets, C. Wronski, M. Zeman and M. v. d. Sanden, "The Staebler-Wornski Effect: New Physical Approaches and Insights as a Route to Reveal its Origin," in *Materials Research Society Proceedings*, San Fransisco, 2010.

[18] A. Smets and M. Sanden, "Relation of the Si-H stretching frequency to the naostructural Si-H Bulk Environment," *Physical Review B,* p. 073202, 2007.

[19] C. Honsberg and S. Bowden, "www.pveducation.org," [Online]. Available: http://pveducation.org/pvcdrom/pn-junction/doping. [Accessed 6 April 2013].

[20] H. Fritzsche, "A New Perspective on an Old Problem - The Staebler-Wronski Effect," in *Materials Research Society Proceedings*, San Fransisco, 2010.

[21] A. Smets, A. Wank, B. Vet, M. Fischer, R. van Swaaij, M. Zeman, D. Bobela, C. Wronski and M. v. d. Sanden, "The Relation Between the Bandgap and the Anisotropic Nature of Hydrogenated Amorphous Silicon," *IEEE Journal of Photovoltaics,* vol. 2, no. 2, pp. 94-98, 2012.

[22] M. Zeman, "Lecture Notes: Thin Film Silicon Solar Cells," in *Solar Cells*, Delft, Technische Universiteit Delft, 2010.

[23] Institut fur Angewandte Photophysik, "http://www.iapp.de/iapp/," [Online]. Available: http://www.iapp.de/iapp/agruppen/osol/?Research:Organic_Solar_Cells:The_pin-concept_in_OSC. [Accessed 14 April 2013].

[24] C. Solanki and G. Beaucarne, "Advanced Solar Cell Concepts," *Energy for Sustainable Development,* vol. 11, no. 3, pp. 17-23, 2007.

[25] D. Staebler and C. Wronski, "Reversible Conductivity Changes in Discharge-Produced Amorphous Si," *Applied Physics Letters,* vol. 31, no. 4, pp. 292-294, 1977.

[26] H. Fritzsche, "Development in Understanding and Controlling the Staebler-Wronski Effect in a-Si:H," *Annual Reviews,* vol. 31, pp. 47-79, 2001.

[27] J. Nelson, The Physics of Solar Cells, London: Imperial College, 2003.

[28] T. Shimizu, "Staebler-Wronski Effect in Hydrogenated Amorphous Silicon and Related Alloy Films," *Japanese Journal of Applied Physics,* vol. 43, no. 6A, pp. 3257-3268, 2004.

[29] A. Kolodziej, "Staebler-Wronski Effect in Amorphous Silicon and Its Alloys," *Opto-Electronics*

Review, vol. 12, no. 1, pp. 21-32, 2004.

[30] H. Branz, "Hydrogen Collision Model: Quantitative Description of Metastability in Amorphous Silicon," *Physical Review,* vol. 59, no. 8, pp. -, 1999.

[31] A. Klaver and R. van Swaaij, "Modeling of light-induced degradation of amorphous silicon solar cells," *Solar Energy Materials & Solar Cells,* no. 92, pp. 50-60, 2008.

[32] V. Nadazdy and M. Zeman, "Origin of charged gap states in a-Si:H and their evolution during light soaking," *Physical Review B,* p. 165213, 2004.

[33] B. Yan, J. Yang, K. Lord and S. Guha, "Annealing kinetics of amorphous silicon alloy solar cells made at various deposition rates," in *Materials Research Society Symposium*, San Fransisco, 2001.

[34] J. Melskens, G. van Elzakker, Y. Li and M. Zeman, "Analysis of hydrogenated amorphous silicon thin films and solar cells by means of Fourier Transform Photocurrent Spectroscopy," *Thin Solid Films,* no. 516, pp. 6877-6881, 2008.

[35] G. van Elzakker, "Hydrogenated Amorphous Silicon Solar Cells Deposited From Silane Diluted with Hydrogen, Ph.D Thesis," Technische Universiteit Delft, Delft, 2010.

[36] E. Johlin, N. Tabet, S. Castro-Galnares, A. Abdallah, M. Bertoni, T. Asafa, J. Grossman, S. Said and T. Bounassisi, "Structural origins of intrinsic stress in amorphous silicon thin films," *Physical Review B,* vol. 85, p. 075202, 2012.

[37] K. Shimizu, T. Tabuchi, M. Iida and H. Okamoto, "Photoinduced structural change and defect creation in hydrogenated amorphous silicon," *Journal of Non-Crystalline Solids,* pp. 227-230, 1998.

[38] B. Pieters, H. Stiebig, M. Zeman and R. van Swaaij, "Determination of the mobility gap of intrinsic µc-Si:H in p-i-n solar cells," *Journal of Applied Physics,* no. 105, p. 044502, 2009.

[39] R. van Swaaij, R. Kind and M. Zeman, "Recombination efficacy in a-Si:H p-i-n devices," *Journal of Non-Crystalline Solids,* no. 358, pp. 2190-2193, 2012.

[40] J. Deng and C. Wronski, "Carrier recombination and differential diode quality factors in the dark forward bias current-voltage characteristics of a-Si:H solar cells," *Journal of Applied Physics,* vol. 98, no. 2, p. 024509, 2005.

[41] M. Kroon and R. van Swaaij, "Spatial effects on ideality factor of amorphous silicon pin diodes," *Journal of Applied Physics,* vol. 90, no. 2, pp. 994-1000, 2001.

[42] R. Kind, R. van Swaaij, F. Rubinelli, S. Solntsev and M. Zeman, "Thermal ideality factor of hydrogenated amorphous silicon p-i-n solar cells," *Journal of Applied Physics,* no. 110, p. 104512, 2011.

[43] J. Willemen, "Modelling of Amorphous Silicon Single- and Multi-Junction Solar Cells, Ph.D Thesis," Technische Universiteit Delft, Delft, 1998.

[44] L. Chen and L. Yang, "Kinetics of Light Induced Degradation in a-Si:H Solar Cells," *Journal of Non-Crystalline Solids,* no. 137-138, pp. 1185-1188, 1991.

[45] D. Redfield, "Kinetics, energetics, and origins of defects in amorphous Si:H," *Journal of Applied Physics,* vol. 52, no. 6, p. 492, 1988.

[46] A. Terakawa, M. Isomura and S. Tsuda, "Effect of the i-Layer Optical Gap on the Light-Induced Degradation of a-SiGe Solar Cells," *Japanese Journal of Applied Physics,* vol. 35, no. 11, pp. 5612-5617, 1996.

[47] Wikipedia, "Wikipedia," Wikipedia, 2013. [Online]. Available: http://en.wikipedia.org/wiki/Electron_beam_physical_vapor_deposition. [Accessed 16 April 2013].

[48] Wikipedia, "Wikipedia," Wikipedia, 2013. [Online]. Available: http://en.wikipedia.org/wiki/Reactive-ion_etching. [Accessed 16 April 2013].

[49] K. Zwetsloot, "Manual for the Quantum Efficiency Measurement Setup," -, Delft, 2009.

[50] A. Mohammed, "Software Development for Solar Cell Degradation Setup, BSc Thesis," Technische Universiteit Delft, Delft, 2011.

[51] A. Klaver, "Irradiation-induced degradation of amorphous silicon solar cells in space, Ph.D Thesis," Technische Universiteit Delft, Delft, 2007.

[52] C. Malone, J. Nicque, S. Fonash and C. Wronski, "Effect of light induced defects on the quantum efficiency of amorphous silicon shottcky barrier solar cell structures," in *IEEE Photovoltaics Specialist Conference*, Las Vegas, 1991.

[53] A. Klaver and R. van Swaaij, "Modeling of light-induced degradation of amorphous silicon solar cells," *Solar Energy Materials & Solar Cells,* no. 92, pp. 50-60, 2007.

[54] N. Wyrsch and A. Shah, "Degradation of a-Si:H solar cells: new evidence for a bulk effect," in *Conference Record of the Twenty Fourth IEEE Photovoltaic Specialists Conference*, Waikoloa, 1994.

[55] S. Myong and K. Lim, "Modeling of annealing kinetics for hydrogenated-amorphous-silicon-based solar cells using two-component metastable defects," *Applied Physics Letters,* no. 88, p. 243510, 2006.

[56] M. Stutzmann, W. Jackson and C. Tsai, "Light-induced metastable defects in hydrogenated amorphous silicon: A systematic study," *Physical Review B,* vol. 32, no. 1, 1985.

[57] B. Ross, J. Deng, M. Albert, R. Collins and C. Wronski, "Evolution of Metastable Defects in Intrinsic Layers of A-Si:H Solar Cells and Corresponding Thin Film Materials Characterized by Carrier Recombination Through Midgap States," *Conference Record of the 2006 IEEE 4th World Conference on Photovoltaic Energy Conversion,* vol. 2, pp. 1576 - 1579, 2006.

[58] L. Yang and L. Chen, ""Fast" and "slow" metastable defects in hydrogenated amorphous silicon," *Applied Physics Letters,* vol. 63, no. 400, 1993.

[59] J. Pearce, J. Deng, M. Albert, C. Wronski and R. Collins, "Room temperature annealing of fast state from 1 sun illumination in protocrystalline Si:H materials and solar cells," *Conference Record of the Thirty-first IEEE Photovoltaic Specialists Conference,* pp. 1536 - 1539, 2005.

[60] D. Carlson and K. Rajan, "The reversal of light-induced degradation in amorphous silicon solar cells by an electric field," *Applied Physics Letters,* vol. 70, no. 16, pp. 2168-2170, 1997.

[61] J. Frenkel, "On pre-breakdown phenomena in insulators and electronic semi-conductors," *Physical Review ,* vol. 54, pp. 647-648, 1938.

[62] B. Pieters, "Characterization of Thin-Film Silicon Materials and Solar Cells Through Numerical Modeling, Ph.D Thesis," Technische Universiteit Delft, Delft, 2008.